Numerical Modeling of Room-and-Pillar Coal Mine Ground Response

Benjamin P. Fahrman

Dissertation submitted to the Faculty of the
Virginia Polytechnic Institute and State University
in partial fulfillment of the requirements for the degree of

Doctor of Philosophy
in
Mining Engineering

Erik C. Westman, Chair
Mario G. Karfakis
Michael M. Murphy
Nino S. Ripepi

18 February 2016
Blacksburg, Virginia

Keywords: Numerical Modeling, Room-and-Pillar Coal Mining, Ground Response Curve

Numerical Modeling of Room-and-Pillar Coal Mine Ground Response

Benjamin P. Fahrman

(ABSTRACT)

Underground coal mine ground control persists as a unique challenge in rock mass engineering. Fall of roof and rib continue to present a hazard to underground personnel. Stability of underground openings is a prerequisite for successful underground coal mine workings. An adaptation of a civil engineering design standard for analyzing the stability of underground excavations for mining geometries is given here. The ground response curve–developed over seventy years ago for assessing tunnel stability–has significant implications for the design of underground excavations, but has seen little use in complex mining applications.

The interaction between the small scale (pillar stress-strain) and the large scale (ground response curve) is studied. Further analysis between these two length scales is conducted to estimate the stress on pillars in a room-and-pillar coal mine. These studies are performed in FLAC3D by implementing a two-scale, two-step approach. This two-scale approach allows for the interaction between the small, pillar scale and the large, panel scale to be studied in a computationally efficient manner.

That this work received support from the National Institute of Occupational Safety and Health's "Capacity Building Project" is purely coincidental.

Acknowledgments

Endeavors such as this are never completed alone. There are too many people to thank to include them all here, but...

I'd like to start by thanking my family–my parents, especially. Your support has helped me accomplish things you always swore were possible, but of which I was never sure.

Thank you to the friends I've made during my extended time in Blacksburg. You're the reason I've loved this place. Of late, extreme appreciation is felt for Alma, in particular. Sanity can be fleeting during trying times and you have helped me keep mine (mostly) intact.

Thanks is owed to the past and present members of Holden 115A (and beyond!). We're all in this together, and you've helped me succeed in countless ways. I won't name you all, but Brent and Will deserve special thanks: Brent for his willingness to argue about what the ground response curve really means when applied to mining, and Will for his time and effort payed into catching me up on all the ins and outs of our case study.

I appreciate the support I've received from the members of my committee. I've learned a lot from each of you, and it's been a pleasure working with you. I'd like to thank Dr. Erik Westman, in particular, for finding a way to help me achieve things I didn't think possible, and Mario for his encouragement for me to succeed.

I'll also thank Magpie and Bode, the friendly creatures of my unlikely Walden Pond: Magpie for her unwavering inclination to contribute to my writing, and Bode for his willingness to distract me–typically only when I wished.

Finally, I'll thank the great students with whom I've had the joy of interacting. In the few short years of my teaching, you have kindled in me the desire to complete a terminal degree in the hopes of securing a position for future teaching. You, more than anyone else, have pushed me to finish this.

Contents

List of Figures

List of Tables

Chapter 1

Introduction

Recent projections made by the US Energy Information Administration (EIA) predict energy demands to increase steadily in the near future. Combustion of coal remains to be a large source of power in the United States and around the world. 40% of all coal produced is produced from underground coal mines, and 40% of that comes from room-and-pillar mines [1]. Despite the fact that 2015 saw the greatest percentage decrease in US coal production ever, the EIA foresees coal production to remain steady or increase over the next few years [2].

Ground control is a primary design consideration during the planning and development of underground coal mines. Day-to-day functions in underground coal mines, like proper ventilation and material haulage, depend on successful ground control design and implementation. In addition, ground control design considerations provide structural stability for mine workings. Successful ground control is an integral condition for successful mining projects [3].

Geotechnical considerations for coal mine design include a unique set of challenges. Coal measure rocks vary considerably in strength and are often highly jointed or laminated. Furthermore, the soft, sometimes unpredictable nature of coal consistently provides greater complexity for underground coal mine design.

Despite a clear focus on safe and effective mine design from a ground control perspective for decades, ground control issues continue to result in injuries and fatalities. Over 16% of all reported incidents in underground coal mines from 2006 to 2014 were due to fall of roof or rib [4]. The total number of injuries attributed to ground control issues in underground coal mines in the US is shown in Figure 1.1. There has been a downward trend in the number of

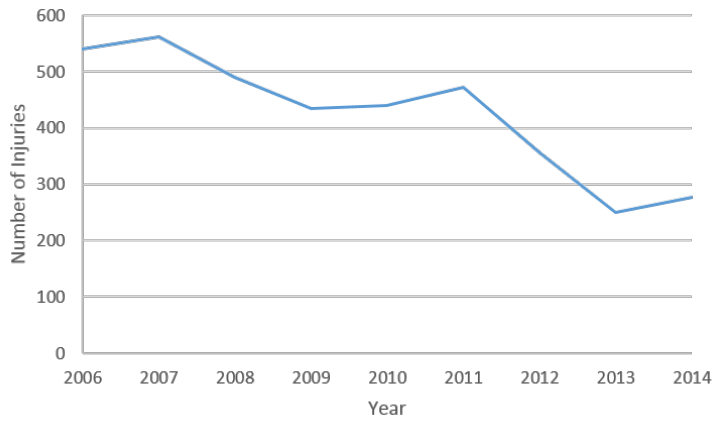

Figure 1.1: Injuries due to fall of roof or rib between 2006 and 2014. This includes fatal injuries, non-fatal injuries with days lost, and injuries with no days lost [4].

incidents for many years, but ground control issues remain a considerable hazard.

The ground response curve (GRC) is a useful tool to aid in the design of underground openings. The GRC originated from the convergence-confinement method (CCM)–a design standard of the tunneling industry. In its original form, CCM was an attempt to quantify the reaction of a rock mass to the development of underground openings within it. A result of this analytical method is the GRC which is the relationship between the reduced radial pressure inside of a circular tunnel due to excavation and the radial convergence of that excavation [5]. A depiction of a ground response curve is shown in Figure 1.2.

Ground response curves are plotted on pressure-convergence axes. The curve begins on the pressure-axis at a value equal to the in situ stress state. As the internal pressure of the rock mass is reduced due to an approaching excavation, convergence is expected. The GRC represents the internal pressure required to prevent further convergence. The curve has great utility for estimating both the self-supporting capacity of an underground opening, as well as the type of support which should be installed [6].

The convergence-confinement method, when applied to circular tunnels, often predicts stable convergence [5]. Stable convergence is represented by the solid line in Figure 1.2, which shows convergence associated with an underground opening which has sufficient self-supporting capacity to limit convergence naturally. That is, if no artificial support is installed, the total convergence of the excavation is expected to be the intersection of the GRC

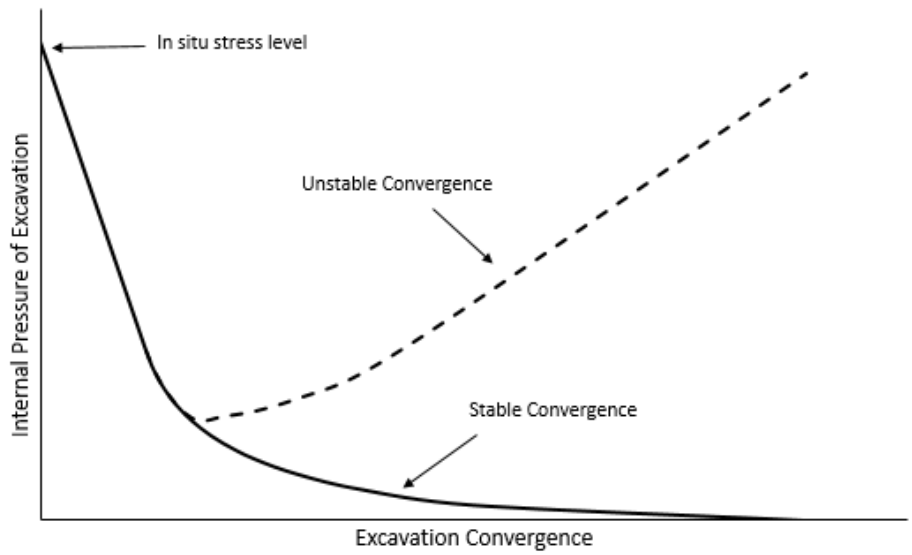

Figure 1.2: Ground reaction curve (GRC) with two possible outcomes shown. The curve with the solid line-type represents stable convergence, and the curve with the dashed line-type represents unstable convergence.

and the convergence-axis, where the internal pressure is zero.

Working sections in retreating room-and-pillar mines are not expected to experience stable convergence [7]. The dashed line in Figure 1.2 shows an underground opening which is expected to experience unstable convergence. The minimum point in the curve represents a loss of self-supporting capacity of the rock mass. Full collapse of the opening is expected after the rock mass no longer has the structural integrity to support its own weight. A loss of self-supporting capacity is represented by the increasing slope of the GRC where the internal pressure required to prevent future convergence approaches the original lithostatic stress.

The geometry of underground mine openings tends to be far more complex than that of the tunnels in civil engineering projects. While analytical solutions such as that obtained from the CCM are prohibitively complex for mine geometries, a ground response curve may still be obtained. Numerical models can been used in an attempt to solve for the GRC for mining applications.

Numerical models were used to estimate the ground response curves for a room-and-pillar coal mine in the central Appalachian coal fields of the eastern US. In addition, loads on the pillars were estimated during advance by using numerical models. All of the numerical

modeling performed for this study was completed in FLAC3D (Fast Lagrangian Analysis of Continua in 3-Dimensions) [8].

The interaction between the large, panel scale and the smaller, pillar scale has been explored previously using numerical modeling in FLAC3D. [9] used an explicitly modeled pillar geometry within a panel-scale model. Including an explicitly modeled pillar array–which requires fine discretization–within a FLAC3D model with large spatial extent results in computational inefficiency. FLAC3D is advertised to have slow execution times if there are significant differences in zone sizes [10], which would be required for explicit representation of pillars in a large scale model.

The ground response curve predicts the response of the rock mass on a large scale, so large-scale models are required to obtain reasonable results. However, the GRC and pillar loading depend on small-scale interactions in and around underground openings. A model with fine enough discretization to represent the small-scale interactions would be prohibitively inefficient in large-scale models. A computationally efficient large-scale model would be too coarse to capture the small-scale effects accurately. In order to model these phenomena in a computationally reasonable manner, a two-scale approach was used.

The two-scale approach begins with modeling on a pillar-scale. The stress-strain response of the pillars in small-scale models is then incorporated into much larger models. A fictitious material which represents the behavior of the excavated coal seam is created by implementing a user-defined constitutive model in FLAC3D. This user-defined constitutive model is applied to the zones within the modeled coal seam so they respond as an excavated coal seam would, but with a discretization far too coarse to model the pillars explicitly.

Lab testing was performed on samples of roof rock to estimate material properties in order to improve the accuracy of the numerical models. The samples were obtained from core holes drilled into the roof from the mine workings. The destructive laboratory tests which were performed include uniaxial compressive strength testing, Brazilian testing, and point-load testing. Measurements were also taken to estimate the acoustic properties and density of the roof rock.

Works Cited

[1] US EIA. Annual coal report 2013. *US Energy Information Administration, Washington, DC*, 2013.

[2] US EIA. Short term energy outlook. *Energy Information Administration, Department of Energy*, 2016.

[3] Christopher Mark and Thomas M Barczak. Fundamentals of coal mine roof support. *New Technology for Coal Mine Roof Support, Proceedings of the NIOSH Open Industry Briefing, NIOSH IC*, 9453:23–42, 2000.

[4] Mine safety and health administration.

[5] Edwin T Brown, John W Bray, Branko Ladanyi, and Evert Hoek. Ground response curves for rock tunnels. *Journal of Geotechnical Engineering*, 1983.

[6] Pierpaolo Oreste. The convergence-confinement method: roles and limits in modern geomechanical tunnel design. *American Journal of Applied Sciences*, 6(4):757, 2009.

[7] B Damjanac, M Pierce, and M Board. Methodology for stability analysis of large room-and-pillar panels. In *48th US Rock Mechanics/Geomechanics Symposium*. American Rock Mechanics Association, 2014.

[8] Itasca Consulting Group, Inc., Minnesota. *Fast Lagrangian Analysis of Continua in 3-Dimensions, version 5.0, manual*, 2013.

[9] Essie Esterhuizen, Chris Mark, and Michael Murphy. The ground response curve, pillar loading and pillar failure in coal mines. In *29th International Conference on Ground Control in Mining*, 2010.

[10] Inc. Itasca Consulting Group. Flac3d training course - basic concepts and recommended procedures, 2015.

Chapter 2

Literature Review

2.1 Introduction

An effective ground control design plan is a prerequisite for safe, efficient, and successful mining operations. In effect, ground control is the prediction of the response of a rock mass to excavation, as well as the prevention of any undesired outcomes regarding rock mass movement or stability. To lay the foundation for discussing the mechanical response of rock masses to excavation, an overview of mechanics is first given. The mechanics overview is then restricted to brittle materials like rock and then large-scale rock masses.

2.2 Mechanics Overview

Stress forms inside of a deformable body when an external force is applied. The stress produced is directly proportional to the force applied and inversely proportional to the area over which the force acts. Stresses which are perpendicular to the area on which they act are called normal stresses, and stresses which act parallel to the area on which they act are called shear stresses. In three dimensions, the total state of stress of an element inside of a deformable body includes the nine stresses shown as arrows in Figure 2.1.

The state of stress may also be completely defined by the matrix shown in Eq. (2.1), sometimes called the Cauchy stress tensor. The first subscript for each stress component indicates the normal (perpendicular) direction of the plane on which the stress acts. For instance, each of the stress components in the first row of the stress tensor, which have the

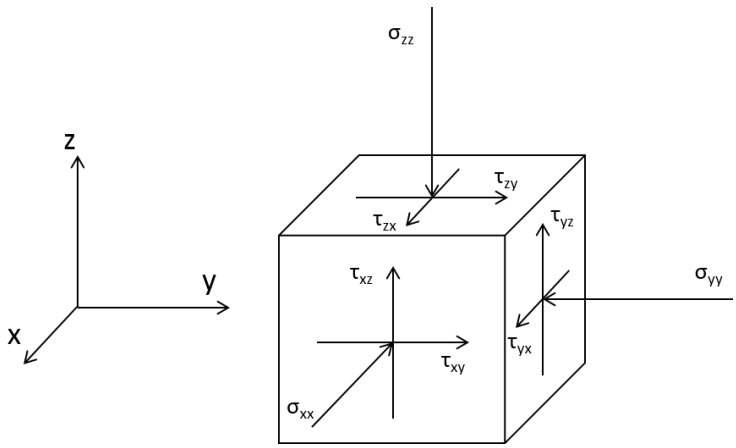

Figure 2.1: A three-dimensional element with all stress components depicted.

first subscript of x, act on the face coming out of the page of Figure 2.1. In addition, the second subscript of each stress component indicates the direction in which the stress acts. Each of the stress components listed in the first column of the stress tensor are directed parallel to the x-axis, as can be seen in Figure 2.1.

$$\begin{bmatrix} \sigma_{xx} & \tau_{xy} & \tau_{xz} \\ \tau_{yx} & \sigma_{yy} & \tau_{yz} \\ \tau_{zx} & \tau_{zy} & \sigma_{zz} \end{bmatrix} \tag{2.1}$$

By assuming that this element is in static equilibrium, it is clear that some components in the stress tensor are redundant. Specifically: $\tau_{xy} = \tau_{yx}$, $\tau_{yz} = \tau_{zy}$, and $\tau_{zx} = \tau_{xz}$. Accounting for static equilibrium reduces the number of unique stress components from nine to six. Therefore, the complete state of stress can be expressed by giving these six components: σ_{xx}, σ_{yy}, σ_{zz}, τ_{xy}, τ_{yz}, and τ_{zx}.

The magnitudes of these six stress components vary with the choice of axes orientation. For every state of stress, there exists an orientation of mutually orthogonal axes, called principal axes, in which the shear stresses are zero. The normal stresses oriented on the principal axes are called principal normal stresses, and are often labeled σ_1, σ_2, and σ_3. The first and third principal normal stresses, σ_1 and σ_3, are the maximum and minimum normal stresses acting in any direction, respectively. The second principal normal stress, σ_2, has some intermediate value.

While the magnitudes of the stress components listed in Eq. (2.1) are directionally

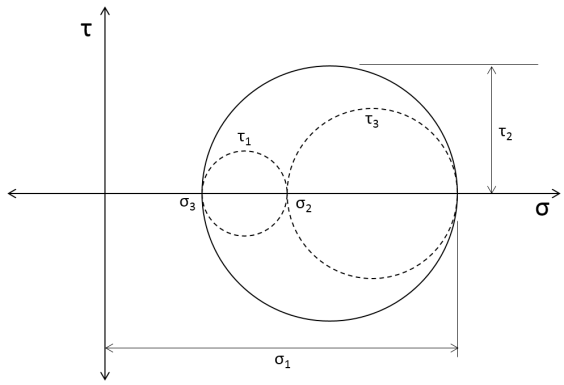

Figure 2.2: A three-dimensional state of stress represented by Mohr's Circles with principal normal and principal shear stresses labeled.

dependent, it can be shown [1] that the quantities in Eq. (2.2) are constant for a state of stress, regardless of choice of coordinate system. Because of their directional independence, they are called stress invariants.

$$\begin{aligned} I_1 &= \sigma_x + \sigma_y + \sigma_z \\ I_2 &= \sigma_x\sigma_y + \sigma_y\sigma_z + \sigma_z\sigma_x - \tau_{xy}^2 - \tau_{yz}^2 - \tau_{zx}^2 \\ I_3 &= \sigma_x\sigma_y\sigma_z + 2\tau_{xy}\tau_{yz}\tau_{zx} - \sigma_x\tau_{yz}^2 - \sigma_y\tau_{zx}^2 - \sigma_z\tau_{xy}^2 \end{aligned} \tag{2.2}$$

Furthermore, the stress invariants can be used to determine the magnitudes of the three principal normal stresses. The cubic equation shown in Eq. (2.3) always yields three real roots. The three solutions to this cubic are σ_1, σ_2, and σ_3 [1].

$$\sigma^3 - \sigma^2 I_1 + \sigma I_2 - I_3 = 0 \tag{2.3}$$

Any state of stress can be represented graphically on a plot of shear stress vs. normal stress, as shown in Figure 2.2. The plot in Figure 2.2 contains Mohr's Circles, which are named after Otto Mohr who developed this type of graphical representation. Each point on a circle represents the state of stress in some direction. The horizontal axis intercepts, where the shear stress is equal to zero, represent the principal normal stresses. Mohr's diagram also conveniently shows the maximum shear stress, which has a value equal to the radius of the largest circle.

Materials will deform when subjected to stress. The ratio of the amount of deformation

to the total original length of the material is called strain. That is, strain, ϵ, is equal to $\Delta L/L$, where L is the length of the unstressed material. Often it is convenient to express strains as percentages, where percent strain, $\epsilon\% = 100\epsilon$.

Strength is possibly the most important consideration in engineering design, because it is an attempt to define the limits of a component's functional applicability. In its most widely applicable form, strength can be defined as the applied stress at which a component will fail to perform its intended function. This definition has led to the use of a concept called factor of safety, FS, which is the ratio of strength to stress. Engineering designs with a factor of safety greater than one are expected to be successful, because the stress does not exceed the strength. Factors of safety less than one are expected to fail.

2.2.1 Elastic Moduli

Relationships between stress and strain are expressed through constitutive models. The simplest constitutive model to describe how a material deforms under stress is to assume that the material will deform proportionally to the load applied. This is identical to saying that stress and strain are linearly related. This model, called the elastic model, is described by Eq. (2.4).

$$\sigma = E\epsilon \tag{2.4}$$

Where E is called Young's modulus. This relationship is shown graphically in Figure 2.3. The slope of the stress-strain curve of an elastic material is constant and equal to the Young's modulus of the material. Furthermore, elastic materials are assumed to recover strain when they are unloaded. Elastic strains do not result in permanent deformation.

Young's modulus relates axial stress to axial strain. Axial strains cause a material to deform in perpendicular directions. This phenomenon, called the Poisson effect, is represented in Figure 2.4. While the amount of elongation, ΔL, due to the extensional stress in Figure 2.4 is dictated by the Young's modulus, the degree to which that elongation causes narrowing of the member is described by Poisson's ratio. Poisson's ratio, ν, is the opposite of the ratio of lateral strain to axial strain, as expressed in Eq. (2.5).

$$\nu = -\frac{\epsilon_{lateral}}{\epsilon_{axial}} \tag{2.5}$$

where $\epsilon_{lateral}$ is the lateral strain and ϵ_{axial} is the axial strain. Nearly all materials

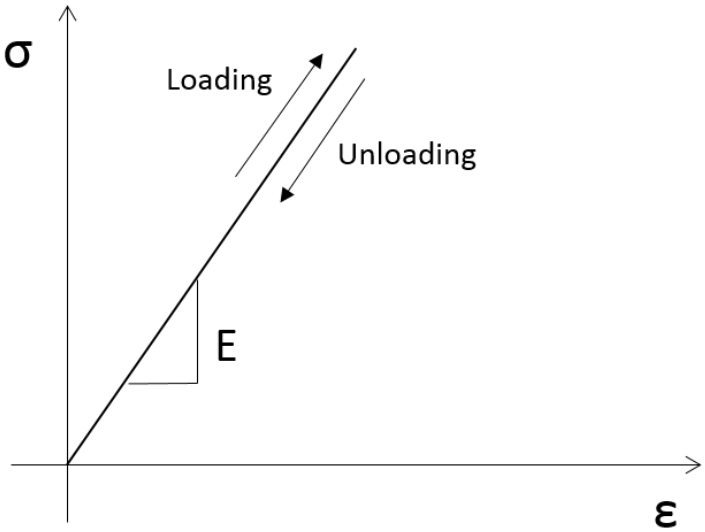

Figure 2.3: Stress-strain curve of elastic loading and unloading.

experience a positive lateral strain (extension) when subjected to a negative axial strain (compression), and a negative lateral strain when subjected to a positive axial strain. The ratio is negated to make the Poisson's ratio generally positive.

The normal stress in the x-direction causes an x-directional strain, ϵ_x, of magnitude σ_x/E, as well as a strain of magnitude $-\nu\epsilon_x$ in the y- and z-directions. This logic can be expanded to the other two axial directions to find expressions for the total strain in each direction. The total strain in each direction is summarized in Eq. (2.6).

$$\begin{aligned} \epsilon_x &= \tfrac{1}{E}\left[\sigma_x - \nu\left(\sigma_y + \sigma_z\right)\right] \\ \epsilon_y &= \tfrac{1}{E}\left[\sigma_y - \nu\left(\sigma_x + \sigma_z\right)\right] \\ \epsilon_z &= \tfrac{1}{E}\left[\sigma_z - \nu\left(\sigma_x + \sigma_y\right)\right] \end{aligned} \tag{2.6}$$

Young's modulus and Poisson's ratio are two of the six elastic moduli. Two other elastic moduli of importance are the bulk modulus, K, and the shear modulus, G. If any two elastic moduli are known for an isotropic, homogeneous material, then the other four can be determined. Eqs. (2.7) and (2.8) can be used to calculate the bulk modulus and shear modulus, respectively, if both Young's modulus and Poisson's ratio are known.

$$K = \frac{E}{3\left(1 - 2\nu\right)} \tag{2.7}$$

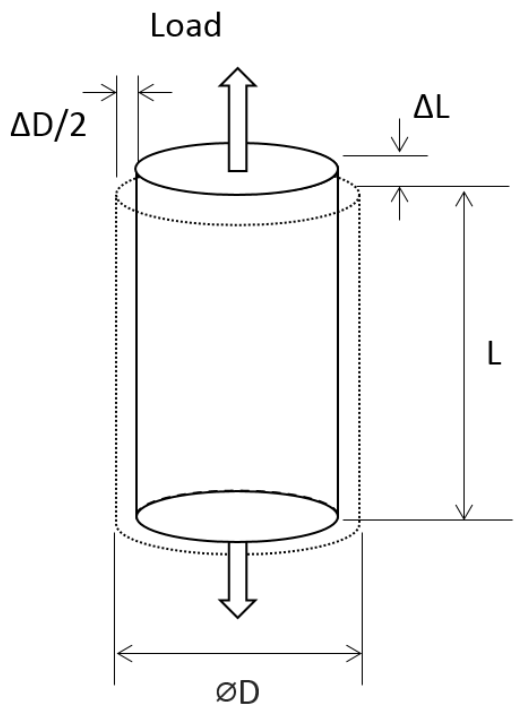

Figure 2.4: Pictorial representation of Poisson's Ratio.

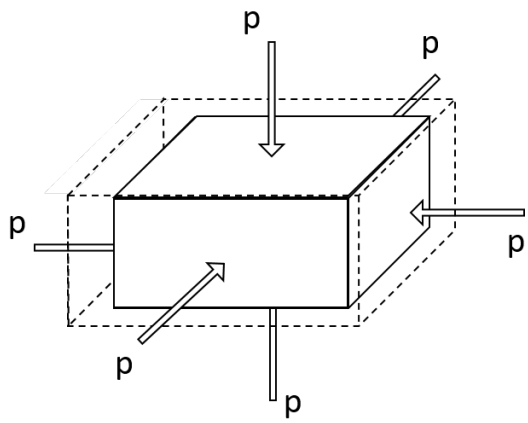

Figure 2.5: Pictorial representation of bulk modulus.

$$G = \frac{E}{2\left(1+\nu\right)} \tag{2.8}$$

The bulk modulus is a measure of the degree to which the volume of a material will change when subjected to uniform compression. Many fundamental expressions exist which can be used to determine the bulk modulus without using Eq. (2.5). Eq. (2.9) is one way to express this as an equation. The hydrostatic stress, σ_h, is the average of the three normal stresses, and the volumetric strain, ϵ_v, is the sum of the three directional strains as determined from Eq. (2.6). A depiction of the phenomenon is shown in Figure 2.5.

$$K = \frac{\sigma_h}{\epsilon_v} = \frac{\frac{\sigma_x+\sigma_y+\sigma_z}{3}}{\epsilon_x+\epsilon_y+\epsilon_z} \tag{2.9}$$

Shear modulus is the shear analogue of Young's modulus. It is the ratio of shear stress, τ_{xy}, to shear strain, γ_{xy}, as depicted in Figure 2.6. This ratio can be found in Eq. (2.10).

$$G = \frac{\tau_{xy}}{\gamma_{xy}} = \frac{F/A}{\Delta x/L} \tag{2.10}$$

The four elastic moduli introduced here are four of the six total. If any two elastic moduli are known for a material, the other four can be determined. Elasticity is a simplifying assumption that has limited application in many instances. All materials will lose elasticity once some yield strength, σ_0, is reached. Loading beyond this point will result in deformation that is not elastic or even failure.

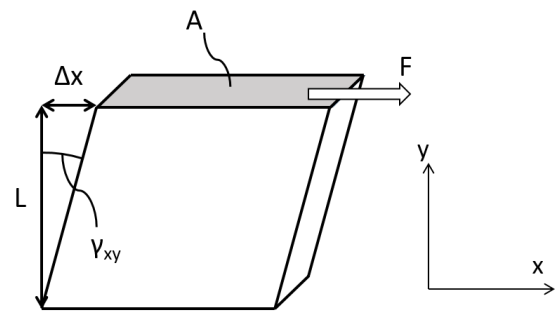

Figure 2.6: Pictorial representation of shear modulus.

2.2.2 Plastic Strain

Permanent deformation is called plastic deformation. The elastic, perfectly-plastic model is a simple plastic model which assumes that a material will behave elastically until some yield strength is reached. The material will then begin deforming while the stress remains at the yield strength. Elastic, perfectly-plastic behavior is represented graphically in Figure 2.7. Prior to unloading, the total strain experienced by the material consists of both elastic strain, ϵ_e, and plastic strain, ϵ_p. Unloading of an elastic, perfectly plastic material will cause recovery of elastic strains, while some permanent, plastic strain will remain.

A select few categories of constitutive models are shown in Figure 2.8. Strain-hardening materials deform plastically after their yield strength is reached, but they are able to support greater loads as they deform. In contrast, materials which exhibit strain-softening behavior will shed load while experiencing plastic deformation. Materials that experience brittle failure lose most or all of their ability to support a load very quickly once their strength is reached.

2.3 Rock Mass Classifications

Rock masses are complex systems with high variation between them, making them difficult to describe quantitatively. Because each rock mass can be described uniquely, a means of classifying rock masses is necessary in order to categorize and group them. This classification, in addition to easing and standardizing communication regarding rock masses, is valuable during the engineering design process.

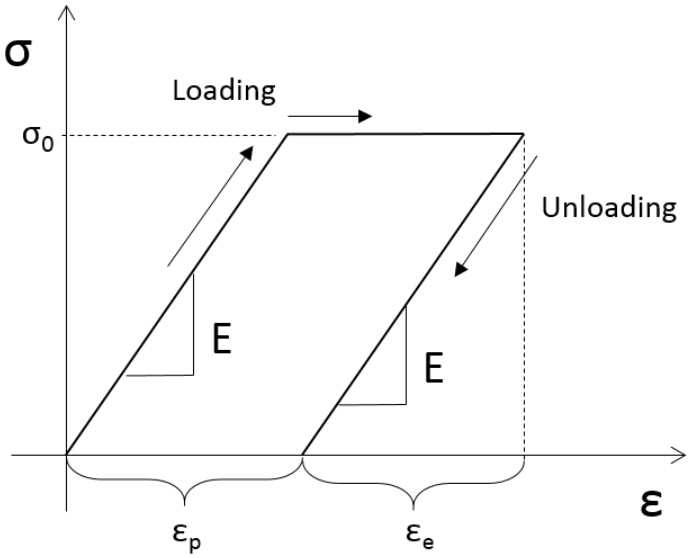

Figure 2.7: Stress-strain curve of elastic, perfectly-plastic loading and unloading.

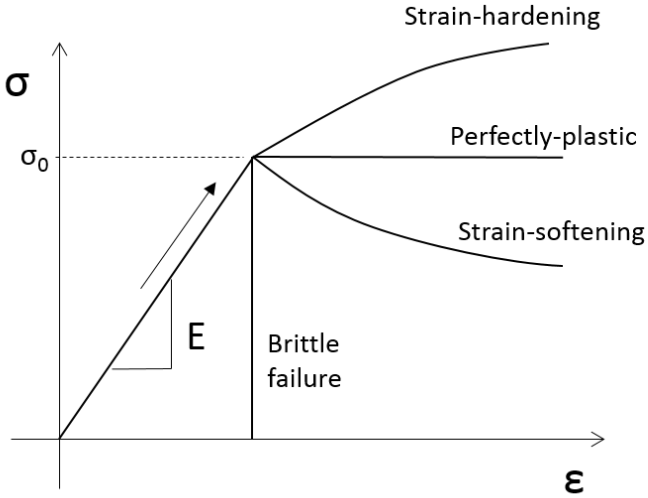

Figure 2.8: Stress-strain curves of multiple elastic, plastic models.

Table 2.1: Qualitative descriptions of rock quality designation ranges as suggested by Deere [3].

RQD %	Qualitative Description
0 - 25	Very Poor
25 - 50	Poor
50 - 75	Fair
75 - 90	Good
90 - 100	Excellent

2.3.1 Rock Quality Designation (RQD)

One of the oldest rock mass classification systems which is still widely used today is the rock quality designation (RQD) system. The RQD system, which was developed as a technique for quantifying the percentage of recoverable core, was first described by Don Deere in 1966 [2]. The RQD value, which is calculated by analyzing core samples, is equal to the ratio of the cumulative length of core greater than 100 mm (4 inches) to the total length of core. Pieces greater than or equal to 4 inches in length are considered to be "sound" core, and smaller pieces are the result of shearing, jointing, faulting, or weathering within the rock mass. In addition to the numerical value of RQD, Deere has categorized ranges of values and suggested qualitative descriptions, as shown in Table 2.1 [3].

When RQD was introduced, there were many existing methods for estimating the core-recovery percentage, but RQD became the standard, and a widely used index of rock quality. The RQD index became a standard because it is easy to measure, easy to calculate, and nondestructive. Because of its applicability and simplicity, it has been incorporated as one input parameter into more involved rock classification systems [4].

2.3.2 Rock Mass Rating (RMR)

One such rock mass classification system which includes the RQD among many other parameters is the rock mass rating (RMR) system. The RMR system was originally called the "Geomechanics Classification" by Bieniawski, its developer. In addition to using previously proven rock mass indices, RMR was designed to be functional and use a variety of important rock and rock mass properties with appropriate weights to value their relative importance properly [5].

Table 2.2: Qualitative descriptions associated with rock masses with RMR ranges as suggested by Bieniawski [6].

Rating	Class no.	Qualitative Description
100 - 81	I	Very Good Rock
80 - 61	II	Good Rock
60 - 41	III	Fair Rock
40 - 21	IV	Poor Rock
< 20	V	Very Poor Rock

Table 2.3: Quantitative estimates of rock mass strength parameters, rock mass cohesion and rock mass friction angle, as well as an expected life of a tunnel through a rock mass based on rock mass rating ranges as suggested by Bieniawski [6].

Class no.	Average stand-up time	Cohesion (kPa)	Friction Angle (°)
I	20 yr for 15-m span	> 400	> 45
II	1 yr for 10-m span	300 - 400	35 - 45
III	1 wk for 5-m span	200 - 300	25 - 35
IV	10 hr for 2.5 -m span	100 - 200	12 - 25
V	30 min for 1-m span	< 100	< 15

The form of the rock mass rating system used today includes six inputs: uniaxial compressive strength, rock quality designation (RQD), discontinuity spacing, condition of discontinuities, presence of groundwater, and orientation of joints. In addition to passionate support of RMR, Bieniawski gave a detailed explanation on how to determine its value here [6]. The RMR system typically takes values between 0 and 100, like the RQD system. But unlike the RQD system, negative values are possible with RMR. Bieniawski groups rock masses within ranges of RMR values and assigns them qualitative descriptions, as well as some reasonable quantitative values, as shown in Tables 2.2 and 2.3.

The RMR system was originally developed as an aide for tunnel design and support selection [5]. While the RMR system has not changed in its essential nature or purpose since its introduction, some modifications were made to it in its first ten to fifteen years in existence. Since its development, the RMR system has been adapted for use in many rock mass design applications including foundations and slopes as well as underground excavations

other than simple tunneling [7].

2.3.3 Tunnel Quality Index (Q)

Developed around the same time as RMR, the Q-System is another rock mass classification technique which is still used today. The Q-System incorporates the RQD value, like RMR, but it also considers the stress state of the rock mass. Typically falling between $Q = 0.001$ and $Q = 1000$ on a logarithmic scale, the Q index is calculated as shown in Eq. (2.11) [8].

$$Q = \frac{RQD}{J_n} \cdot \frac{J_r}{J_a} \cdot \frac{J_w}{SRF} \tag{2.11}$$

where RQD is the rock quality designation, J_n is the joint set number, J_r is the joint roughness number, J_a is the joint alteration number, J_w is the joint water reduction factor, and SRF is the stress reduction factor. The Q-System is not strictly a rock mass classification system. The Q-System may only be applied to an underground opening within a rock mass and not to a rock mass itself. Still in use today, the Q-System was an early attempt to quantify and predict the response of the rock mass to being excavated [9].

2.3.4 Geological Strength Index (GSI)

The Geologic Strength Index (GSI) was introduced in an attempt to overcome some limitations present in the existing classification systems. The GSI index, which ranges from 10 to 100, was created to be a direct input into numerical modeling programs. Existing classification systems were developed to account for factors such as jointing and water content which are dealt with explicitly in modeling softwares, causing such effects to be considered redundantly [10].

The GSI incorporates geologic makeup of the rock mass, as well as some visual characteristics. Specifically, the structure of the rock mass must be defined. Originally, four qualitative descriptions of the rock mass were defined, one of which had to be ascribed to the rock mass. There are a total of six options now to be used for assigning a description to the rock mass structure: intact, block, very blocky, blocky/seamy, disintegrated, and laminated [10]. There are also descriptions given so that all users may arrive at the same or similar conclusions. In addition to the structural component of the rock mass, the surface quality of the must be described as well [11].

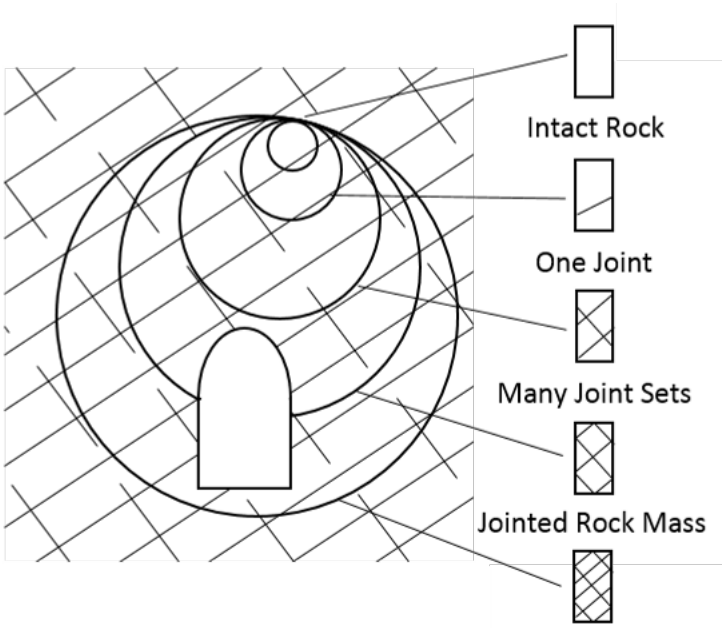

Figure 2.9: Depiction showing the degree of fracturing expected on different length scales in a rock mass. Used under fair use, 1995 [11].

2.4 Failure Criterion

Knowledge of the strength characteristics of in situ rock is required for practical design purposes. The most common means of inferring the strength of rock is lab testing, which is most commonly done on small samples of intact rock. The results of testing intact rock samples in a lab setting cannot be assumed to be valid for rock which is not intact, so some reduction factors are often applied [12]. A cartoon showing relevant scales of rock and the importance of joints is shown in Figure 2.9.

The strength [13, 14, 15, 16, 17] and post-failure behavior [18] of geomaterials depend greatly on the scale considered. Strength testing of intact rock takes many forms and is used ubiquitously in the rock mechanics industry. Testing of rocks with a single joint, whether natural or saw-cut, is also common in laboratories. The strength of a rock sample with a single joint depends greatly on the orientation of the joint. For heavily jointed rock masses, there is often a sufficient number of joints in various directions that the rock mass as a whole can be assumed to act homogeneously [18].

The two most common means of estimating rock strength are the Mohr-Coulomb and

the Hoek-Brown failure criteria. Charles-Augustin de Coulomb developed the Mohr-Coulomb failure criterion in the 18th Century. The Mohr-Coulomb failure criterion gives a simple, linear relationship between shear strength and applied normal stress. The Hoek-Brown failure criteria was adapted from an equation used to estimate the strength of concrete by Evert Hoek and Edwin Brown for analyzing rock in the 1980's [19]. While these two failure criteria are the most commonly used design constraints in rock mechanics, they both ignore the intermediate principal stress, which has been shown to have a significant and predictable effect on failure [20].

2.4.1 Mohr-Coulomb Failure Criterion

The Mohr-Coulomb failure criterion remains one of the most widely used models for predicting the failure of rocks under compression. It is widely used to predict rock failure, because it is simple, intuitive, and accurate under many loading conditions. The Mohr-Coulomb failure criterion predicts the shear strength, $|\tau|$, to be a function of the applied normal stress, σ_n, as shown in Eq. (2.12).

$$|\tau| = \sigma_n \tan\phi + c \tag{2.12}$$

where ϕ and c are empirically derived parameters. The parameter ϕ is called the angle of internal friction, and c is cohesion. The angle of internal friction is analogous to a coefficient of friction, in that the product of it and normal stress create opposition to sliding. Cohesion is the inherent shear strength of the rock, which can prevent failure in cases of pure shearing.

Because this shear strength estimate is a function of normal stress, the equation can be plotted on the same axes as a Mohr's circle, as shown in Figure 2.10. The Mohr's circle plotted in Figure 2.10 represents a state of stress at failure because it is intersecting the failure envelope at the point $(|\tau|, \sigma_n)$. Any Mohr's circle under the failure envelope and not intersecting it, is expected to be stable.

As discussed previously, the Mohr's circle is a graphical representation of a state of stress. Every diameter which can be drawn through the circle represents an orientation of mutually orthogonal axes in that stress state. The horizontal diameter through the circle would intersect at σ_1 and σ_3, the principal stresses. This orientation has a shear stress value of zero. Angles within the Mohr's circle are double that of the actual stress state it is representing. The principal stresses, which are 180° apart on the circle are perpendicular in reality. Furthermore, the plane of failure is θ from the plane on which σ_1 acts, and the

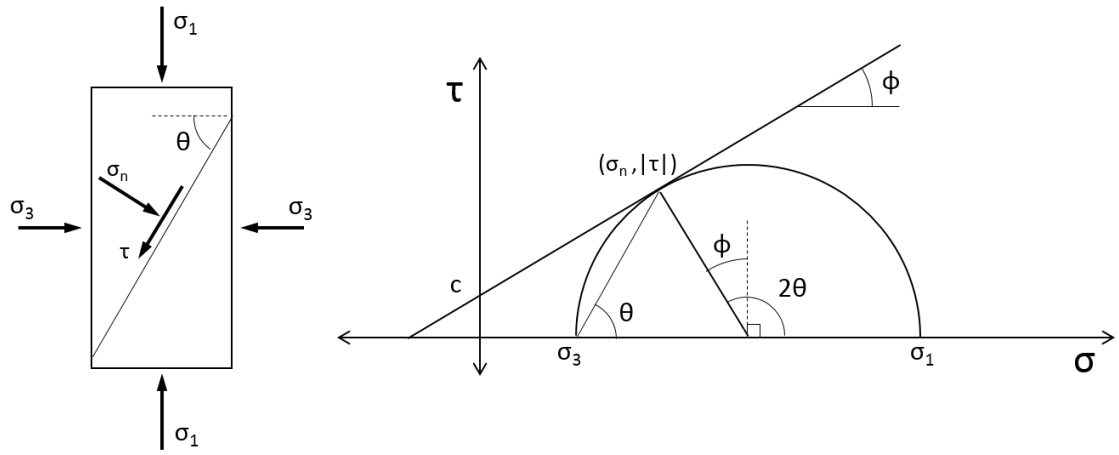

Figure 2.10: Mohr-Coulomb failure envelope plotted with a Mohr's circle representing a state of stress at failure (right). Representative vertical cross-section of a laboratory rock sample with geometry and applied stresses that match the axes plotted to the right (left).

diameter to the point of failure on the Mohr's circle–the point at which the circle intersects the failure plane–is 2θ from the diameter intersecting σ_1.

It is often convenient to express a failure envelope in the stress-space where the three spatial axes are σ_1, σ_2, and σ_3, so that a stress state can be plotted as one point independent of orientation. In the principal stress space, the Mohr-Coulomb failure envelope, shown in Eq. (2.12), can be written conveniently in two forms: one in terms of ϕ (Eq. (2.13)), and one in terms of θ (Eq. (2.14)). Where $2\theta = 90° + \phi$, as can be seen in Figure 2.10.

$$\sigma_1 = \sigma_3 \frac{1 + \sin\phi}{1 - \sin\phi} + 2c\frac{\cos\phi}{1 - \sin\phi} \tag{2.13}$$

$$\sigma_1 = \sigma_3 \tan^2\theta + 2c\tan\theta \tag{2.14}$$

A stable state of stress can reach failure in one of three simple ways: an increase in the maximum principal stress, σ_1, a decrease in the minimum principal stress, σ_3, or the addition of pore pressure. These three paths from a stable stress state to a state of failure are shown in Figure 2.11 with the original state of stress being the dashed circle and the final, failed state being the solid circle. The first two scenarios are fairly straightforward: the stress state changes sufficiently to cause the circle to intersect the failure envelope. The third scenario involving pore pressure involves a new concept. The presence of pore pressure within a

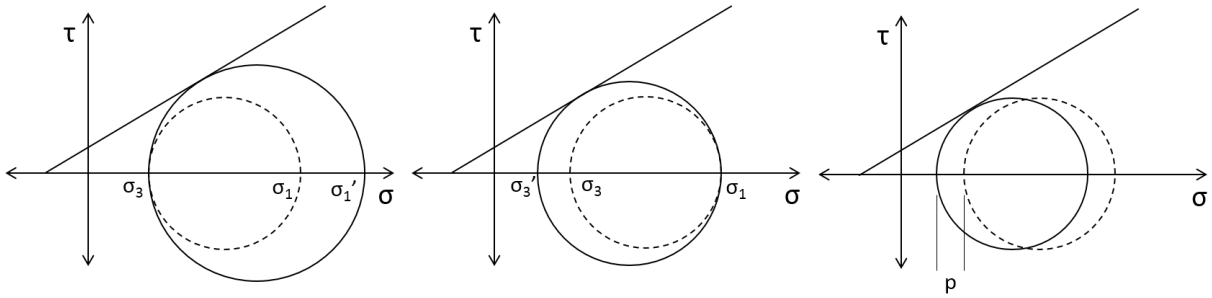

Figure 2.11: Mohr's circle showing progression to failure by increasing σ_1 (left). Mohr's circle showing progression to failure by decreasing σ_3 (center). Mohr's circle showing progression to failure by increasing pore pressure, p, (right).

specimen reduces the effective normal stress by the amount of pore pressure. Graphically, this amounts to sliding the Mohr's circle to the left by an amount equal to the pore pressure without changing the diameter of the circle. The examples shown in Figure 2.11 illustrate the utility of the graphical tool developed by Mohr to accompany the failure criterion developed by Coulomb.

The Mohr-Coulomb failure envelope for intact rock can be determined through laboratory testing. At least four cylindrical rock samples should be held at various confining stresses, typically with $\sigma_2 = \sigma_3$, and loaded until failure. These combinations of principal stresses at failure can then be plotted as Mohr's circles on shear stress vs. normal stress axes. The best-fit line that lies tangent to the Mohr's circles representing stress states at failure is the failure envelope. The material constants, c and θ, can then be determined from the failure envelope [21].

In addition to intact rock, rock with joints can also be analyzed by using the Mohr-Coulomb failure criterion. The consideration of joints adds some complexity to the Mohr-Coulomb model, because the stability of each joint needs to be determined explicitly when the Mohr-Coulomb criterion is used in this way. While it is possible to apply the Mohr-Coulomb failure criterion to rock with joints, it becomes cumbersome with only a few joints if the orientation and strength characteristics of the joints vary [22].

The Mohr-Coulomb failure criterion is simple, effective, and very widely used, but it contains a few inherent flaws due to its simplicity. Because it is an estimate of shear strength, tensile failure is not explained well by the Mohr-Coulomb failure criterion. This is not a serious flaw of the Mohr-Coulomb failure criterion, because all of the widely used failure criteria for rock are focused on the compressive region, and none of them can be extended into the tensile region with confidence [23].

A second significant limitation of the Mohr-Coulomb failure criterion and its application is also a consequence of its simplicity. The failure envelope of many rock types is nonlinear [24]. The shear strength for many rock types is significantly overestimated by the linear Mohr-Coulomb failure envelope in the region with high confining stress. A more general Mohr-Coulomb, $|\tau| = f(\sigma_n)$, form which can be constructed by connecting tangent lines to many Mohr circles at failing stress states can overcome this pitfall, while simultaneously sacrificing the greatest strength of the linear Mohr-Coulomb criterion: its simplicity.

2.4.2 Hoek-Brown Failure Criterion

The Hoek-Brown failure criterion supplies an empirical relationship for predicting failure which is nonlinear. The relationship, shown in Eq. (2.15), was originally developed as a strength criterion for concrete, but was adapted by Hoek and Brown to describe rock failure [19]. Hoek and Brown justified proposing the new relationship, by saying that it is the first rock failure criterion which can simultaneously [25]:

- Be applied to intact rock for any stress conditions which could be expected underground,
- Handle the presence of one or more joint sets within the sample, and
- Provide some insight into rock mass response.

$$\sigma_1 = \sigma_3 + \sqrt{m\sigma_c\sigma_3 + s\sigma_c^2} \tag{2.15}$$

where σ_1 is the maximum principal stress at failure, σ_3 is the minimum principal stress, σ_c is the uniaxial compressive strength of intact rock, and m and s are empirically derived material constants.

One of the first challenges faced and overcome by the Hoek-Brown criterion was the popularity of the Mohr-Coulomb criterion at the time. Software packages and closed-form solutions at the time required the Mohr-Coulomb constants, c and ϕ, as inputs. Relationships between the Mohr-Coulomb constants and the Hoek-Brown constants, m and s, were presented a few years after the Hoek-Brown criterion was introduced. The derived relationship is [18]:

$$\phi = \arctan\left(4h\cos^2\left(\frac{\pi}{6} + \frac{1}{3}\arcsin\left(h^{-3/2}\right)\right) - 1\right)^{-1/2} \tag{2.16}$$

where ϕ is the instantaneous angle of internal friction, and:

$$h = 1 + \frac{16\left(m\sigma + s\sigma_c\right)}{3m^2\sigma_c} \tag{2.17}$$

The Hoek-Brown criterion is meant to be applicable to describe situations where the rock or rock mass behaves isotropically. With appropriate values given to m and s, the Hoek-Brown criterion claims to be able to describe the behavior of intact rock or highly jointed rock masses. It is not recommended, however, to be used to explain the behavior of rock with a single joint or a few joints, because these could not behave isotropically [26].

It was admitted from the start by the developers that an empirical relationship such as the one shown in Eq. (2.15) is only as good as the values chosen for the constants m and s. For easier application, relationships between the constants and the RMR value are given [26]. These values could be applied to rock mass behavior, but not to that of intact rock.

Another significant modification occurred in 1992 when a third fitting parameter was introduced. A modified version of the Hoek-Brown criterion was presented. The failure criterion for intact rock remained unchanged, but a constant, a, was added to that of jointed rock masses, which took the form [27, 28]:

$$\sigma_1 = \sigma_3 + \sigma_c\left(m_b\frac{\sigma_3}{\sigma_c}\right)^a \tag{2.18}$$

The Geological Strength Index was developed, among other reasons, for use with the Hoek-Brown failure criterion. Relationships between the GSI value and the empirical constants m, s, and a have been published. Furthermore, relationships between RMR and GSI and the Q-index and GSI have also been published to make the Hoek-Brown criterion easily accessible in addition to robust [11].

The Hoek-Brown failure criterion has seen widespread application and success in describing the behavior of intact rock and jointed rock masses since its inception. Its nonlinear form has proven to fit more closely to lab data than the Mohr-Coulomb failure criterion. While it does suffer from the need to fit more empirically-derived parameters than the Mohr-Coulomb criterion, the availability of relationships between those constants and well-

established rock mass characterization systems make choosing appropriate values for those constants relatively easy.

2.5 Design of Underground Openings

Design approaches used for underground openings can be characterized as one of three methods: an empirical approach, a rational approach, or an observational approach. The empirical approach depends on the use of knowledge gained from previous case studies. The rational approach requires the development of analytical solutions for the state of stress and strain present in the subsurface during and after excavation. And an observational approach involves extensive monitoring in the form of visual observations during the excavation process so that interventions can be made when necessary to achieve a desired final form. A single design may incorporate any or all of these three [29].

2.5.1 Analysis of Retreat Mining Pillar Stability (ARMPS) [30]

The mining industry necessarily employs an observational strategy at all times. Sophisticated monitoring is used at times, but often it depends simply on visual observations. While the observational strategy is always in use, it is a secondary strategy. Primary design of underground mines has a focus on pillar sizing, which has historically taken an empirical approach [31].

A primary focus of ground control in underground coal mines has long been pillar design. It was long assumed that pillar load could be assumed to be found from the tributary area. Pillar strength was determined from an empirical relationship. The pillar safety factor could then be calculated to predict a satisfactory design [32]. This method could be classified as some hybrid between a empirical strategy–determining pillar strength–and a rational approach–calculating a factor of safety.

When using this design approach, the only variable was in the choice of empirical relationship. Many empirically derived coal pillar strength equations have been produced over the past century. An extensive review of empirical coal pillar strength equations was composed in 1976 [33]. It was clear that the strength of a coal pillar is dependent upon both the size and the shape of the pillar. The dependence of coal pillar strength on shape and size was reiterated in a more recent review of empirically derived strength equations published some twenty years later [34]. A comprehensive list of coal pillar strength equations was

compiled in a recent paper [35], which listed over a dozen equations.

In addition to the difficulty faced when deciding on a strength equation, it was realized that estimating pillar load from the tributary area leads to erroneous results [36]. Assuming the tributary area for finding pillar load results in the theoretical maximum load on the pillar. The actual pillar load is considerably less. Excavating material to create pillars causes some convergence within the seam. The overburden tends to have some capacity to support itself, and the load is instead distributed to barrier pillars, intact rock, and gob.

The Analysis of Retreat Mining Pillar Stability (ARMPS) [30], represents further development into a combination empirical-rational approach to underground coal mine design. ARMPS was formulated from ALPS, Analysis of Longwall Pillar Stability. Since its inception, ARMPS has become an industry standard in the United States.

ARMPS calculates the load on the active mining zone (AMZ), which depends on the loading condition. The strength of the pillars, S_P, is assumed to follow the Mark-Bieniawski pillar strength formula:

$$S_P = 6.2\text{MPa}\left[0.64 + \left(0.54\frac{w}{h} - 0.18\frac{w^2}{hL}\right)\right] \tag{2.19}$$

A stability factor is then calculated, which is the ratio of the load bearing capacity of the pillars within the active mining zone to the load on those pillars. The value of ARMPS is tied to the large database of cases which it uses to set safe thresholds for its stability factor. Rather than assuming a factor of one to be the threshold between unsafe designs and safe ones, ARMPS uses its extensive database to set the threshold at a stability factor of 1.5 [34].

ARMPS uses mine geometry alone to suggest which designs may be stable and which may not be. Overburden thickness, the pillar array, and the loading condition are the only inputs. Its simplicity, ease of use, and large database have led to its ubiquity in underground coal mine design, but it does not include site-specific characteristics.

2.5.2 Ground Response Curve

The convergence-confinement method (CMM), an analytical technique, would be classified as a rational approach to the design of underground openings. The CCM has seen widespread use in civil engineering for determining the response of the subsurface during tunneling. The stress and strain response around the opening can be determined after some simplifying assumptions are made. Originally, those assumptions were [37]:

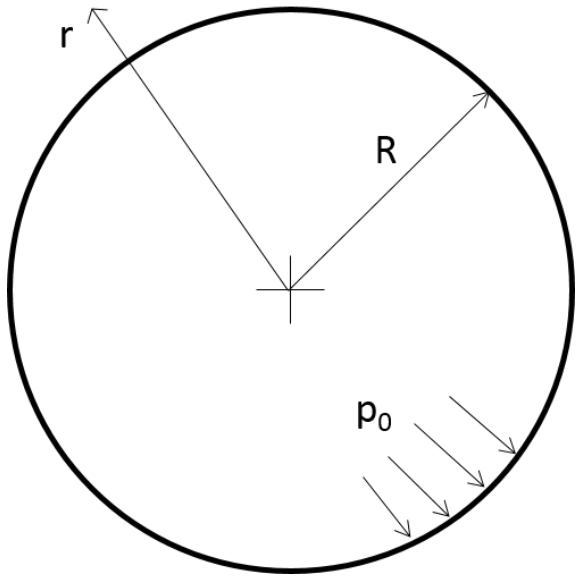

Figure 2.12: Vertical cross-section of a circular tunnel of radius, R, with internal pressure, p_0, which is analyzed for the convergence-confinement method (CM).

- Opening has a circular vertical cross-section
- Stress field is hydrostatic
- Homogeneous and isotropic rock mass

Because of the hydrostatic stress field and the circular opening assumptions, the problem becomes two-dimensional. First in the radial direction, the problem can be depicted in a vertical cross-section, as shown in Figure 2.12. Following the assumption of a hydrostatic stress state, the state of stress in the rock mass prior to excavation is $\sigma_1 = \sigma_2 = \sigma_3 = p_0$, where p_0 is the in situ stress. Rather than being viewed in three orthogonal directions, the CCM approach considers only the internal pressure of the tunnel, p_i, and the external pressure of the tunnel, p_e, where $p_i = p_e = p_0$ prior to excavation. As such, determining the stress and strain response around the opening involves determining the expected radial convergence given a reduction in internal radial pressure.

The solution for determining the stress-strain response in an axial-symmetric element of rock, which was originally published over seventy years ago, can be found here [29]. Solutions for both elastic and elastic-plastic materials are also given. A typical stress-strain

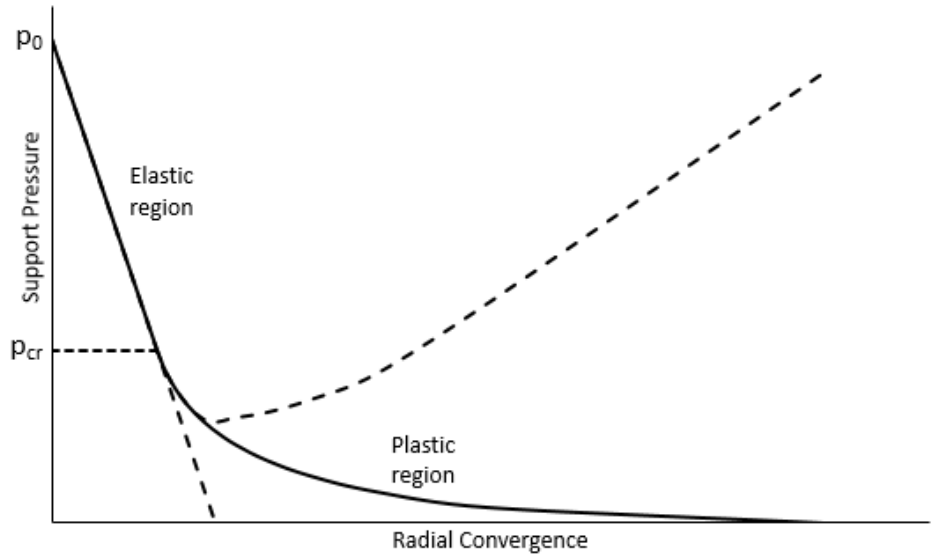

Figure 2.13: Typical ground reaction curve (GRC) as determined via the convergence-confinement method (CCM).

curve representing the response of the rock mass, called the ground response curve (GRC), can be seen in Figure 2.13.

The curve begins on the stress-axis at the value of the in situ stress state, p_0. As the tunnel is being excavated, the pressure inside of the tunnel is reduced, which causes radial convergence. This relationship between internal radial pressure and radial convergence is represented by the GRC.

Convergence of the opening is elastic until some critical pressure, p_{cr}, is reached, after which the convergence becomes plastic. Plastic radial convergence will continue as the internal pressure is reduced until no more support is required to prevent further convergence–represented by the intersection of the GRC with the horizontal axis. It could also be the case that the self-supporting capacity of the rock is lost and the curve would never intersect the horizontal axis. If the critical pressure is never reached, then the response will be purely elastic [38].

Other than considering the radius, the only other relevant spatial dimension with the original simplifying assumptions for the problem is in the direction of the tunnel axis. When the tunnel face is very far from an analyzed region, the internal pressure is equal to the in situ pressure. As the tunnel excavation approaches, the internal radial pressure reduces because of the presence of the excavation. There is a reduction in radial pressure in a region

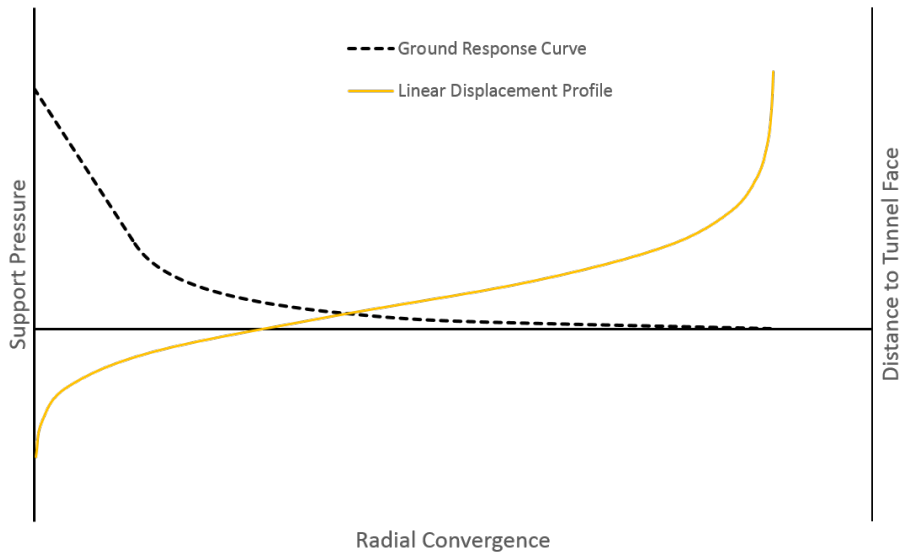

Figure 2.14: Typical ground reaction curve (GRC) and linear displacement profile (LDP) as determined via the convergence-confinement method (CCM).

some distance ahead of the excavation face. The relationship between the axial distance from the excavation face and the radial convergence, called the linear displacement profile (LDP), is shown in Figure 2.14 [39].

The LDP shows that there is radial convergence ahead of the tunnel face. Radial convergence has been measured as much as one radius ahead of the excavation face. This convergence increases steadily up to the excavation face where approximately one-third of the total expected convergence is expected. No more convergence is expected at a greater distance that 1.5 diameters away from the excavation face [11]. These are obviously very rough estimates, especially when considering the fact that not all rock masses have sufficient self-supporting capacity to force intersection of the GRC with the horizontal axis.

Not only is the CCM a relatively easy solution to achieve, the GRC has uses during support selection and installation. The support pressure-radial convergence curve is analogous to a stress-strain curve. The stress-strain characteristic curves of supports may be plotted along with the GRC and LDP on these plots [40].

After a support is installed, its own strain increment will match that of the tunnel. The applied stress on the support will increase according to the support characteristic curve (SCC), which is simply the stress-strain curve of the support. Loading will increase until

either the SCC intersects the GRC or the support fails. When the SCC intersects the GRC, the support is supplying the internal radial pressure required to prevent further convergence, so equilibrium is reached. This relationship between the SCC and GRC has obvious implications for support selection. Furthermore, the LDP gives some indication of the timing available for support installation. Obviously, supports may not be installed until the opening has been excavated. The earliest time available for support installation is dependent upon the mode of excavation in use as well as the support chosen [41].

In addition to the circular, hydrostatic, isotropic solution described here, solutions for many other simplifying assumptions have been determined. Some of the first variations on the original solution were to generalize it to include non-hydrostatic stress states. Initial solutions assumed the rock mass to be a Mohr-Coulomb material [42, 43], but some later solutions involved Hoek-Brown materials [44, 45, 46]. An extensive history of GRC solutions through 1983 are given here [37].

Closed-form solutions nearly exclusively assume a circular vertical cross-section. While this simplifying assumption is applicable in many tunneling operations, it is too simple to be applied to mining. Analytical solutions of increasing complexity are quite rare, and are still limited in application because they are too simple [47].

Using the convergence-confinement method to solve for the ground response curve can only apply to the simplest geometries. And it was originally concerned with determining the ground response due only to a reduction in the internal pressure of the future tunnel related to excavation. Numerical modeling has seen ever increasing use in recent decades because of technological advances made to computing. These numerical models can provide a means of estimating the ground response curve for very complex geometries, while incorporating site-specific characteristics.

A majority of studies related to ground control in mining involving numerical modeling use Itasca's FLAC3D (Fast Lagrangian Analysis of Continua in 3-Dimensions) [48]. FLAC3D is an explicit, finite-difference modeling program. Unlike its competitors, this explicit modeling scheme allows extreme flexibility and accurate results well into the plastic region of material response.

The ground response curve concept has been used to study various loading conditions expected during longwall mining [49, 50, 51]. An excellent example of the power and versatility of numerical models when applied to mining applications is shown in [49]. Numerical models were used in [49] to determine the response in a longwall gate road to increased loading from a passing longwall–a geometry and loading condition far too complex for CCM.

There has been limited study of the ground response in room-and-pillar coal mines using numerical models. [52] used explicitly modeled coal pillars within a panel. The elastic modulus of the pillar material was reduced to determine the response of the surrounding rock at mid-panel.

Difficulties are met when explicitly modeling pillars within a panel-scale model. An element size sufficiently small to represent the pillars to adequate realism would be prohibitively fine at the panel scale. A considerably coarser mesh is typically chosen for models which represent much larger spatial extents. The FLAC3D developers have recommended against using zones of significantly different sizes in a single simulation. The solution scheme used in FLAC3D results in slow execution times when model geometries include zones of significantly different sizes [53].

A method has been proposed which follows pillar behavior on the small-scale, accounts for the panel response on the large-scale, and is computationally reasonable [54]. This study, performed in a trona room-and-pillar mine in Wyoming, details a two-scale approach to modeling room-and-pillar panels. First, the loading response of pillars is simulated in small-scale models. Then, a large, panel-scale model is developed which accounts for the pillar response, but only models the pillar explicitly with a fictitious material.

Works Cited

[1] Norman E Dowling. *Mechanical behavior of materials: engineering methods for deformation, fracture, and fatigue*. Prentice hall, 1993.

[2] DU Deere, AJ Hendron, FD Patton, and EJ Cording. Design of surface and near-surface construction in rock. In *The 8th US Symposium on Rock Mechanics (USRMS)*. American Rock Mechanics Association, 1966.

[3] DU Deere. Geological considerations. *Rock mechanics in engineering practice*, pages 1–20, 1968.

[4] DU Deere and DW Deere. The rock quality designation (RQD) index in practice. In *Symposium on Rock Classification Systems for Engineering Purposes, 1987, Cincinnati, Ohio, USA*, 1988.

[5] ZT Bieniawski. Engineering classification of jointed rock masses. *Civil Engineer in South Africa*, 15(12), 1973.

[6] ZT Bieniawski. The geomechanics classification in rock engineering applications. In *4th ISRM Congress*. International Society for Rock Mechanics, 1979.

[7] ZT Bieniawski. *Engineering rock mass classifications: a complete manual for engineers and geologists in mining, civil, and petroleum engineering*. John Wiley & Sons, 1989.

[8] N. Barton, R. Lien, and J. Lunde. Engineering classification of rock masses for the design of tunnel support. *Rock mechanics*, 6(4):189–236, 1974.

[9] NGI. Using the Q-system: rock mass classification and support design. Norwegian Geotechnical Institute, Oslo, April 2013.

[10] V Marinos, P Marinos, and Evert Hoek. The geological strength index: applications and limitations. *Bulletin of Engineering Geology and the Environment*, 64(1):55–65, 2005.

[11] E Hoek, PK Kaiser, and WF Bawden. *Support of underground excavations in hard rock*. AA Balkema, Rotterdam, 1995.

[12] AJ Hendron. Mechanical properties of rock. *Rock Mechanics in Engineering Practice*, pages 21–53, 1968.

[13] Nick Barton. Shear strength criteria for rock, rock joints, rockfill and rock masses: Problems and some solutions. *Journal of Rock Mechanics and Geotechnical Engineering*, 5(4):249 – 261, 2013.

[14] Nick Barton and Stavros Bandis. Effects of block size on the shear behavior of jointed rock. In *The 23rd US Symposium on Rock Mechanics (USRMS)*. American Rock Mechanics Association, 1982.

[15] Seong-Tae Yi, Min-Su Kim, Jin-Keun Kim, and Jang-Ho Jay Kim. Effect of specimen size on flexural compressive strength of reinforced concrete members. *Cement and Concrete Composites*, 29(3):230–240, 2007.

[16] JN van der Merwe. A laboratory investigation into the effect of specimen size on the strength of coal samples from different areas. *Journal of the South African Institute of Mining and Metallurgy*, 103(5):273–279, 2003.

[17] Z.T. Bieniawski. The effect of specimen size on compressive strength of coal. *International Journal of Rock Mechanics and Mining Sciences & Geomechanics Abstracts*, 5 (4):325 – 335, 1968.

[18] Evert Hoek. Strength of jointed rock masses. *Geotechnique*, 33(3):187–223, 1983.

[19] Evert Hoek and Paul Marinos. A brief history of the development of the Hoek-Brown failure criterion. *Soils and rocks*, 2:1–8, 2007.

[20] GA Wiebols and NGW Cook. An energy criterion for the strength of rock in polyaxial compression. In *International Journal of Rock Mechanics and Mining Sciences & Geomechanics Abstracts*, volume 5 (6), pages 529–549. Elsevier, 1968.

[21] R Ulusay. *The ISRM Suggested Methods for Rock Characterization, Testing and Monitoring: 2007-2014*. Springer, 2015.

[22] Q Xu, J Chen, J Li, C Zhao, and C Yuan. Study on the constitutive model for jointed rock mass. *PloS one*, 10(4), 2015.

[23] ZF Zhang and J Eckert. Unified tensile fracture criterion. *Physical review letters*, 94(9):094301, 2005.

[24] John Conrad Jaeger and Neville GW Cook. *Fundamentals of rock mechanics*. Chapman & Hall, London, 3rd edition, 1979.

[25] Evert Hoek and Edwin T Brown. *Underground excavations in rock*. Institution of Mining and Metallurgy, 1980.

[26] Evert Hoek and Edwin T Brown. The Hoek-Brown failure criterion-a 1988 update. In *Proc. 15th Canadian Rock Mech. Symp*, pages 31–38. Toronto, Dept. Civil Engineering, University of Toronto, 1988.

[27] E Hoek, D Wood, and S Shah. A modified Hoek-Brown failure criterion for jointed rock masses. In *Eurock*, volume 92, pages 209–13, 1992.

[28] Sandip Shah. *A study of the behaviour of jointed rock masses*. PhD thesis, University of Toronto, 1992.

[29] Pierpaolo Oreste. The convergence-confinement method: roles and limits in modern geomechanical tunnel design. *American Journal of Applied Sciences*, 6(4):757, 2009.

[30] C. Mark and F.E. Chase. Analysis of retreat mining pillar stability (armps). In *Proceedings-New Technology for Ground Control in Retreat Mining. Pittsburgh, PA: US Department of Health and Human Services, Public Health Service, Centers for Disease Control and Prevention, National Institute for Occupational Safety and Health, DHHS (NIOSH) Publication*, pages 17–34, 1997.

[31] BN Whittaker, T Unlu, DJ Reddish, and Smith SF. Pillar design aspects for stability in deep coal mines. *Assessment and Prevention of Failure Phenomena in Rock Engineering*, 1993.

[32] C Mark. State-of-the-art in coal pillar design. *Transactions-Society for Mining Metallurgy and Exploration Incorporated*, 308:123–128, 2000.

[33] WA Hustrulid. A review of coal pillar strength formulas. *Rock Mechanics*, 8(2):115–145, 1976.

[34] Christopher Mark and Timothy M Barton. Pillar design and coal strength. In *Proceedings-New Technology for Ground Control in Retreat Mining. Pittsburgh, PA: US Department of Health and Human Services, Public Health Service, Centers for Disease Control and Prevention, National Institute for Occupational Safety and Health, DHHS (NIOSH) Publication*, pages 49–59, 1997.

[35] M Jawed, RK Sinha, and S Sengupta. Chronological development in coal pillar design for bord and pillar workings: A critical appraisal. *Journal of Geology and Mining Research*, 5(1):1–11, 2013.

[36] H Wagner. Pillar design in coal mines. *JS Afr Inst Min Metall*, 80:37–45, 1980.

[37] Edwin T Brown, John W Bray, Branko Ladanyi, and Evert Hoek. Ground response curves for rock tunnels. *Journal of Geotechnical Engineering*, 1983.

[38] Diego Lope Álvarez. Limitations of the ground reaction curve concept for shallow tunnels under anisotropic in-situ stress conditions. Master's thesis, Universitat Politècnica de Catalunya, 2012.

[39] N Vlachopoulos and MS Diederichs. Improved longitudinal displacement profiles for convergence confinement analysis of deep tunnels. *Rock mechanics and rock engineering*, 42(2):131–146, 2009.

[40] Thomas M Barczak. Optimizing secondary roof support with the niosh support technology optimization program (stop). In *Proceedings of 19th International Conference on Ground Control in Mining, Morgantown, WV*, pages 74–84, 2000.

[41] Thomas M Barczak, Thomas P Mucho, and Dennis R Dolinar. Design methodology for standing secondary roof support systems. *Proceedings, New Technology for Coal Mine Roof Support*, pages 133–150, 2000.

[42] JJK Daemen and C Fairhurst. Influence of failed rock properties on tunnel stability. In *The 12th US Symposium on Rock Mechanics (USRMS)*. American Rock Mechanics Association, 1970.

[43] JW Bray. A study of jointed and fractured rock. part ii–theory of limiting equilibrium. *Rock mechanics and engineering geology*, 5(4):197–216, Dec 1964.

[44] C Carranza-Torres and C Fairhurst. Application of the convergence-confinement method of tunnel design to rock masses that satisfy the Hoek-Brown failure criterion. *Tunnelling and Underground Space Technology*, 15(2):187–213, 2000.

[45] C Carranza-Torres and Ch Fairhurst. The elasto-plastic response of underground excavations in rock masses that satisfy the Hoek-Brown failure criterion. *International Journal of Rock Mechanics and Mining Sciences*, 36(6):777–809, 1999.

[46] Kyung-Ho Park, Bituporn Tontavanich, and Joo-Gong Lee. A simple procedure for ground response curve of circular tunnel in elastic-strain softening rock masses. *Tunnelling and Underground Space Technology*, 23(2):151–159, 2008.

[47] H Yavuz. Support pressure estimation for circular and non-circular openings based on a parametric numerical modelling study. *Journal-South African Institute Mining and Metallurgy*, 106(2):129, 2006.

[48] Itasca Consulting Group, Inc., Minnesota. *Fast Lagrangian Analysis of Continua in 3-Dimensions, version 5.0, manual*, 2013.

[49] Essie Esterhuizen and Tom Barczak. Development of ground response curves for longwall tailgate support design. In *Golden Rocks 2006, The 41st US Symposium on Rock Mechanics (USRMS)*. American Rock Mechanics Association, 2006.

[50] Thomas M Barczak. A retrospective assessment of longwall roof support with a focus on challenging accepted roof support concepts and design premises. In *Proceedings of the 25th international conference on ground control in mining, Morgantown, WV*, pages 232–243, 2006.

[51] Thomas M Barczak, GS Esterhuizen, John Ellenberger, and P Zhang. A first step in developing standing roof support design criteria based on ground reaction data for Pittsburgh seam longwall tailgate support. In *Proceedings of the 27th International Conference on Ground Control in Mining*, pages 349–359, 2008.

[52] Essie Esterhuizen, Chris Mark, and Michael Murphy. The ground response curve, pillar loading and pillar failure in coal mines. In *29th International Conference on Ground Control in Mining*, 2010.

[53] Inc. Itasca Consulting Group. Flac3d training course - basic concepts and recommended procedures, 2015.

[54] M Board, B Damjanac, and M Pierce. Development of a methodology for analysis of instability in room and pillar mines. In *Deep Mine 07, Proceedings of the Fourth International Seminar on Deep and High Stress Mining*, pages 273–282. Perth, Australia, 2007.

Chapter 3

Modeling the Ground Response Curve for a Room-and-Pillar Coal Panel

3.1 Abstract

The response of the overburden to excavations made within a coal seam has significant implications on the stability of mine workings. A useful tool for analyzing the reponse of a rock mass to underground excavations, called the ground response curve, was developed for the tunneling industry approximately seventy years ago. While mine geometries are far too compex for analytical solutions to the ground response curve to be developed, numerical modeling may be used instead. Numerical modeling is used in this study to solve for the ground response curve for a room-and-pillar coal mine panel in the eastern US. The ground response curves obtained are compared to stress-strain curves for pillars within the panel to estimate panel stability.

3.2 Introduction

Coal mines provide a unique set of challenges toward safe design. The complexity arises from the soft nature of coal and the high variability among coal measure rocks. The rock types present around coal seams often range from strong, competent sandstones to weak, laminated shales. Ground control in these environments begins with pillar sizing. Larger pillars obviously offer more support, but at the cost of leaving a valuable resource underground.

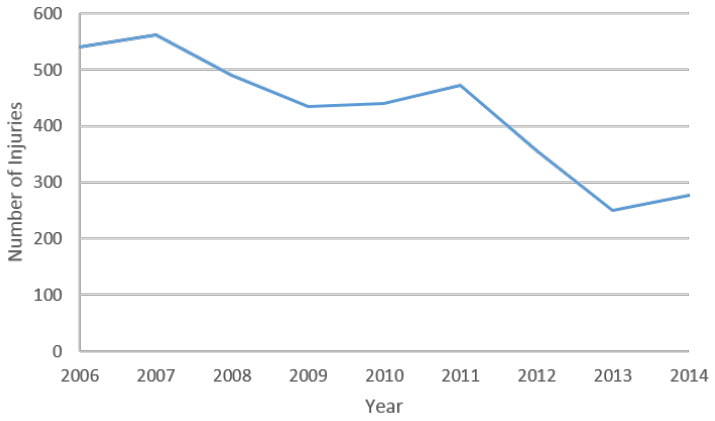

Figure 3.1: Injuries due to fall of roof or rib between 2006 and 2014. This includes fatal injuries, non-fatal injuries with days lost, and injuries with no days lost [1].

Ground control is a primary design consideration during the development of underground coal mines. Poor ground conditions can negatively affect ventilation and haulage. Extremely poor ground conditions or poor designs can result in catastrophe. Over 16% of all reported incidents in underground coal mines from 2006 to 2014 were due to fall of roof or rib [1]. A chart of the total number of injuries attributed to ground control issues in underground coal mines in the US is shown in Figure 3.1. There has been a downward trend in the number of incidents of late, but safer conditions are certainly possible.

The ground response curve is a useful tool to aid in understanding the stability of underground openings. Developed for the tunneling industry, the ground response curve was originally determined using the convergence-confinement method (CCM). In its original form, CCM simply predicted the relationship between reduced radial pressure inside of a tunnel due to excavation and the radial convergence of that excavation [2]. A depiction of a ground response curve is shown in Figure 3.2.

Ground response curves (GRC) are plotted on pressure-convergence axes. The curve begins on the pressure-axis at a value equal to the in situ stress state. As the internal pressure of the rock mass is reduced due to an approaching excavation, convergence is expected. The GRC represents the internal pressure required to prevent further convergence. The curve has great utility for estimating not only the self-supporting strength of an underground opening, but also the type of support which should be applied [3].

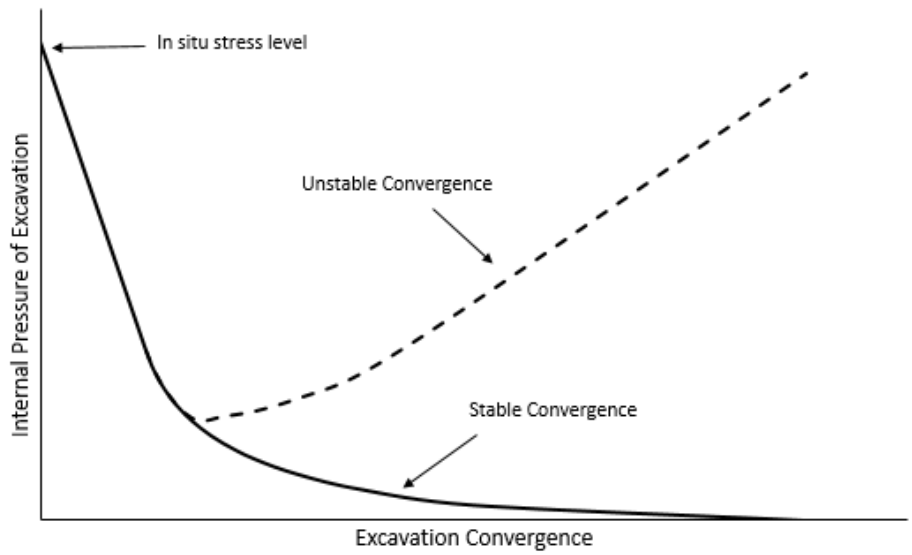

Figure 3.2: Ground reaction curve (GRC) with two possible outcomes shown. The solid line represents stable convergence, and the dashed line represents unstable convergence.

The convergence-confinement method (CCM), when applied to circular tunnels, often predicts stable convergence [2]. Stable convergence is represented by the solid line-type in Figure 3.2. The curve with the solid line-type shows convergence associated with an underground opening which has sufficient self-supporting capacity to limit convergence naturally. That is, without the installation of artificial support, the total convergence of the excavation is expected to be the intersection of the GRC and the convergence-axis, where internal pressure is zero.

Working sections in retreating room-and-pillar mines are not expected to experience stable convergence [4]. The dashed line-type in Figure 3.2 shows an underground opening which is expected to experience unstable convergence. The minimum point in the curve represents a loss of self-supporting capacity of the rock mass around the excavation. Full collapse of the opening is expected after the rock mass no longer has the integrity to support its own weight. This is represented by the increasing slope of the GRC where the internal pressure required to prevent future convergence approaches the original lithostatic stress.

The geometry of underground mine openings tends to be far more complex than those in the tunneling industry. However, the ground response curve concept may still be applied. Analytical solutions for the ground response curve are often not possible for mining scenarios, but the curve itself may still be determined through numerical modeling [5]. The numerical

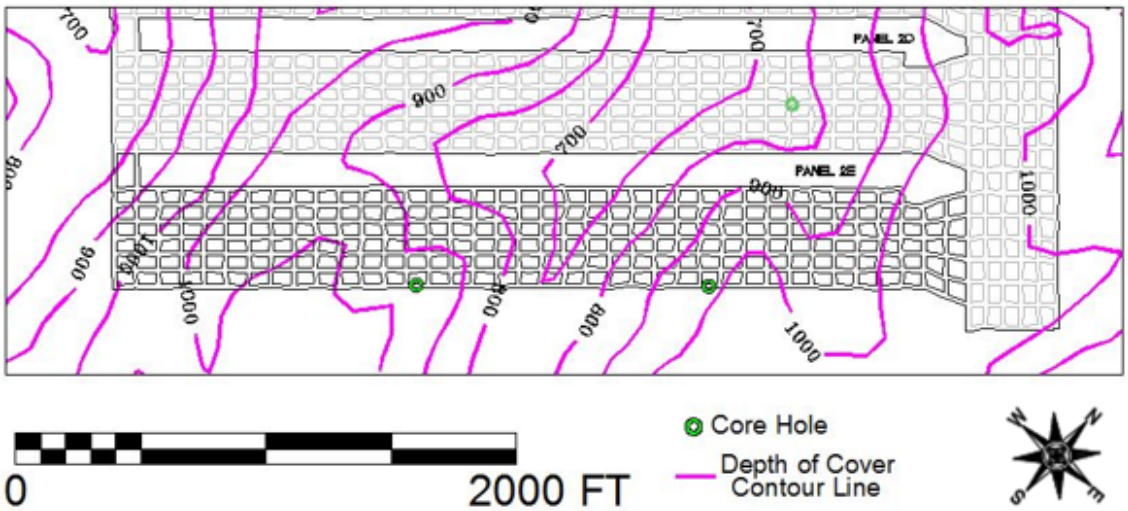

Figure 3.3: Contour map showing depth of cover over room-and-pillar panel 2E. The marked drillhole locations represent the locations of the two holes drilled into the roof for installation of the seismic array from which core samples were collected and tested for rock mechanics properties.

modeling performed in this study was completed in FLAC3D [6]

3.3 Site Description

This study included characteristics specific to a room-and-pillar coal mine located in the central Appalachian coal fields of the Eastern United States. The room-and-pillar mine panel studied here was numbered "Panel 2E" by the mine operators. As shown in Figure 3.3, the depth of cover over Panel 2E ranged from approximately 700 to 1000 feet. Panel 2E was a seven-entry panel containing rectangular pillars. Entries were cut to a height between six and seven feet. The barrier pillars on either side are approximately 140-feet wide.

The mined seam was the Jawbone. Coal thickness in the studied mine sections was approximately five feet, and approximately six inches of parting was present. Rib sloughage was commonly observed to occur to a depth of six inches to a foot into the rib. The sloughage was likely due to the degree of fracturing within the seam, which is depicted in Figure 3.4.

Both the roof and floor are comprised of shaley material. Two holes were drilled into the roof for the installation of triaxial geophones. The location of the holes that were drilled is shown in Figure 3.3. Core samples of the roof were collected during the drilling of these

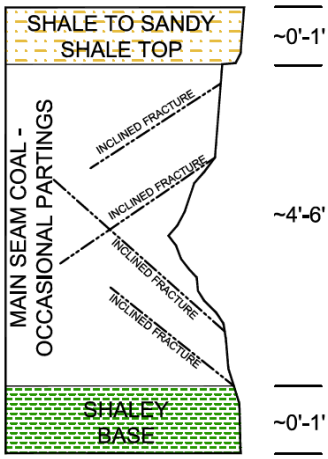

Figure 3.4: Depiction of the inclined fractures observed within the Jawbone seam in the studied panel. Also shown is the typical roof and floor material.

holes, and testing for rock strength characteristics was performed. The mechanical properties obtained from lab testing are shown in Table 3.1.

While not shown in Table 3.1, variation in the strength of the roof material was observed during sample preparation and lab testing. Variation in the strength characteristic was attributed to the variation in the sand content present in the roof material. A detailed discussion of the testing procedures and results can be found in Appendix A.

Only the immediate roof was subjected to laboratory testing. Characteristics of all other strata overlying the studied seam were assumed from core holes drilled from the surface before mine development began. A geologic column representing the findings of the exploratory drilling is shown in Figure 3.5.

The lab testing as well as this numerical modeling study are part of a larger study which involves passive microseismic monitoring during pillar recovery of one of the panels. The core samples were retrieved from holes which were drilled primarily for the installation of a seismic network. Details of the microseismic study, as well as a more in-depth discussion of the site and its geology can be found here [7].

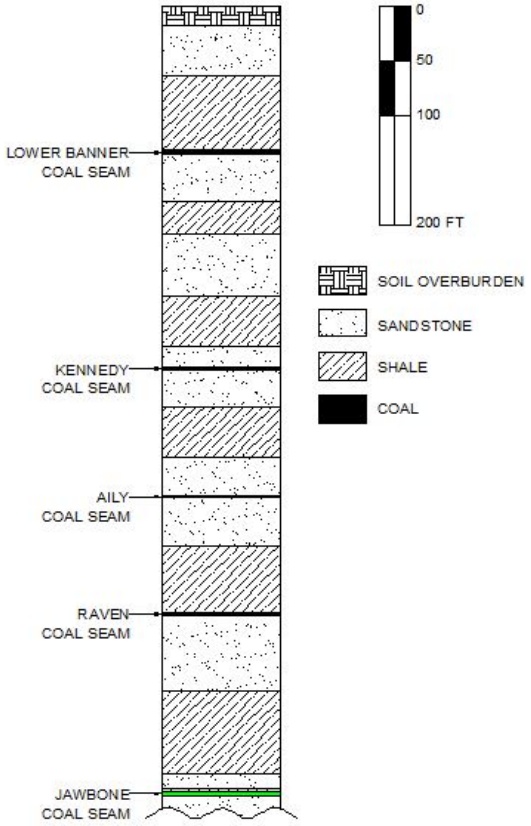

Figure 3.5: Geologic column summarizing the cores collected from Core Hole 679, which was drilled directly above Panel 2D prior to mine development. More information on Panel 2D can be found in Chapter 4.

Table 3.1: Material properties of the roof rock as determined from a series of laboratory tests. Details of the laboratory testing can be found in Appendix A.

Parameter	Unit	Value
Density	kg/m^3	2670
Young's modulus	GPa	23.2
Compressive strength	MPa	142
Tensile strength	MPa	7.84
Cohesion	MPa	37.5
Angle of internal friction	°	30

3.4 Modeling the GRC

Material properties obtained from laboratory testing should not be used as direct inputs into numerical models of large-scale rock mass behavior. Rock masses are often highly fractured, and samples obtained from rock masses that are suitable for laboratory testing exhibit behavior that is not representative of the rock mass as a whole. For this reason, adjustments were made to the mechanical properties found in the laboratory to obtain reasonable values for the rock mass.

The properties of the shale material which were used to model the overburden response come from both laboratory testing and the literature. The uniaxial compressive strength, Young's modulus, and the angle of internal friction calculated from laboratory testing matched values found in the literature for strong shale. Additional material properties required for numerical modeling were assumed to follow those found in the literature which are associated with the strong shale [8]. A list of the material property values used to model the shale roof can be found in Table 3.2.

Weaker laminations were obviously present in the core samples obtained from one of the holes drilled. The material properties listed in Table 3.2 were not assumed to be accurate for the immediate roof above the entire panel. The weaker laminations present in some of the roof material were represented in the models by reducing the properties of the implicitly modeled joints.

Table 3.2: First estimate of material properties of the roof rock used in numerical models. The values listed are obtained from laboratory testing or literature available on numerical modeling input parameters.

Parameter	Unit	Value
Young's modulus	GPa	23.2
Compressive strength	MPa	80
Angle of internal friction	°	30
Cohesion	MPa	14.8
Tensile strength	MPa	4.6
Bedding friction angle	°	10
Bedding cohesion	MPa	2.96
Bedding tensile strength	MPa	0.46

3.4.1 The Pillar Response

Small-scale pillar models were constructed with representative materials of the roof and floor. Coal was modeled as a Hoek-Brown material, while the roof and floor were modeled using the ubiquitous joint constitutive model. These models were loaded while the stress-strain response of the pillar material was measured and recorded.

A range of reasonable properties of the coal material were found in the literature [8, 9]. Values throughout this range were tested as inputs into the numerical models and the stress-strain response was measured. Model calibration at this stage was performed by comparing the peak strength of various square pillar dimensions against the empirical Bieniawski pillar strength equation [10]:

$$S_P = S_i \left[0.64 + 0.36 \frac{W_p}{H_p} \right] \tag{3.1}$$

Square pillars with width-to-height ratios of 6 and 8 were tested in this way to find appropriate values for coal as a Hoek-Brown material. These pillars were modeled with an elastic roof and floor to focus on the coal material, and to minimize the effect of the surrounding material. The stress-strain curves of the two pillar dimensions tested are shown in Figure 3.6. The peak strength values obtained are within approximately ten percent of

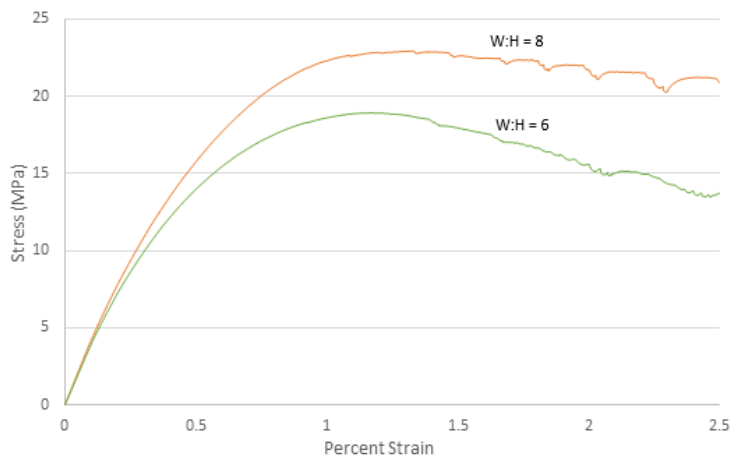

Figure 3.6: Stress-strain response of the two square pillars–of width to height ratios equal to six and eight–with elastic roof and floor.

the values suggested by Eq. (3.1).

After finding appropriate coal material properties, those material properties were modeled with a more realistic roof and floor material. The roof and floor were modeled as jointed Mohr-Coulomb materials by using the ubiquitous joint constitutive model within FLAC3D. The material properties listed in Table 3.2 were used as inputs. The ubiquitous joint constitutive model considers the effect of a specified joint strength and orientation anywhere within the roof and floor material without explicitly representing any joints.

A pillar matching those cut in the room-and-pillar Panel 2E was modeled in FLAC3D with ubiquitously jointed shale material as the roof and floor while the stress-strain response was recorded. The stress-strain curve of this pillar is shown in Figure 3.7. Stress and strain values were calculated as averages over the entire pillar area.

Calibration of the model was performed at this stage in two forms. The pillar peak strength was matched to the Mark-Bieniawski empirical pillar strength relationship [11]. The pillar response was also matched to underground observations. Visual observations were limited in Panel 2E to the degree of rib sloughage. Rib sloughage of six inches to one foot was commonly reported throughout the panel. This rib sloughage was matched to the failed state of the pillar-scale models.

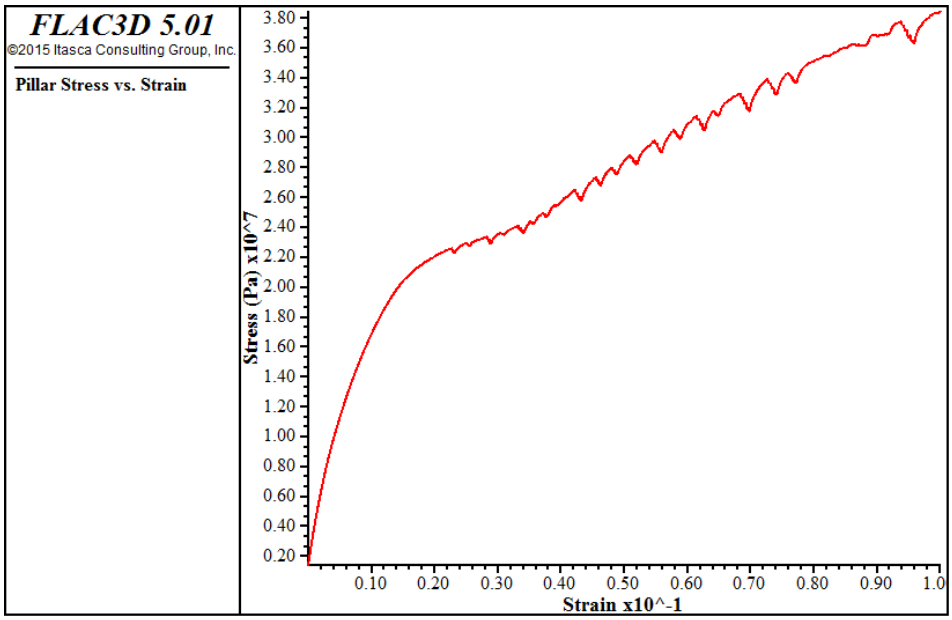

Figure 3.7: Stress-strain response of a rectangular pillar with roof and floor properties listed in Table 3.2.

3.4.2 The Overburden Response

The response of the overburden to excavations made within the seam was modeled by constructing thin vertical cross-sections of the rock mass. These vertical cross-sections included material from the floor up to the surface. The models were allowed to reach equilibrium with gravity loading and horizontal stresses considered. The vertical pressure within the seam was then reduced gradually to represent excavation of the openings. The vertical pressure of the roof on the seam as well as the convergence of the seam was measured throughout the excavation process. An example ground response curve as obtained from this modeling method is shown in Figure 3.8.

Roof and floor material was assumed to follow the built-in ubiquitous joint constitutive model in FLAC3D. A user-defined joint strength and orientation is considered implicitly throughout the modeled roof and floor material. The ubiquitous joint model is the most efficient method for including the presence of a series of joints or laminations in FLAC3D.

The curve starts as the in situ vertical stress value on the internal pressure-axis. As the internal pressure within the seam is reduced, convergence occurs. This curve never reaches the horizontal axis, so unstable convergence is expected.

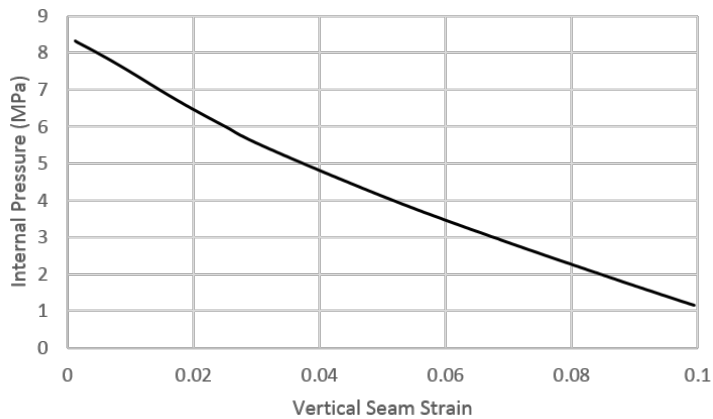

Figure 3.8: Ground response curve of Panel 2E.

3.5 Results and Discussion

The ground response curve is a useful tool for analyzing the stability of underground excavations. While unstable convergence is predicted from the curve obtained here, this is only expected to occur after full extraction. Further convergence can be prevented at any point with the application of a vertical stress which matches that described by the curve.

An altered pillar stress-strain response curve is plotted superimposed on the GRC in Figure 3.9. The stress-strain response of the pillar is reduced by a factor of $(1 - ER)$, where ER is the extraction ratio of the panel. This is done to average the stress a pillar applies to the roof over the entire tributary area.

Convergence within the mined-out panel is expected to stop at the intersection point of the altered pillar stress-strain curve and the ground response curve. At this point, the pillars are supplying the internal pressure required to prevent further convergence of the excavation.

3.6 Conclusions

The ground response curve of the rock mass surrounding a room-and-pillar coal mine has been estimated using FLAC3D. The GRC was estimated by gradual reduction of the pressure within the future underground opening. This method is a similar procedure to the analytical solution determined from the convergence-confinement method.

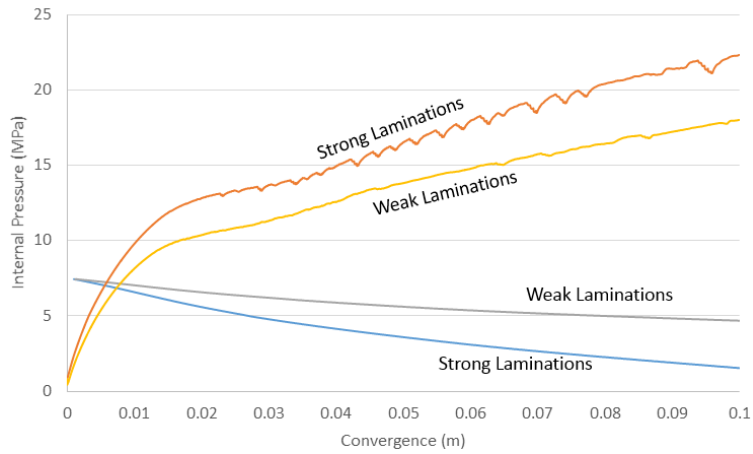

Figure 3.9: Ground response curve of Panel 2E plotted along with the altered stress-strain response of a pillar within the panel for both the shale with weak laminations and the shale with strong laminations.

The ground response curve represents the response of the overburden to excavations within the coal seam. It has major implications for panel stability. The ground response curve obtained from this numerical modeling study predicts full collapse of the mine opening by full extraction.

The stress-strain response of the pillars were plotted on the same set of axes as the ground response curve. At the intersection point between the pillar stress-strain curve and the ground response curve, convergence is expected to cease. This is because the pillar is supplying the required internal pressure to prevent further convergence of the panel.

3.7 Acknowledgment

This work was supported by NIOSH (contract 200-2011-40313) through the Capacity Building and Ground Control Research for the Mining Industry initiative.

Works Cited

[1] Mine safety and health administration.

[2] Edwin T Brown, John W Bray, Branko Ladanyi, and Evert Hoek. Ground response curves for rock tunnels. *Journal of Geotechnical Engineering*, 1983.

[3] Pierpaolo Oreste. The convergence-confinement method: roles and limits in modern geomechanical tunnel design. *American Journal of Applied Sciences*, 6(4):757, 2009.

[4] B Damjanac, M Pierce, and M Board. Methodology for stability analysis of large room-and-pillar panels. In *48th US Rock Mechanics/Geomechanics Symposium*. American Rock Mechanics Association, 2014.

[5] Essie Esterhuizen, Chris Mark, and Michael Murphy. The ground response curve, pillar loading and pillar failure in coal mines. In *29th International Conference on Ground Control in Mining*, 2010.

[6] Itasca Consulting Group, Inc., Minnesota. *Fast Lagrangian Analysis of Continua in 3-Dimensions, version 5.0, manual*, 2013.

[7] William J Conrad. Microseismic monitoring of a room and pillar retreat coal mine in southwest virginia. Master's thesis, Virginia Polytechnic Institute and State University (Virginia Tech), 2016.

[8] Essie Esterhuizen, Chris Mark, and Michael M Murphy. Numerical model calibration for simulating coal pillars, gob and overburden response. In *Proceeding of the 29th international conference on ground control in mining, Morgantown, WV*, pages 46–57, 2010.

[9] Jienan Pan, Zhaoping Meng, Quanlin Hou, Yiwen Ju, and Yunxing Cao. Coal strength and young's modulus related to coal rank, compressional velocity and maceral composition. *Journal of Structural Geology*, 54:129–135, 2013.

[10] Z.T. Bieniawski. The effect of specimen size on compressive strength of coal. *International Journal of Rock Mechanics and Mining Sciences & Geomechanics Abstracts*, 5 (4):325 – 335, 1968.

[11] C. Mark and F.E. Chase. Analysis of retreat mining pillar stability (armps). In *Proceedings-New Technology for Ground Control in Retreat Mining. Pittsburgh, PA: US Department of Health and Human Services, Public Health Service, Centers for Disease*

Control and Prevention, National Institute for Occupational Safety and Health, DHHS (NIOSH) Publication, pages 17–34, 1997.

Chapter 4

Two-Scale Modeling of a Room-and-Pillar Coal Mine Panel

4.1 Abstract

Variations within the material properties of the strata overlying a coal seam can result in significantly different stress magnitudes applied to the pillars in a room-and-pillar mine. For this reason, site-specific characteristics should be incorporated into the ground control design of underground coal mines. A two-scale modeling approach is outlined, which allows for large-scale, site-specific characteristics to be considered when assessing pillar stability. The two-scale modeling approach uses pillar-scale behavior in panel-scale models in a computationally efficient manner. The results compare well with those of ARMPS, and the modeling approach can be catered to any site.

4.2 Introduction

Energy demands are expected to remain constant or increase slightly over the next few years [1]. Combustion of coal leads to a significant portion of the energy production in the United States. Approximately 40% of all coal produced comes from underground mines, and approximately 40% of all coal produced from underground mines comes from room-and-pillar mines [2].

Coal mines are of particular interest and complexity due to the soft nature of coal and

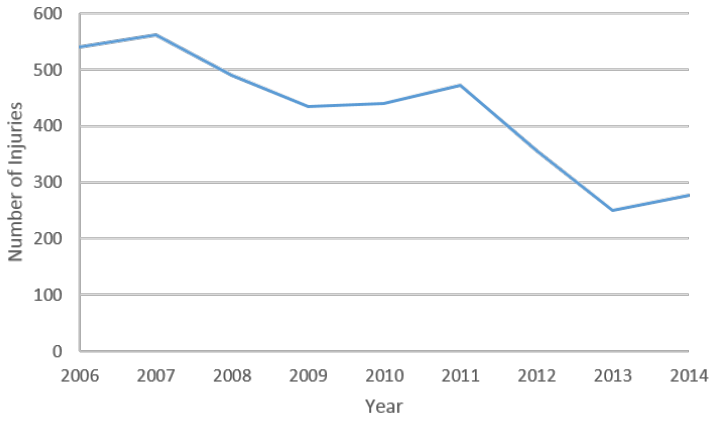

Figure 4.1: Injuries due to fall of roof or rib between 2006 and 2014. This includes fatal injuries, non-fatal injuries with days lost, and injuries with no days lost [3].

highly variable, often laminated rock present above and below coal seams. Underground coal mine ground control starts with proper pillar sizing. Larger pillars, while offering more support, reduce coal production. The sizing of pillars, more than any other design consideration, is a balance between revenue and cost.

Control of the ground is a primary design consideration during the development of underground coal mines. Poor ground conditions will at least add cost to ventilation and haulage needs. Increasingly bad ground conditions can prevent future raw material extraction or even cause injury or death to mine workers. Over 16% of all reported incidents in underground coal mines from 2006 to 2014 were due to fall of roof or rib [3]. A chart of the total number of injuries attributed to ground control issues in underground coal mines in the US is shown in Figure 4.1. There has been a downward trend in the number of incidents of late, but safer conditions are certainly possible.

Room-and-pillar coal mine stability has two scales to consider. Stability must be maintained at the pillar scale and at the mine-wide scale. Mine-wide stability is largely a function of the response of the overburden to excavations made within the panel. Pillar sizing and the performance of the pillars has great implications on panel stability [4].

Numerical modeling was performed to explore the interaction between the overburden and the pillars on a large, panel-wide scale. To accomplish this, the interaction between the roof, pillars, and the floor was first studied on a small scale. The results of these pillar-scale

models were then used in a panel-scale study to assess mine-wide stability. This two-step approach allows for computationally efficient modeling while considering both the small scale and the large scale [5].

4.3 Overview of Two-Scale Modeling Approach

A two-scale modeling approach for modeling room-and-pillar mines in FLAC3D has been suggested in the literature [5]. This approach is ideal for analyzing the interaction between the large-scale and the small-scale responses during excavation. The two-scale approach has been used to estimate the stress on pillars in a room-and-pillar trona mine. The ground response curve has also determined using this method.

A computationally efficient room-and-pillar panel-scale model requires discretization too coarse for accurate representation of the pillar scale. Accurate representation of pillar-scale behavior in a room-and-pillar mine requires discretization too fine to be extended to large-scale models while remaining computationally efficient. The two-scale modeling approach employed here allows for pillar-scale behavior to be represented in a panel-scale model in a computationally efficient manner.

This two-scale, two-step approach starts with a pillar-scale model. Coal pillar behavior depends greatly on the shape and size of the pillar itself, as well as the interaction between the coal and the roof and floor material. To represent the coal pillar behavior accurately, a coal pillar is modeled along with sufficient extent of roof and floor material. These models are loaded until failure. During loading, the stress-strain response of the roof-pillar-floor system was recorded. Calibration of the pillar-scale model took place at this stage by matching model outputs to observations made underground.

The stress-strain curve recorded during pillar loading at the small-scale is later used to represent the seam in a large-scale model. Many shapes and sizes of pillars are often used for room-and-pillar mines, which are all expected to behave differently when loaded. Each pillar in a room-and-pillar panel need not be modeled independently. Instead, unique patterns of pillars should be identified and modeled. Each pillar pattern which is modeled has a spatial extent to which it may be assumed to represent similar pillars in a reasonable manner. If pillar shape and size are uniform in a room-and-pillar panel and the roof and floor conditions are consistent, then only one small-scale model is required. If not, multiple pillar patterns should be modeled with their corresponding roof and floor conditions.

The stress-strain curves obtained during these small-scale models may then be used as

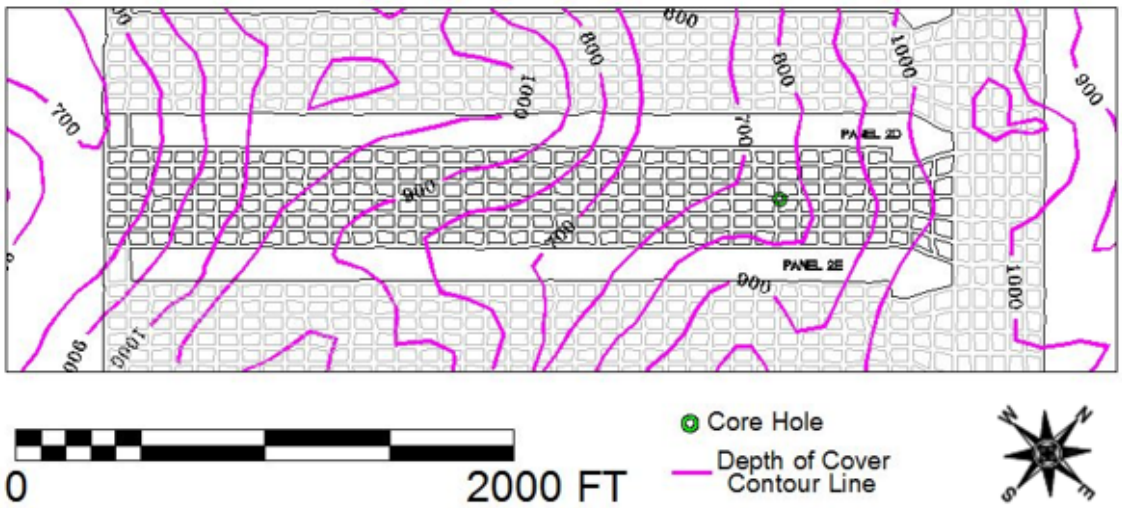

Figure 4.2: Contour map showing depth of cover over room-and-pillar panel 2D, center frame. The drillhole location marked is Core Hole 679, which was drilled from the surface prior to mine development.

inputs in larger scale models. Instead of representing pillar geometry explicitly, which would require a discretization too fine to be computationally reasonable, the material within the coal seam is modeled using a fictitious material which is made to represent the mined-out coal seam. The fictitious material used to represent the coal seam acts as a surrogate for the small-scale room-and-pillar geometry. It responds as the actual seam is expected to during the excavation process while allowing coarse enough discretization to be computationally efficient in large-scale models.

4.4 Site Description

This study included characteristics specific to a room-and-pillar coal mine located in the central Appalachian coal fields of the Eastern United States. As shown in Figure 4.2, the depth of cover over the studied panel ranged from approximately 700 to almost 1100 feet. The panel which was the focus of this study is denoted "Panel 2D" by the mine operators. Panel 2D was a seven-entry panel with rectangular pillars. The barrier pillars on either side of Panel 2D are approximately 140-feet wide.

A core hole was drilled from the surface directly above Panel 2D prior to the development of the mine. The location of this exploratory core hole, Core Hole 679, is shown in Figure

Table 4.1: Material properties of the roof rock as determined from a series of laboratory tests. Details of the laboratory testing can be found in Appendix A.

Parameter	Unit	Value
Density	kg/m^3	2670
Young's modulus	GPa	23.2
Compressive strength	MPa	142
Tensile strength	MPa	7.84
Cohesion	MPa	37.5
Angle of internal friction	°	30

4.2. The cores obtained from the hole show that the strata overlying the coal seam are alternating layers of shale and sandstone. A geologic column summarizing the content of the cores collected form Core Hole 679 is shown in Figure 4.3.

Extraction took place from the Jawbone seam, shown near the bottom of the geologic column shown in Figure 4.3. The coal seam is approximately five feet thick within the panel, not including about half of a foot of parting. The cut height ranged from six to seven feet.

The coal shows a moderate to high degree of fracturing. Persistent fractures present within the Jawbone seam are depicted in Figure 4.4. Rib sloughage from six inches to a foot was observed throughout Panel 2D. The rib sloughage is attributed to the degree of fracturing of the coal in the Jawbone seam. Visual observations within the mine were limited to the degree of sloughage of the ribs

Roof and floor conditions varied somewhat. Both the roof and floor often contained shaley material, and the sand content of the roof varied throughout the studied region. Samples were collected from two holes drilled into the roof from an adjacent panel of this room-and-pillar mine. Those samples were tested for mechanical properties to be used in this numerical modeling study. A detailed discussion of the testing procedures and results can be found in Appendix A. The mechanical properties obtained from lab testing are shown in Table 4.1.

The lab testing as well as this numerical modeling study are part of a larger study which involves passive microseismic monitoring during pillar recovery of one of the panels. The core samples were retrieved from holes which were drilled primarily for the installation of the seismic network. Details of the microseismic study, as well as a more in-depth discussion

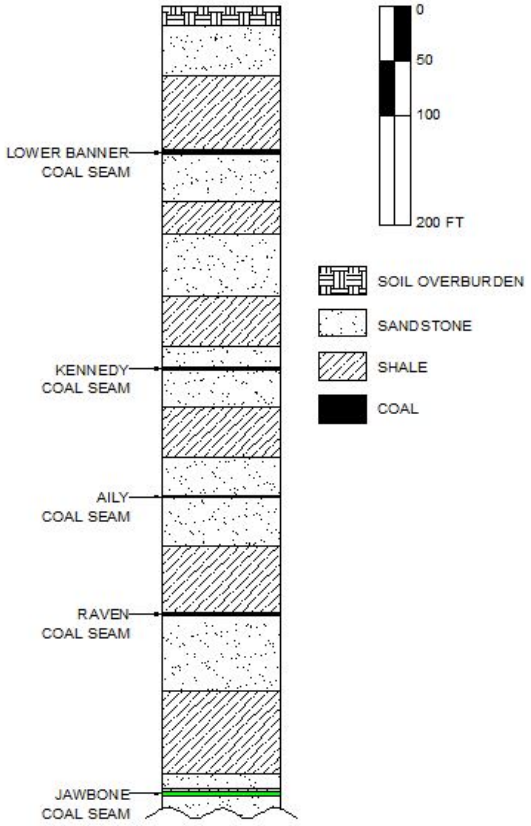

Figure 4.3: Geologic column summarizing the cores collected from Core Hole 679, which was drilled directly above Panel 2D prior to mine development. The location of the core hole relative to Panel 2D is shown in Figure 4.2.

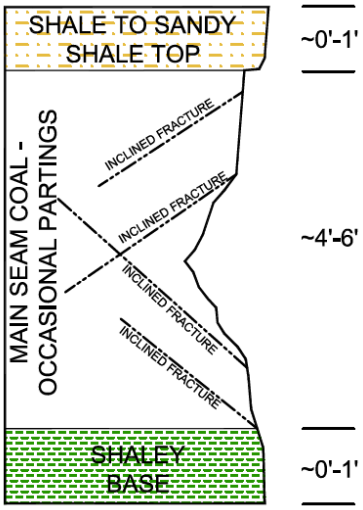

Figure 4.4: Depiction of the inclined fractures observed within the Jawbone seam in the studied panel. Also shown is the typical roof and floor material.

of this site and its geology can be found here [6].

4.5 Two-Scale Modeling

The numerical modeling which took place as part of this study was performed in two phases. The first phase was performed with fine discretization of the model, and pertained only to the pillar-scale. The primary output from this step in the modeling process is the stress-strain response of the pillars. The stress-strain response of the pillars was then used as an input in the second phase of the modeling procedure, which was focused on a larger scale. All of the numerical modeling involved in this study was performed in Itasca's FLAC3D (Fast Lagrangian Analysis of Continua in 3-Dimensions) [7].

4.5.1 Pillar-Scale Modeling

Pillar scale modeling took place in multiple phases as well. Finding appropriate material properties for the coal material was the first step. The second step was to use those coal material properties to find appropriate input values for the material properties of the roof and floor material.

To determine the material properties of the coal material, models were constructed for various coal pillar sizes. Square coal pillars were simulated between an elastic roof and floor material. The roof and floor were chosen to be elastic to minimize the effect of the interaction between the coal pillar and the roof and floor while modeling the coal material alone. An example of the geometry of the modeled coal pillar along with the elastic roof and floor material is shown in Figure 4.5.

Coal pillars with a width-to-height ratio of six and eight were simulated in FLAC3D during the first phase of the small-scale modeling. Simple, square coal pillars were modeled with an elastic roof and floor in order to find material parameters which would result in reasonable coal pillar strengths. These coal pillars were assumed to follow the Hoek-Brown criterion, which is shown in Eq. (4.1). The Hoek-Brown failure criterion is one of the built-in constitutive models available in FLAC3D. A range of values were chosen as inputs for the material properties of the simulated coal pillars. The material property values used were restricted to reasonable ranges found from the literature available on the subject [8, 9]. The results of the parametric analysis are shown in Appendix D.

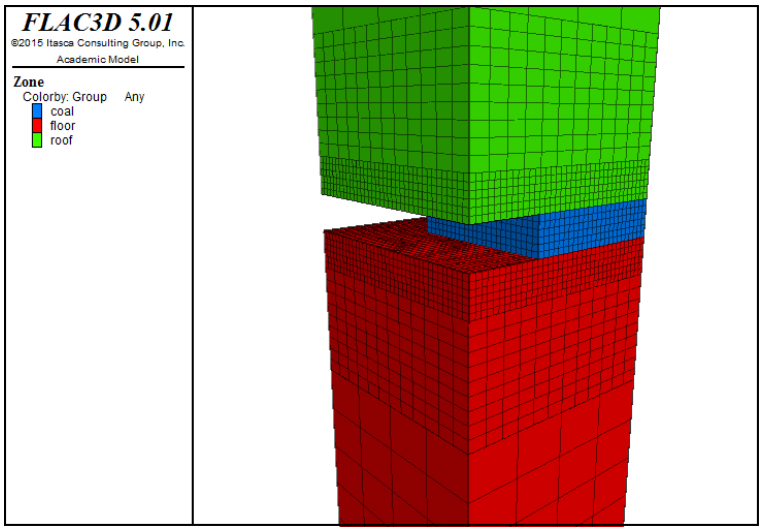

Figure 4.5: An example of a coal pillar geometry in FLAC3D. The pillar shown is one quarter of a pillar which has a width to height ratio of 8.

$$\sigma_1 = \sigma_3 + \sigma_c \left(m_b \frac{\sigma_3}{\sigma_c} \right)^a \tag{4.1}$$

The stress-strain response of the pillars was recorded during loading. Stress-strain curves for the two models which most closely match the peak strength as suggested by the empirical Bieniawski equation are shown in Figure 4.6. The square pillar with width-to-height ratio of 6 shows strain-softening behavior, while the pillar with width-to-height ratio of 8 shows perfectly plastic, approaching strain-hardening post-peak behavior, as expected from laboratory tests [10]. The material parameters used for these two models were used for subsequent pillar-scale numerical models.

During this stage of modeling, calibration was performed by attempting to match the peak strength of the modeled pillar to the empirically derived, Bieniawksi coal pillar strength equation [11]. This calibration method has been used previously [9]. The pillar strength, S_P, of a square pillar as given by the Bieniawski formula is [12]:

$$S_P = S_i \left[0.64 + 0.36 \frac{W_p}{H_p} \right] \tag{4.2}$$

where W_p is the pillar width and H_p is the pillar height.

The peak strength results from the numerical models is listed with strengths predicted

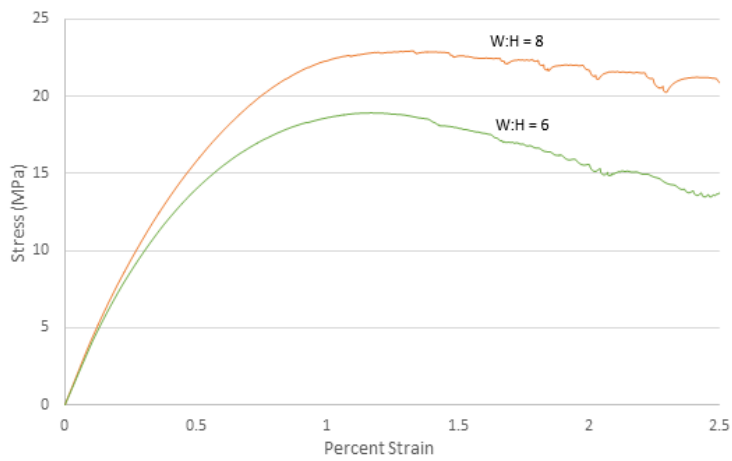

Figure 4.6: Stress-strain response of the two square pillars–of width to height ratios equal to six and eight–with elastic roof and floor.

Table 4.2: Peak strength of two numerically modeled square coal pillars and the predicted strength from the Bieniawski equation.

Width to height ratio	Pillar strength estimation method	
	Bieniawski Equation	Numerical Model
6	17.3 MPa	18.9 MPa
8	21.8 MPa	22.9 MPa

by the Bieniawski equation in Table 4.2. A difference of approximately ten percent exists between the results of the numerical models and the peak strength values predicted by the Bieniawski equation. The material property values obtained here are not the sole combination of values which would produce results within a reasonable range of the values predicted by the Bieniawski equation, but they both match empirical results and are known to be well within reasonable ranges.

The material property values obtained for the coal pillar from the numerical modeling of the square pillars were assigned to numerical models of pillars matching the dimensions of the rectangular pillars cut in Panel 2D. The value obtained was compared to the Mark-Bieniawski strength equation, Eq. (4.3) [13]. The peak strength values obtained for the rectangular pillar models were within approximately ten percent of the strength value predicted by the Mark-Bieniawski equation.

$$S_P = S_i \left[0.64 + 0.54 \frac{W_p}{H_p} - 0.18 \frac{W_p^2}{L_p H_p} \right] \tag{4.3}$$

where L_p is the length of the pillar.

The coal material properties were then modeled along with realistic roof and floor materials. The roof and floor material was modeled with the ubiquitous joint constitutive model built into FLAC3D. The ubiquitous joint model in FLAC3D implicitly considers the effect of a user-defined joint strength and orientation within a Mohr-Coulomb material. Shearing and tensile failure along the user-defined joint orientation is allowed anywhere within the material without the sacrifice in computation time associated with modeling the joints explicitly. Implementing the ubiquitous joint constitutive model is the most efficient means of including the effect of a series of joints or laminations in FLAC3D.

The properties of the immediate roof material were estimated from laboratory testing which was performed on samples from two core holes drilled during installation of a micro-seismic monitoring array. A summary of those lab test results is shown in Table 4.1. A more in-depth analysis of the immediate roof material can be found in Appendix A.

Mechanical properties determined from laboratory samples should not be assumed appropriate for numerical modeling of large-scale rock masses. Adjustments must be made to the mechanical properties to be applied to large and/or in situ rock. The uniaxial compressive strength, Young's modulus, and angle of internal friction found in the laboratory match well with strong, competent shale, published in the literature [9]. The input parameters used here were determined from [9], which gives suggested numerical modeling inputs for various rock types and strengths. Additional properties required for numerical modeling were assumed to follow those suggested by the literature. The properties used in these numerical models for the shale material, which were determined from both laboratory testing as well as the literature available, are given in Table 4.3.

As discussed in Appendix A, weaker laminations were obviously present in the core samples obtained from one of the holes drilled. The material properties listed in Table 4.3 cannot be assumed to be reasonable for the immediate roof above the entire panel. The weaker laminations present in some of the roof material were represented in the models by reducing the properties of the implicitly modeled joints by a factor of 2 from those shown in Table 4.3.

An example of a loaded pillar in FLAC3D which matches the pillar dimensions in Panel 2D and which has a roof and floor which contain the material properties listed in Table 4.3

Table 4.3: First estimates of material properties of the roof rock used in numerical models. The values listed are obtained from laboratory testing or literature available on numerical modeling input parameters [9].

Parameter	Unit	Value
Young's modulus	GPa	23.2
Compressive strength	MPa	80
Angle of internal friction	°	30
Cohesion	MPa	14.8
Tensile strength	MPa	4.6
Bedding friction angle	°	10
Bedding cohesion	MPa	2.96
Bedding tensile strength	MPa	0.46

is shown in Figure 4.7. The stress and strain values plotted are determined from average stress and strain across the area of the pillar. Only one quarter of the pillar was modeled to obtain this stress-strain curve.

Calibration of the model is necessary at this stage. An initial stage of calibration was performed when the peak strength of two sizes of modeled square coal pillars were matched to empirically determined pillar strengths. These coal strength properties also matched empirical strength equations for rectangular pillars. Calibrating models by matching them to underground observations is another common practice. Visual observations at the studied site were limited to the degree of rib sloughage, which was reported to be six inches to one foot. Rib sloughage was identified in the models by analyzing the "state" of the zones in the coal pillar.

4.5.2 Large-Scale Modeling

The stress-strain curves obtained from loading the pillar-scale models in FLAC3D was used as an input in the large-scale models. A fictitious material was used to represent the seam during excavation. The fictitious material modeled within the seam was made to follow the stress-strain response of the panel itself to being excavated. Using this fictitious material, a

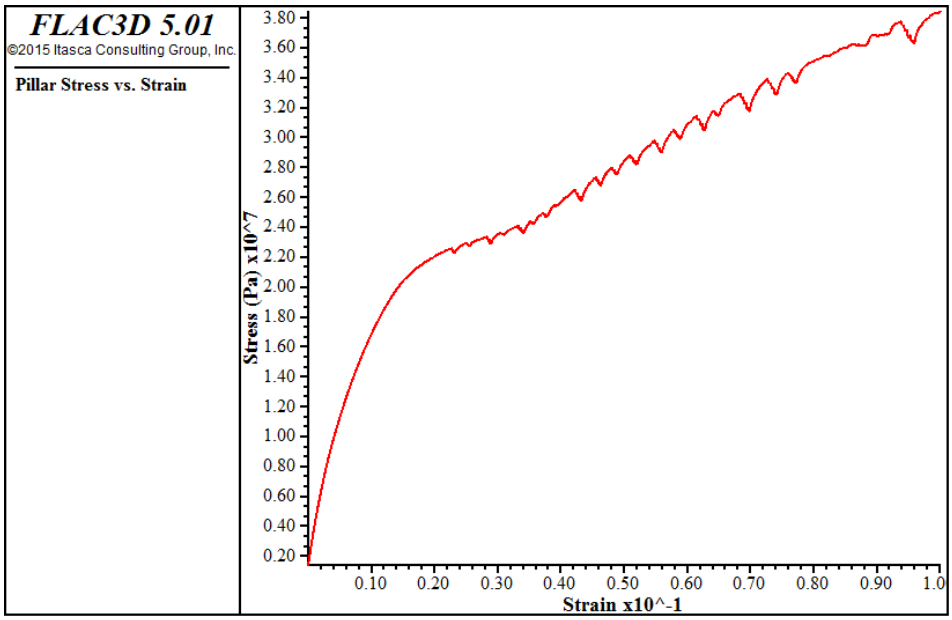

Figure 4.7: Stress-strain response of a rectangular pillar with roof and floor properties listed in Table 4.3.

much coarser, and, therefore, much more efficient large-scale model could be created.

Large models with a lateral extent sufficient to encompass the entire room-and-pillar panel were constructed. These models extended vertically from below the mined seam to the surface. Discretization of the models was far coarser than required for accurate representation of the pillar geometry explicitly. The panel-scale model geometry is shown in Figure 4.8.

The material modeled within the seam was made to follow an altered version of the stress-strain response recorded from the pillar-scale models. The stress-strain relationship of the fictitious material, $\sigma_f(\epsilon)$, is related to the stress-strain relationship of the actual coal pillars, $\sigma_p(\epsilon)$, by:

$$\sigma_f(\epsilon) = (1 - ER)\sigma_p(\epsilon) \tag{4.4}$$

where ER is the extraction ratio within the panel. The factor $(1 - ER)$ is equal to the ratio of the pillar area divided by the tributary area, so multiplying the stress applied to the pillars by a factor of $(1 - ER)$ has the effect of distributing the stress on a single pillar to the tributary area of the pillar [14]. This results in the appropriate amount of stress being applied to the coarse, fictitious material within the panel.

The adjustment made to the stress-strain relationship shown in Eq. (4.4) forces the

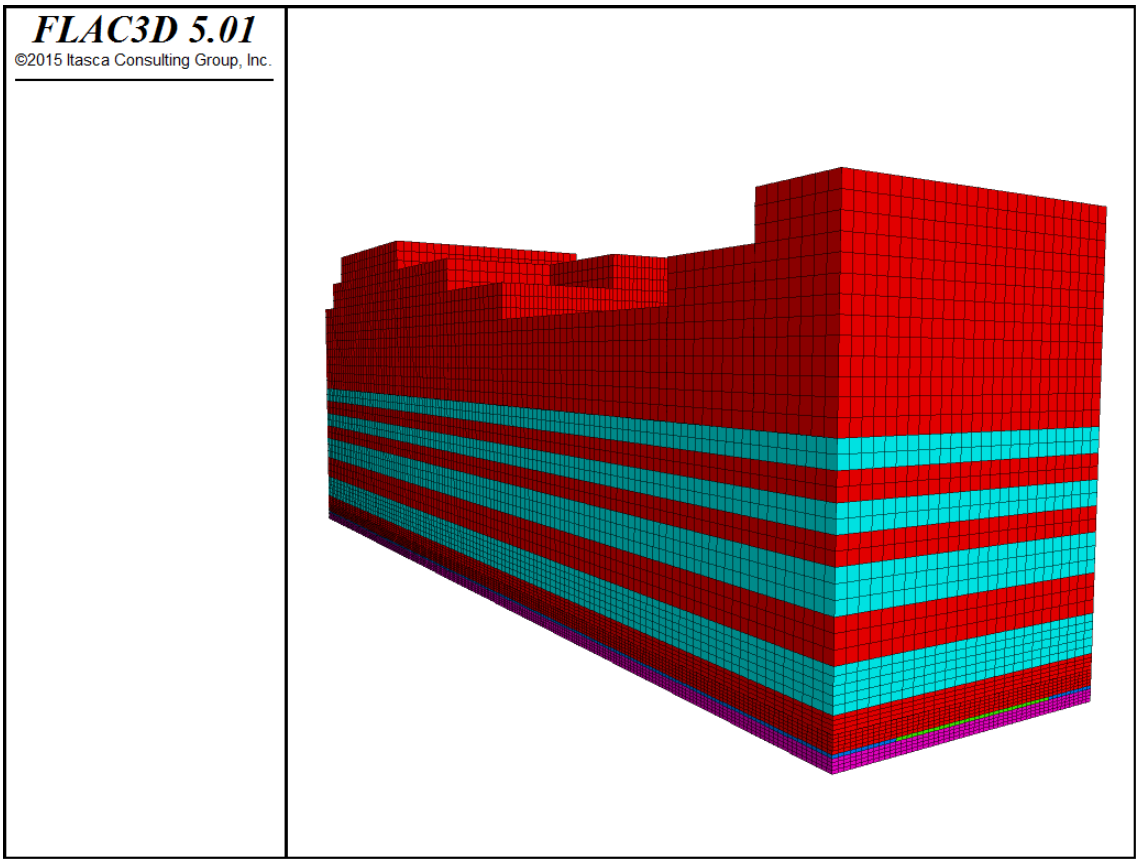

Figure 4.8: Panel scale model with representative overlying strata up to approximate surface topography.

material within the panel to behave as if pillars were explicitly modeled without modeling the actual pillar geometry. In effect, the stress applied to the pillar in the pillar-scale model is spread out to the material which fills the seam in the panel-scale model. Furthermore, when the fictitious material is loaded, it will respond as regularly spaced pillars within the seam would.

Because the coarse, fictitious material modeled within the seam follows the altered stress-strain relationship shown in Eq. (4.4), the Young's modulus assigned to the material must be altered as well. The Young's modulus of the fictitious material, E_f, becomes $(1 - ER)E_p$, where E_p is the Young's modulus found from the stress-strain curve resulting from the pillar-scale model. Also, Poisson's ratio of the material within the seam of the panel-scale model is set to zero to prevent the development of horizontal stresses within the seam from taking a vertical load.

Implementation of a new, fictitious material like one which is made to follow Eq. (4.4) requires the creation of a new constitutive relationship. FLAC3D supports implementation of user-defined constitutive models [7]. For simplicity, the constitutive model created for this study followed Tresca's failure envelope.

The Tresca failure envelope predicts failure when the maximum shear stress reaches some threshold. Because the loading of this fictitious material is forced to be uniaxial, the Tresca failure surface becomes:

$$f(\sigma_1) = \sigma_1 - 2k \tag{4.5}$$

where k is analogous to the cohesion. In effect, $2k$ is the stress at which failure should occur during any step in the solving procedure of FLAC3D. More details regarding the development of the user-defined Tresca constitutive model used in this study can be found in Appendix C.

The vertical stress within the seam, σ_v, was altered to represent development of the panel by using the following relationship:

$$\sigma_v = (1 - ER)\sigma_{v0} \tag{4.6}$$

where σ_{v0} is the in situ vertical stress. This modification to the vertical stress within the seam is done to effectively remove the support capacity provided by the coal which is excavated during development. After the in-seam vertical stress is reduced by the relationship shown in Eq. (4.6), equilibrium is lost. Because the fictitious seam material behaves as a

pillar array within the seam would, the response of the overburden to the excavation is realistic. The material within the seam is loaded as the overburden relaxes over the panel and a pressure arch forms above the panel.

4.6 Results and Discussion

An in situ stress state was applied to the model geometry shown in Figure 4.8. A vertical stress, σ_v, representing the lithostatic pressure was applied to the model. The horizontal stresses which were applied followed recommendations from the literature, which suggested that the horizontal stresses in the region of the studied mine site are approximately $1.2\sigma_v$ [15]. The initial model geometry with this stess state was allowed to reach equilibrium.

The in-seam vertical stress was reduced by the factor shown in Eq. 4.6, which creates unbalanced forces. Load from the overburden weight is applied to the material within the seam. Pressure arches form above the mined-out panel. After the model is allowed to regain equilibrium, the stability of the mined seam and the surrounding rock mass can be assessed.

The vertical stress on the zones in the panel can easily be determined from FLAC3D. This vertical load can be converted to the actual stress on the pillars by dividing the vertical stress by $(1 - ER)$. The load on the pillars in the panel is shown in Figure 4.9.

The panel shown in Figure 4.9 has the same orientation as that shown in Figure 4.2. Much of the variation in vertical stress on the pillars can be explained by the depth of cover (Figure 4.2), as should be expected. In addition to the mined-out panel, the barrier pillars on either side of the panel are included in this diagram. It can be seen that the barrier pillars took on increased load when the seam was excavated.

In addition to the stress on the pillars, stability of the mine can easily be quantified. The metric chosen for quantifying panel stability is similar to the ARMPS stability factor [13]. The ratio of the pillar strength to pillar stress is shown in Figure 4.10. The strength is assumed to follow the empirical Mark-Bieniawski strength equation, Eq. (4.3). The stress on the pillars is that calculated from the two-scale modeling approach, as shown in Figure 4.9.

The resulting safety factors are similar to those found by the ARMPS method. With this pillar geometry, ARMPS estimates the stability factor of the panel to be between 2.3 and 3.1, depending on the depth of cover. The range of stability factors determined by ARMPS is very similar to the range of safety factors determined from numerical modeling with the

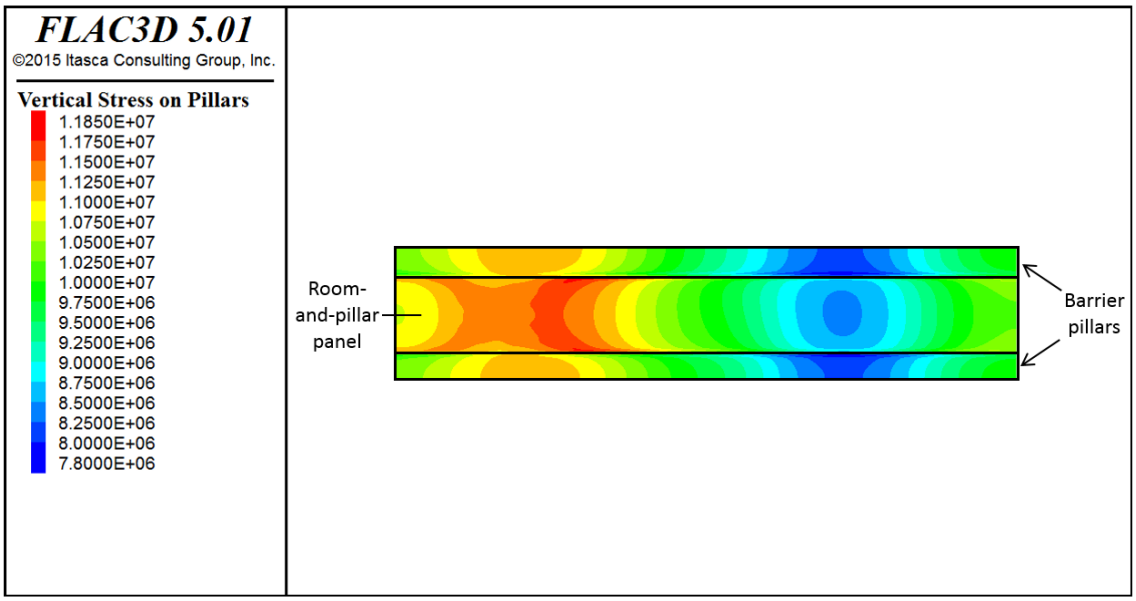

Figure 4.9: Vertical stress on the pillars in the panel. The stress values are determined by dividing the average vertical stress on the fictitious material in the large-scale model by $(1 - ER)$.

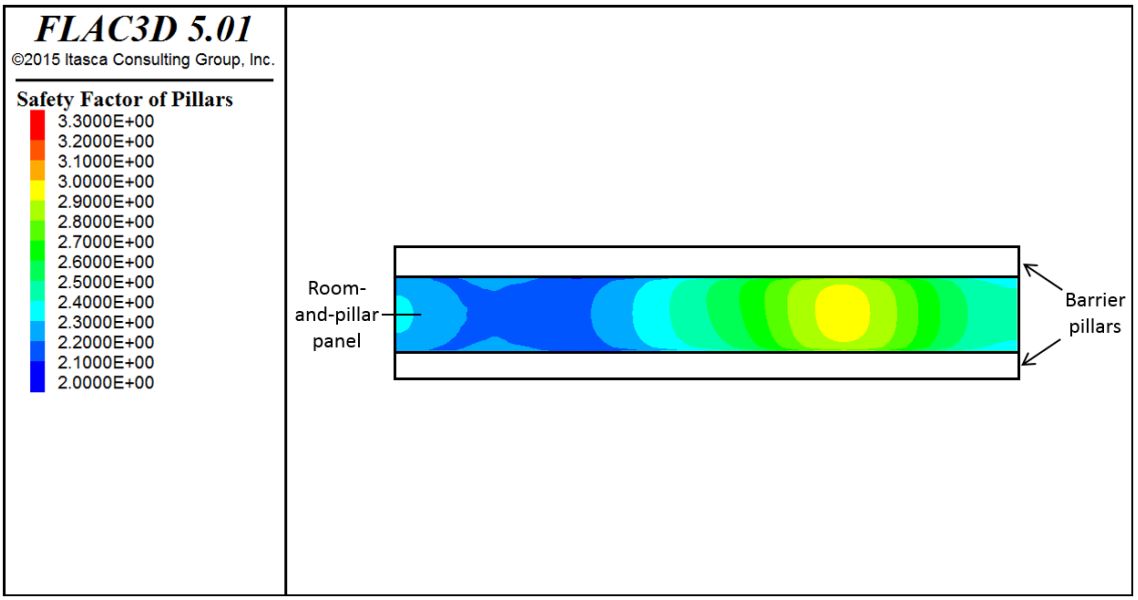

Figure 4.10: Safety factor of the pillars in Panel 2D. Strength is found from the empirical Mark-Bieniawski strength equations, and stress is determined from the two-scale modeling approach.

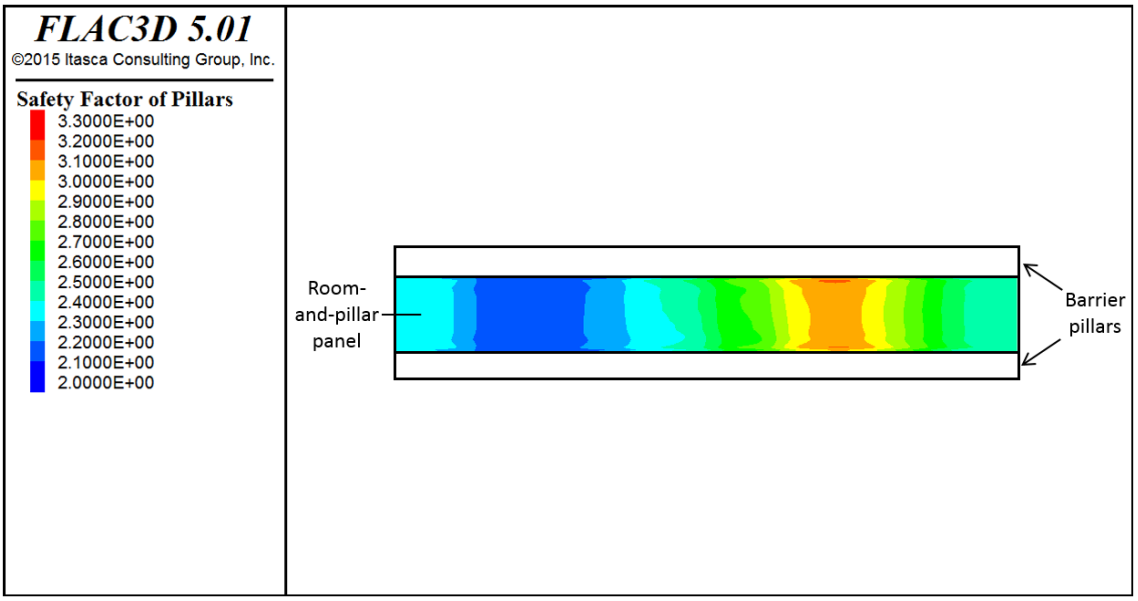

Figure 4.11: Safety factor of the pillars in Panel 2D assuming weaker laminations in the roof and floor material. Strength is found from the empirical Mark-Bieniawski strength equations, and stress is determined from the two-scale modeling approach.

roof and floor properties listed in Table 4.3. Because ARMPS has been used for nearly two decades with great success, a close match between ARMPS and the two-scale approach is a strength.

Results of the two scale approach, however, suggest that the geologic make-up of the overburden can significantly impact pillar safety factor. The same two-scale, two-stage analysis was performed with a more competent overburden. The shale strata in previous simulation were replaced with more competent sandstone to obtain the results shown in Figure 4.11.

The results displayed in Figures 4.10 and 4.11 suggest that variations within the material properties of the strata overlying a coal mine can considerably affect stability, as should be expected. Increasing the percentage of competent strata above a coal seam affected the safety factors by 10%. Inclusion of site-specific material properties adds to the reliability of these results.

4.7 Conclusions

A two-scale modeling approach has been outlined which can be applied to room-and-pillar coal mine stability. The two-scale approach is a computationally efficient means of considering pillar-scale behavior in panel-scale models. Small-scale models were created which represent unique patterns of pillar geometry within the studied coal mine panel. These pillars are loaded significantly into the plastic region while their stress-strain response is recorded. These stress-strain curves are then used in much larger scale models with a much coarser model discretization–too coarse for explicit representation of the pillars. The material within the seam of these large-scale models is made to respond as the pillars within the seam do in the small-scale models.

This two-step, two-scale modeling process easily provides a means of estimating stress on the pillars during development. The results obtained from this two-step process have been shown to match well with the results given by ARMPS. Matching ARMPS, an industry standard in design, suggests that the results are reasonable. Varying the material properties of the strata overlying the room-and-pillar panel in this two-scale, two-step process can significantly impact the resulting safety factors. And the inclusion of site-specific characteristics adds to the reliability of the results.

4.8 Acknowledgment

This work was supported by NIOSH (contract 200-2011-40313) through the Capacity Building and Ground Control Research for the Mining Industry initiative.

Works Cited

[1] US EIA. Short term energy outlook. *Energy Information Administration, Department of Energy*, 2016.

[2] US EIA. Annual coal report 2013. *US Energy Information Administration, Washington, DC*, 2013.

[3] Mine safety and health administration.

[4] C Mark, F Chase, and D Pappas. Reducing the risk of ground falls during pillar recovery. *Transactions-society for mining, metallurgy, and exploration incorporated*, 314:153–160, 2003.

[5] B Damjanac, M Pierce, and M Board. Methodology for stability analysis of large room-and-pillar panels. In *48th US Rock Mechanics/Geomechanics Symposium*. American Rock Mechanics Association, 2014.

[6] William J Conrad. Microseismic monitoring of a room and pillar retreat coal mine in southwest virginia. Master's thesis, Virginia Polytechnic Institute and State University (Virginia Tech), 2016.

[7] Itasca Consulting Group, Inc., Minnesota. *Fast Lagrangian Analysis of Continua in 3-Dimensions, version 5.0, manual*, 2013.

[8] Jienan Pan, Zhaoping Meng, Quanlin Hou, Yiwen Ju, and Yunxing Cao. Coal strength and young's modulus related to coal rank, compressional velocity and maceral composition. *Journal of Structural Geology*, 54:129–135, 2013.

[9] Essie Esterhuizen, Chris Mark, and Michael M Murphy. Numerical model calibration for simulating coal pillars, gob and overburden response. In *Proceeding of the 29th international conference on ground control in mining, Morgantown, WV*, pages 46–57, 2010.

[10] MN Das. Influence of width/height ratio on post-failure behaviour of coal. *International Journal of Mining and Geological Engineering*, 4(1):79–87, 1986.

[11] ZT Bieniawski. A method revisited: coal pillar strength formula based on field investigations. In *Proceedings of the Workshop on Coal Pillar Mechanics and Design. Pittsburgh, PA: US Department of the Interior, Bureau of Mines, IC*, volume 9315, pages 158–165, 1992.

[12] Z.T. Bieniawski. The effect of specimen size on compressive strength of coal. *International Journal of Rock Mechanics and Mining Sciences & Geomechanics Abstracts*, 5 (4):325 – 335, 1968.

[13] C. Mark and F.E. Chase. Analysis of retreat mining pillar stability (armps). In *Proceedings-New Technology for Ground Control in Retreat Mining. Pittsburgh, PA: US Department of Health and Human Services, Public Health Service, Centers for Disease Control and Prevention, National Institute for Occupational Safety and Health, DHHS (NIOSH) Publication*, pages 17–34, 1997.

[14] Essie Esterhuizen, Chris Mark, and Michael Murphy. The ground response curve, pillar loading and pillar failure in coal mines. In *29th International Conference on Ground Control in Mining*, 2010.

[15] Christopher Mark and Murali Gadde. Global trends in coal mine horizontal stress measurements. In *10th Coal Operator's Conference COAL 2010)*, 2010.

Chapter 5

Probabilistic Approach to Coal Pillar Design

5.1 Abstract

The classical approach to engineering design involves the purely deterministic calculation of the factor of safety–the ratio of strength to stress. The factor of safety is an easy calculation to perform in many circumstances, and it is very easy to interpret the results. The simplicity of the method is both a strength and a weakness. The results of the deterministic factor of safety calculation are simple to determine and interpret, but it has no ability to account for the uncertainty and variability present in the inputs.

Uncertainty is prevalent in geotechnical engineering applications. This uncertainty can stem from spatial variability, poor sampling, a dynamically changing environment, etc. Probability analyses allow input parameters to take the form of a distribution rather than a single value, making them uniquely equipped to handle the uncertainty inherent in geotechnical engineering design considerations. A stochastic approach also has the benefit of resulting in a probability of failure, which is more meaningful than a factor of safety.

Though stochastic modeling is becoming more common in many geotechnical applications, it is still not widely used for coal pillar design. The objectives of this study are to justify the concept of using a stochastic approach to coal pillar design and to compare the results of a simple stochastic analysis to those of standard industry practice.

A simple synthetic study was performed to compare the results of a probabilistic analysis of coal pillar design to the results obtained from running ARMPS, published by NIOSH.

Normal distributions were assigned to each input parameter required to determine the factor of safety of a single coal pillar. The probability of failure resulting from the synthetic study was found to be more conservative than the ARMPS stability factor.

A probabilistic approach to coal pillar design is discussed in comparison to the traditional deterministic approach. The effective handling of uncertainty and the increased meaning of the inputs and outputs inherent to a probabilistic approach are determined to be the greatest strengths of the method.

5.2 Introduction

The method of engineering design is the process of choosing the appropriate components to make a functional structure that is sufficiently safe. Engineering design typically involves an iterative, purely deterministic approach where a multitude of inputs are adjusted until the optimal design is reached. This deterministic approach to assess safety and durability generally results in a factor of safety (FS) value, as calculated by:

$$\text{Factor of Safety} = \frac{\text{STRENGTH}}{\text{STRESS}} \tag{5.1}$$

The factor of safety is a very easy calculation to perform in many circumstances, and it is very easy to interpret the results. If the strength of a component or a structure is greater than the stress expected to be applied to the component or structure, then the factor of safety will be greater than one and the component or structure is expected not to fail. However, if the stress exerted on the component or structure exceeds the strength, then the factor of safety will be less than one and the component or structure is expected to fail.

The greatest strength of deterministic factor of safety calculation is also its greatest weakness: it is extremely simple. Its ubiquity in engineering design calculations can also be attributed to a general unwillingness to change. Because of its simplicity, the deterministic approach to factor of safety calculations is completely lacking in uncertainty quantification.

For the deterministic approach to be used, it must be assumed that the exact inputs are known. If the exact inputs are known, then the exact solution can be determined. The deterministic approach is a very simple approach to engineering design. The greatest strength of deterministic factor of safety calculation is also its greatest weakness: it is extremely simple. Because of its simplicity, the deterministic approach to factor of safety calculations is completely lacking in uncertainty quantification.

Uncertainty quantification is an important practice in all engineering practices. This is especially true when regarding geotechnical engineering. A high level of uncertainty is involved with engineering geotechnical structures. A common method of skirting the issue of uncertainty quantification is to take a conservative approach to design. The conservative approach involves underestimation of the strengths and/or overestimation of the stresses in an attempt to guarantee a safe design. Using a conservative approach for engineering design does not guarantee safety, can lead to over design of components and structures, and removes meaning from the term factor of safety by introducing intentionally arbitrary inputs.

This conservative approach has led to design standards that require factors of safety for elevator. Elevators must be over designed to some degree because of the likelihood of misuse and the dire consequences of failure, but many engineering structures do not require the over design which is typically present. Intentionally designing to a factor of safety much greater than one indirectly admits the fault in the deterministic approach while bypassing more meaningful and less arbitrary alternatives.

5.3 Probabilistic Approach

A probabilistic approach to engineering design can be a superior alternative to a deterministic approach. Instead of considering one value for each input in an engineering design calculation, a probabilistic approach allows for a distribution of values for each input parameter. A distribution is used rather than a single value to represent the uncertainty or variability in the data. With a distribution of inputs, the output will also take the form of a distribution. This distribution of outputs leads to the greatest strength of the probabilistic analysis, which is a meaningful result.

Using a probabilistic approach for calculating factors of safety can easily be visualized in a few different ways. Figure 5.1 shows possible distributions of stress and strength for an example probabilistic analysis. The probability of failure in the example component or structure is the area confined in the overlap where the stress exceeds the strength. Figure 5.2 shows a second possible visualization of results from a probabilistic analysis. With the factor of safety output plotted as a single distribution, the probability of failure is simply the area under the curve to the left of a factor of safety equal to one. This is a simplified version of possible results from stochastic analyses, but a more complex analysis will likely take the same general form.

The probabilistic approach has some inherent advantages over the more widely used

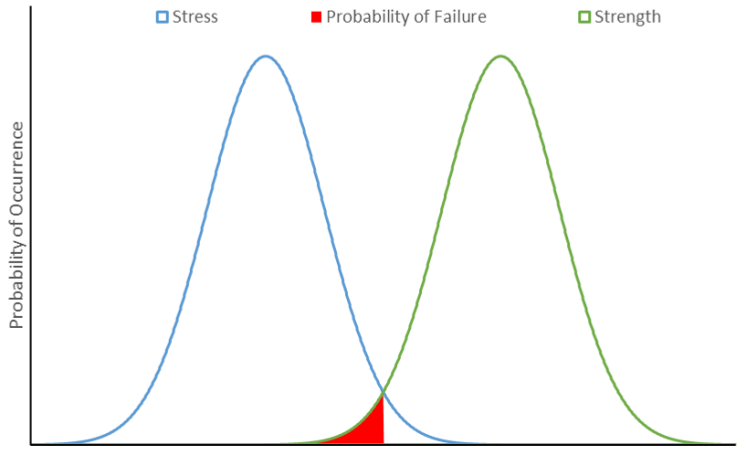

Figure 5.1: Example probability distributions of stress and strength

deterministic approach. Two of these advantages are:

- Input parameters represented by single values suggest knowledge of the exact value. Input parameters represented by distributions show uncertainty or variability in the data which makes them a more realistic representation.
- *Probability of failure* is more meaningful than *safety factor* in many instances. Designing to an acceptable probability of failure is a better engineering practice than setting an arbitrary factor of safety threshold.

These are two of the more important advantages of the probabilistic method over the deterministic method, but there are additional, less obvious advantages. There is a smaller chance of user error when a probabilistic analysis is used. This is inherent to the method, because the user is not forced to determine a single value for the input parameters. Fundamentally accounting for any uncertainty in the calculation allows the user to be more certain of inputs. Furthermore, the process can be quicker and easier to implement. After performing a deterministic design calculation, a sensitivity analysis it typically required to deal with uncertainty. A probabilistic analysis removes the need for a sensitivity analysis because the uncertainty is handled inherently.

Probabilistic analyses for engineering design have been used in many industries to determine probability of failure [1]. The natural variability of the ground makes geotechnical design a unique setting where a probabilistic approach should be used more widely. A transition toward using the probabilistic approach for engineering design of geologic structures

Figure 5.2: Example output distribution of factor of safety

is taking place for rock wedge failure [2], slope stability [3], and room-and-pillar failure in oil shale mining [4], among others.

5.4 Coal Pillar Design

Like many other structural design problems, coal pillar design can be expressed as a factor of safety. Estimating stress on a coal pillar can be relatively straightforward, but the method for determining coal pillar strength is not as well established. There are many equations for coal pillar strength, and any of them can be appropriate in a given set of conditions.

The stress supported by a pillar in a room-and-pillar mine can be assumed to be a function of the tributary area and the pillar area, shown in Figure 5.3, as well as the overburden stress. It is assumed that each pillar supports the volume of overburden in the column above the tributary area of that pillar. For square pillars with a consistent, rectangular pattern, the equation for pillar stress, σ_p, becomes:

$$\sigma_p = \sigma_z \left(\frac{W_P + W_E}{W_E} \right)^2 \tag{5.2}$$

$$\sigma_z = \gamma z \tag{5.3}$$

Where σ_z, the the vertical stress, is the product of γ, the unit weight of the overburden,

and z, the overburden thickness. As shown in Figure 5.3, W_P is the pillar width and W_E is the width of the opening.

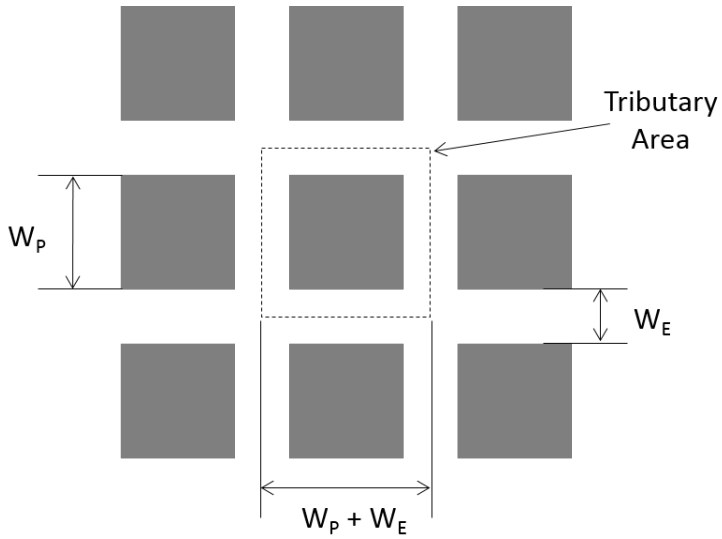

Figure 5.3: Tributary area in a room-and-pillar mine

Determination of coal pillar strength is much less straightforward. Pillar strength is commonly calculated using the Bieniawski equation [5]:

$$S_P = S_i \left[0.64 + 0.36 \frac{W}{H} \right] \tag{5.4}$$

Where S_i is the compressive strength of coal, and $\frac{W}{H}$ is the coal pillar width to height ratio. Like most equations for coal pillar strength, the Bieniawki equation is empirical. This equation was chosen because its ubiquitous use for calculating the stress of square coal pillars.

The ARMPS, Analysis of Retreat Mining Pillar Stability, program created by NIOSH, the National Institute of Occupational Safety and Health, is often used in addition to or instead of a factor of safety calculation. A "stability factor" is reported by the ARMPS program. It is recommended to design with a stability factor of at least 1.5 when the depth of cover is greater than 1000-ft [6].

5.5 Probabilistic Coal Pillar Study

Two mine geometries were assumed to test the probabilistic procedure involved with underground coal pillar design. Both geometries were 6-entry panels with 20-ft entries. One scenario had 40' x 40' pillars, the other had 60' x 60' pillars. The results for these designs were calculated for multiple depths.

A mean value was assigned to each required input parameter and a reasonable standard deviation for each value was estimated. Each input parameter was assumed to be normally distributed. Except for the pillar dimensions and the depth of cover, the distribution of all parameters remained the same for both scenarios.

The compressive strength of coal is notoriously difficult to test in a laboratory. Coal samples degrade quickly once removed from confinement, and coal exhibits a rather extreme size effect. The in situ strength of coal is generally accepted to be 900 psi, but this value has been known to vary. In situ coal strength has been determined to fall between 780 and 1070 psi [7]. Therefore, the mean value for in situ coal strength was assumed to be 900 psi with a standard deviation of 72.5 psi. This range results in the typical range of in situ coal strength reported by Mark and Barton to be approximately ± 2 standard deviations.

The room-and-pillar layout was assumed to consist of 40-ft square pillars on 60-ft centers for the first scenario and 60-ft square pillars on 80-ft centers for the second scenario. Both of these geometries result in an entry and crosscut width of 20-ft. The pillar width was given these mean values with a standard deviation of 0.5-ft. The entry width was assumed to be the center-to-center spacing minus the pillar width to keep the mine geometry consistent. The mining height was given an arbitrary mean of 6-ft and standard deviation of 0.25-ft.

All of the input parameters required for this simple study are listed in Table 5.1. The only parameter changed between the first and second runs is the pillar size. Depth was varied to compare the probabilities of failure from the probabilistic study to the stability factors from ARMPS. The stability factors were calculated for the mine geometries under development loading only.

Monte Carlo simulations were performed for each of the two runs to determine distributions for the likely factors of safety resulting from these synthetic data sets with the stress and strength equations discussed above. Random numbers were generated by [8] for each of the input parameters, with the exception of entry width which is a function of pillar width, and the factor of safety was determined. Each Monte Carlo simulation consisted of one million iterations for each of the two runs.

Table 5.1: List of statistical parameters for each input value. All distributions were assumed to be normal.

Parameter	Mean	St. Dev.
Depth	Varied	20 ft
Overburden Unit Weight	165 pcf	6 pcf
Entry Width	20 ft	0.5 ft
Pillar Height	6 ft	0.25 ft
Strength	900 psi	72.5 psi
Pillar Width		
Run 1	40 ft	0.5 ft
Run 2	60 ft	0.5 ft

5.6 Results

The results from the Monte Carlo simulations were compared to the stability factors calculated by ARMPS, and the deterministic safety factor for a variety of depths. The deterministic factor of safety results were found by inputting only the distribution means into the stress and strength equations. For the first scenario, the depth of cover was varied from 400 to 1400-ft. The depth of cover was varied from 400 to 2400-ft for the second scenario.

There is relatively good agreement between all three pillar design methods, as shown in Figure 5.4. That is, at the depth at which the ARMPS stability factor crosses the suggested design threshold of 1.5, the deterministic safety factor crosses the suggested design threshold of 1, and the probabilistic approach passes 50% chance of failure. The minimum stability factor recommended for a "satisfactory" pillar system is 1.5 for depths of cover greater than 1000-ft [7]. The depth of cover corresponding to a stability factor of 1.5 is approximately 1100-ft. At this same depth, the safety factor resulting from the deterministic method is approximately one.

The probability of failure at 1100-ft is approximately 0.6, which means 60% of pillars subjected to this loading scheme are expected to fail. This probability of failure is more conservative than the other results. The distribution of safety factors is normally distributed and centered close to one as shown in Figure 5.5. The largest safety factor calculated was approximately 1.6 and the smallest value was approximately 0.6. This range is due to the standard deviations assigned to the input parameters.

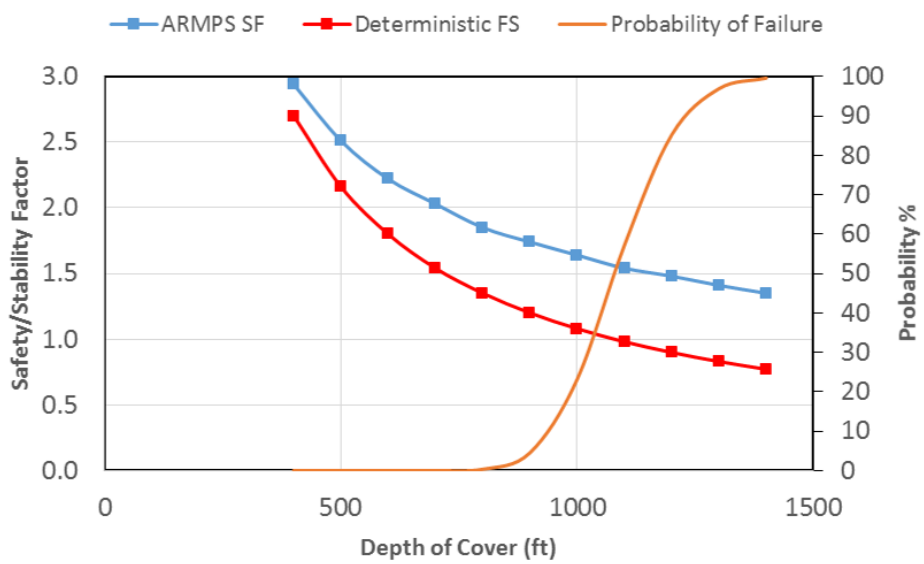

Figure 5.4: ARMPS stability factor, deterministic factor of safety, and the probability of failure for the first scenario (40 ft x 40 ft pillars) plotted versus depth of cover.

The second Monte Carlo analysis was performed assuming 60' x 60' pillars. The depths for this geometry were varied from 400-2400-ft. The resulting ARMPS stability factors, deterministic safety factors, and probabilities of failure are plotted versus depth in Figure 5.6.

The synthetic study resulted in more conservative values than ARMPS for the second scenario. The ARMPS stability factor approaches 1.5 for a depth of 2400-ft. At 2400-ft deep, the deterministic safety factor is approximately 0.8 and the probability of failure is 0.992.

5.7 Discussion

The results from the synthetic study and the results from the ARMPS varied somewhat. The difference between the results of the two methods increases with increasing depth of cover. This is most likely because the tributary area method of pillar stress determination was used for the synthetic study. The tributary area method leads to the most conservative (highest) estimate of the stress on a pillar. The tributary area has been shown to overestimate the stress on a pillar by as much as 40% [9].

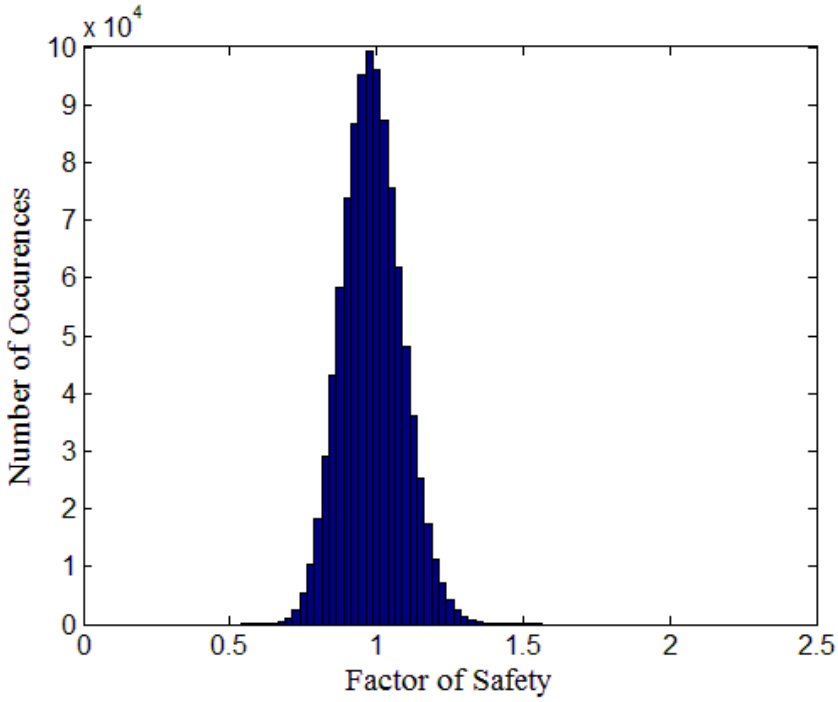

Figure 5.5: Factor of safety histogram for the second mine geometry (40 ft x 40 ft pillars) at a depth of 1100 ft.

Before the probabilistic approach to coal pillar design could become widely applied, standards would need to be created. Geotechnical engineering involves too much variation to ever adhere to the six sigma standard. An acceptable probability of failure threshold would have to be decided upon.

For example, if a probability of failure of 30% were deemed an appropriate design threshold, then this would correspond to a stability factor of approximately 1.6 for the first scenario and 1.8 for the second scenario. The probability of failure approach is a more meaningful standard by which industry-wide design thresholds could be set.

The scope of the probabilistic approach could be increased by performing a similar calculation for an entire panel rather than just one pillar. This could be done with a Gaussian field representing the distribution of coal strengths, etc. spatially. While the Monte Carlo for the simple, single-pillar example has a rather quick computation time, a panel-sized probabilistic method could take a significant amount of time to perform.

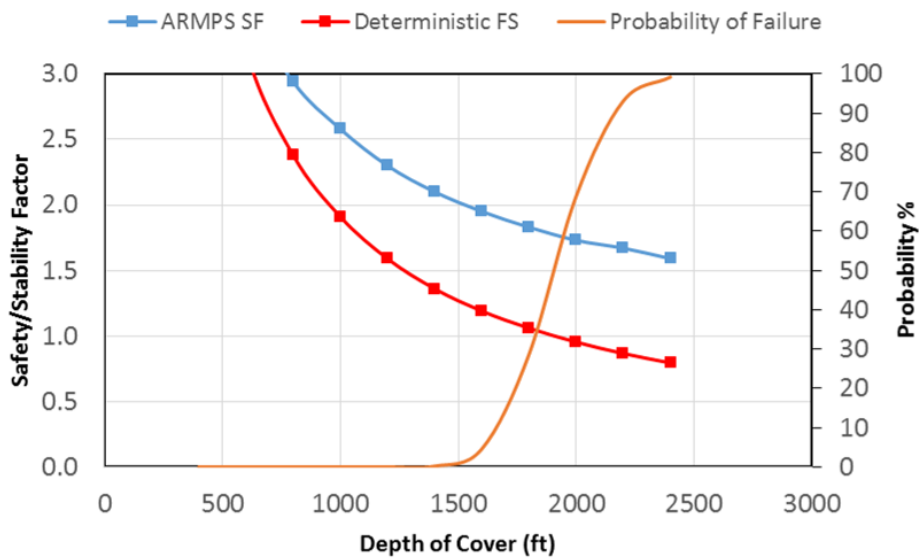

Figure 5.6: ARMPS stability factor, deterministic factor of safety, and the probability of failure for the first scenario (60 ft x 60 ft pillars) plotted versus depth of cover.

5.8 Conclusions

Uncertainty quantification is necessary in all engineering practices. This is especially true when regarding geotechnical engineering. Probabilistic analyses for engineering design are becoming more prevalent in many fields where a high degree of uncertainty is present, but remain mostly absent in coal pillar design.

Performing a probabilistic study rather than a deterministic one is a relatively easy way to quantify the uncertainty in an engineering design. A sensitivity analysis requires actively varying the inputs a slight degree to determine how the output is affected. This process can be much more time consuming, more user intensive, and less comprehensive than a probabilistic analysis like the one performed here.

A probabilistic approach to coal pillar design has potential to be a viable alternative to traditional deterministic methods. Accounting for variability or uncertainty in the inputs and outputs of engineering design calculations provides more meaningful results. Designing to arbitrary deterministic thresholds indirectly admits the fault in the deterministic approach.

The simple synthetic study performed involved comparing the results of a simple factor of safety determination to the stability factor calculated by ARMPS. Both the probability

of failure and a deterministic factor of safety were determined using the Bieniawski equation for coal pillar strength and the tributary area assumption for coal pillar stress.

For 40-ft square pillars in a 6-entry panel under development loading, ARMPS resulted in a stability factor of 1.5 at approximately 1100-ft of cover. This same scenario in the synthetic study resulted in a probability of failure of approximately 60%. The results of the synthetic study agreed somewhat with the output from ARMPS, but were more conservative than ARMPS. The conservative nature of the synthetic study was found to increase with depth.

5.9 Acknowledgment

This work was supported by NIOSH (contract 200-2011-40313) through the Capacity Building and Ground Control Research for the Mining Industry initiative.

Works Cited

[1] J Townsend, C Meyers, R Ortega, J Peck, M Reinfurth, and B Weinstock. *Review of the probabilistic failure analysis methodology and other probabilistic approaches for application in aerospace structural design*, volume 3434. National Aeronautics and Space Administration, Office of Management, Scientific and Technical Information Program, 1993.

[2] H. Park and TR West. Development of a probabilistic approach for rock wedge failure. *Engineering Geology*, 59(3):233–251, 2001.

[3] G. Zhou, T. Esaki, Y. Mitani, M. Xie, and J. Mori. Spatial probabilistic modeling of slope failure using an integrated gis monte carlo simulation approach. *Engineering Geology*, 68(3):373–386, 2003.

[4] Enno Reinsalu. Stochastic approach to room-and-pillar failure in oil shale mining. In *Proceedings of the Estonian Academy of Sciences, Engineering*, volume 6, pages 207–216. Estonian Academy Publishers, 2000.

[5] ZT Bieniawski. A method revisited: coal pillar strength formula based on field investigations. In *Proceedings of the Workshop on Coal Pillar Mechanics and Design. Pittsburgh, PA: US Department of the Interior, Bureau of Mines, IC*, volume 9315, pages 158–165, 1992.

[6] C. Mark and F.E. Chase. Analysis of retreat mining pillar stability (armps). In *Proceedings-New Technology for Ground Control in Retreat Mining. Pittsburgh, PA: US Department of Health and Human Services, Public Health Service, Centers for Disease Control and Prevention, National Institute for Occupational Safety and Health, DHHS (NIOSH) Publication*, pages 17–34, 1997.

[7] Christopher Mark and Timothy M Barton. Pillar design and coal strength. In *Proceedings-New Technology for Ground Control in Retreat Mining. Pittsburgh, PA: US Department of Health and Human Services, Public Health Service, Centers for Disease Control and Prevention, National Institute for Occupational Safety and Health, DHHS (NIOSH) Publication*, pages 49–59, 1997.

[8] MATLAB. *version 8.0.0.783 (R2012b)*. The MathWorks Inc., Natick, Massachusetts, 2012.

[9] ZT Bieniawski. Ground control. *SME Mining Engineering Handbook. Littleton, CO: Society for Mining, Metallurgy, and Exploration, Inc*, pages 897–937, 1992.

Chapter 6

Discussion and Conclusions

6.1 Overview of Study

A two-step, two-scale numerical modeling approach is outlined which can be used as a tool for analyzing the stability of underground coal mine openings. This two-scale approach starts with pillar modeling. Pillars are modeled with sufficient roof and floor material and loaded to estimate their stress-strain response. These pillar stress-strain curves are then used as inputs into large, panel-scale models. This two-step approach to numerical modeling allows for the study of the interaction between small-scale behavior and large-scale behavior in a computationally efficient manner.

The ground response curve (GRC) is a useful tool for analyzing the stability of underground excavations. The GRC originated in the tunneling industry as an analytical result from the convergence-confinement method. While the geometries used in underground coal mining are too complex for analytical solutions like this to be developed, this two-scale modeling procedure can be used to determine the GRC.

The stress state of pillars in underground coal mine workings is rarely known to great accuracy. The two-scale approach was implemented with the use of a fictitious material within the coal seam which was made to respond as the pillars would. The representative material is used instead of explicitly modeling the pillars so that a far coarser discretization could be used to speed up processing time.

With better estimates of pillar stress and strength, a probabilistic approach could be implemented for room-and-pillar coal mine design. This approach has seen widespread use in other industries because of its utility and ability to handle uncertainty. The process for

implementing a probabilistic approach to coal mine pillar design is outlined here.

Laboratory testing of samples collected from drilling in the roof was also performed. This testing was performed to find first estimates of material properties of the roof material above a room-and-pillar coal mine panel in the Eastern US. Destructive testing included uniaxial compressive strength testing, Brazil testing, and point-load testing.

6.2 Summary of Results

Laboratory testing was performed on cores collected from two holes drilled into the roof from the mine workings. The laboratory testing shows that the immediate roof material of this room-and-pillar coal mine is a strong sandy shale. While the uniaxial compressive strength seems reasonably similar between the two holes drilled, there are obvious differences in the strength of laminations present. Preparation of samples from one of the holes was difficult to perform without damaging the samples. Furthermore, the Brazil testing was mostly fruitless for samples from that hole because of the weak laminations.

The ground response curve of a room-and-pillar coal mine panel was found by gradual reduction of the internal pressure within the seam. The pressure against the roof and the convergence of the seam were recorded throughout the process of reducing the internal pressure. This process of determining the GRC is akin to the original formulation of the convergence-confinement method. The GRCs obtained are indicative of the panel stability and the self-supporting capacity of the overburden strata. The modeling results of the GRC were plotted with the stress-strain response of the pillars in order to assess panel stability.

By using a fictitious material which represents the average response of the pillars within a room-and-pillar mine panel, the full panel scale was assessed. The load placed on the pillars during panel development was estimated. Furthermore, by assuming pillar strength to be given by the empirical Mark-Bieniawski pillar strength formula, a pillar safety factor was determined throughout the mined seam.

6.3 Discussion of Results

There were three primary goals set prior to the laboratory analysis:

- Determining acoustic properties of the roof rock.

- Estimating additional material properties of the roof rock for numerical modeling.
- Concluding whether there is significant variation in the roof rock between the holes.

The acoustic properties were found nondestructively by testing specimens prepared for uniaxial compressive strength testing. Additional material properties were determined, mostly from destructive testing and from the literature. While strength variations between the two holes were found qualitatively, limited statistical analysis could support the claim with the small sample sizes available.

The ground response curve was estimated for a room-and-pillar panel in FLAC3D with a method analogous to the convergence-confinement method. The GRC predicts full convergence of the seam at full extraction, as should be expected. The interaction of the ground response curve and modeled pillar stress-strain curves can be used as a tool to size pillars.

The stress on the pillars in a room-and-pillar panel was estimated using a two-scale modeling approach. From the stress calculated, a pillar safety factor was also found. These safety factors agreed well with ARMPS stability factors for the panel. The agreement between this novel method of pillar stress determination and an industry standard is encouraging. Furthermore, the numerical models contain material properties for the studied site, which increases their reliability.

6.4 Conclusions

Safe design of underground excavations requires an understanding of the response of the rock mass to the future excavation. In the tunneling industry, the geometry is often sufficiently simple for this understanding to be reached with analytical solutions. Mining geometries, however, are far too complex for analytical solutions to be feasible.

The pillar-scale response has a great impact on the panel-scale response, and vice versa. The interaction between these two length scales is explored here using numerical modeling in FLAC3D. Rather than analyzing the interaction between these two length scales in a single simulation, a more computationally efficient approach is outlined.

A two-stage, two-scale numerical modeling approach for assessing room-and-pillar coal mine stability was introduced. The modeling approach shown here uses a coarse discretization in large, panel-scale models which includes fictitious, yet representative material within the coal seam. This representative material is made to follow the stress-strain response

of small, pillar-scale models via the implementation of a user-defined constitutive model developed for this study.

Site-specific design considerations can significantly improve reliability of results, confidence in designs, and tons of coal recovered. One-size-fits-all approaches to underground coal mine design must be either unsafe for some designs, or wasteful for others. Pillar-sizing, which is likely the most evident cost-benefit compromise in underground mining, should be done with site-specific considerations.

6.5 Future Work

This two-scale modeling approach has great growth potential for room-and-pillar coal mines. These large-scale models can be used to assess stress on pillars, convergence of openings, subsidence, etc. Conversely, monitoring any of these rock mass responses could help improve the model inputs.

With the addition of appropriate gob modeling, retreat and gob-side loading can be studied. Also, more reasonable estimates for subsidence could be found. Finally, associating the large-scale model with recorded microseismicity would be a challenge worth pursuing. By matching seismicity rate and possibly location with failed states of the model zones, panel stability assessments would be greatly improved, as would the results of the seismic survey.

6.6 Acknowledgment

This work was supported by NIOSH (contract 200-2011-40313) through the Capacity Building and Ground Control Research for the Mining Industry initiative.

Appendices

Appendix A

Properties of Roof Rocks in the Central Appalachian Region

A.1 Abstract

Laboratory tests were performed on sandy shale core specimens collected from roof rock above a retreating room-and-pillar coal mine in the Eastern US. These tests were performed in an attempt to determine: the acoustic properties to aid in a seismic survey; estimates of other material properties to be used in numerical modeling; and the degree to which the roof rock varied across the panel. Acoustic tests, UCS tests, Brazilian tests, and point-load tests were all performed on the core specimens, which totaled only about 11 feet in length. P- and s-wave velocities were estimated at 3990 $^{m}/_{s}$ and 2510 $^{m}/_{s}$, respectively. The average Young's modulus was found to be 23.2 GPa. The uniaxial compressive strength and indirect estimate of tensile strength were found to be 142 MPa and 7.84 MPa, respectively.

A.2 Introduction

Underground coal mine ground control presents a unique set of design challenges. The complexity of ground control for coal mines is due in large part to the highly variable, often laminated rock present above and below coal seams. Laboratory testing of rock specimens is one of the most informative methods for quantifying rock properties.

A series of lab tests was performed on core collected from the roof rock above a retreating

room-and-pillar coal mine in the Eastern US. The drilling was performed in order to install triaxial geophones as part of a passive seismic study of the retreat process. More details regarding the microseismic survey and a more extensive overview of the geology at this site can be found here [1].

Approximately eleven feet of sandy shale core was collected from two boreholes for the testing. The amount of core available for laboratory testing was limited. Considering the short supply of core available for testing, three modest goals were defined:

- Estimate p- and s-wave velocities to improve the results of the seismic survey.
- Develop reasonable first approximations of material properties for use in numerical models.
- Determine whether the samples obtained from Holes #1 and #2 are similar enough to be considered one sample or if they should be considered distinct.

Uniaxial compressive strength and indirect tensile strength testing was performed using an MTS load cell. The point-load test–a method of indirectly determining the unconfined compressive strength of a material–was also performed. Because the point-load test requires little to no sample preparation, it provides a quick and easy means of estimating UCS. Its ease of use and portability have led to its wide use for mining and civil engineering sites [2].

A.3 Sample Description

Two holes were drilled into the roof rock immediately above a retreating room-and-pillar coal mine located in the Central Appalachian coal fields of the Eastern US from inside the mine opening. The locations of the holes relative to the immediate mine panel are shown in Figure A.1. Approximately 120 inches were drilled for Hole #1, but a total of only 79 inches of core was collected. Hole #2 was drilled only about 58 inches into the roof, and all of the core from Hole #2 was collected. The drilling was performed for the purpose of installing two triaxial geophones as part of a seismic survey, not for the express purpose of laboratory testing for material properties. The holes were drilled vertically into the roof with a 2.5 inch diameter bit.

Pictures of the core samples taken from Holes #1 and #2 can be found in Figures A.2 and A.3, respectively. Upon initial inspection, the two holes appeared to made up of a

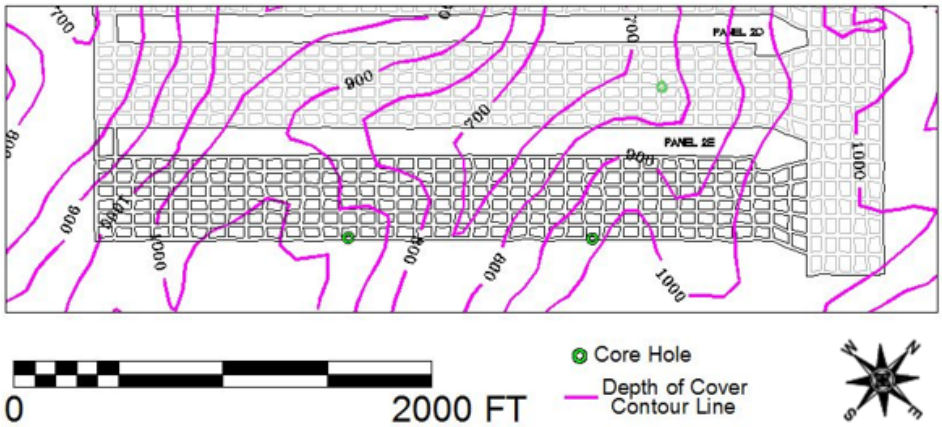

Figure A.1: Contour map showing depth of cover over room-and-pillar panel 2E. The marked drillhole locations represent the locations of the two holes drilled into the roof for installation of the seismic array from which core samples were collected and tested for rock mechanics properties.

similar rock type. Core samples from both holes are light gray in color with some laminations. Samples from both holes are sandy shale, with the sand content of Hole #1 appearing to be greater than the sand content of Hole #2. The sand present in the core from Hole #1 is fairly uniformly distributed along the core, while the sand in the core from Hole #2 is clearly layered between shale. The laminations and sand present in Hole #2 vary greatly along the core, while Hole #1 seems to be much more consistent.

Of the total collected core length of 79 inches from Hole #1, the total length of core measuring longer than four inches is 37 inches. More than the 79 inches of the ten feet of core was reported to be recoverable, but was left underground because material testing was initially an afterthought and drilling was done primarily for installation of the seismic network. This ratio of recovered core longer than four inches to the total amount of collected core results in a rock quality designation (RQD) of 47%. Similarly, 15 inches of core from Hole #2 was comprised of sections of core greater than four inches in length, resulting in an RQD of 26%. These results are summarized in Table A.1. The values of RQD obtained for Holes #1 and #2 correspond to the upper and lower limits of the "poor rock" qualitative description, respectively, as defined by [3].

After this initial inspection, laboratory tests were performed in an attempt to accomplish the goals listed above until no unbroken samples were left. Destructive tests performed include uniaxial compression test, the indirect uniaxial tensile strength, so-called "Brazil-

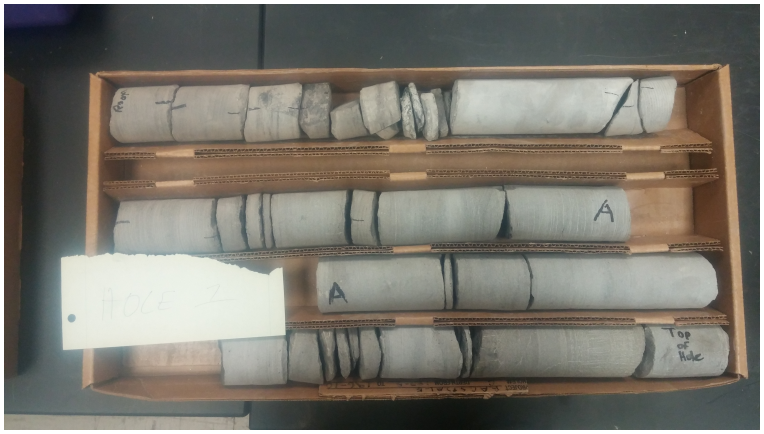

Figure A.2: Cores collected from Hole #1. Total length of core collected (all shown) is about 79 inches of the total ten feet drilled.

Figure A.3: Cores collected from Hole #2. The drilled length of Hole #2 is 58 inches, and everything recoverable was collected (all shown).

Table A.1: Rock Quality Designation (RQD) for the portion of core collected from Hole #1 and the entirety of length drilled for Hole #2.

Hole #	RQD	Qualitative Description
1	47	Poor rock
2	26	Poor rock

ian," test, and the point-load test. The wave propagation speeds and the density of the rock were also determined in a non-destructive manner.

A.4 Sample Preparation

Priority was given to uniaxial compressive strength (UCS) testing because longer specimens are required for it and multiple properties may be estimated from testing a single specimen. Specimens were prepared for the Brazilian test second. For the Brazilian test, ten specimens were prepared to meet the International Society of Rock Mechanics (ISRM) suggested minimum of ten specimens per sample [4]. Ten specimens for the Brazilian test were prepared for each of the two holes drilled.

A.4.1 Uniaxial Compressive Strength (UCS) Test

The ISRM suggests UCS tests should be performed on cores with a length to diameter ratio between 2.5:1 and 3:1 [5]. None of the recovered cores met this length requirement. The minimum required length-to-diameter ratio which allows a shear failure plane to develop in most specimens as predicted by the Mohr-Coulomb model is approximately 2:1. This absolute minimum requirement left four specimens long enough for uniaxial compression testing, three specimens from Hole #1 and one specimen from Hole #2.

The four specimens long enough for UCS testing were cut to the maximum possible length. After cutting, precision grinding was performed on the ends of the specimens to obtain the greatest possible end-to-end flatness and the least possible deviation from perpendicularity between ends and the center axis of the core. The ISRM suggests specimens should be flat to within 0.02 mm (8 x 10^{-4} in.), should not depart from perpendicularity by more than 0.05 mm (2 x 10^{-3} in.) in 50 mm (2 in.), and have smooth sides to within 0.3 mm (1 x 10^{-2} in.) [5].

The dimensions of the specimens which would be subjected to UCS testing are listed in Table A.2. ISRM suggests taking six diameter measurements–two diameter measurements at right angles of each other at each the top, center, and bottom–of each sample and computing the average. Furthermore, it is suggested by the ISRM that at least two length measurements be taken and averaged [5]. The averages of these measurements are listed in Table A.2. A list of all of the individual measurements can be found in Appendix B.

Due to poor drilling and/or sample friability, the samples showed irregularities signifi-

Table A.2: Dimensions of the four specimens subjected to uniaxial compression strength (UCS) testing after preparation.

Hole	Sample	Diameter (in.)	Length (in.)	End Flatness (in.)
1	1	2.237	5.607	0.025
1	2	2.238	4.425	0.010
1	3	2.253	5.352	0.018
2	4	2.246	5.464	0.020

cant enough to prevent the ISRM suggested tolerances from being met. The suggested level of side smoothness was not present in any of the samples. This was likely due to the presence of laminations throughout the cores. Furthermore, the suggested end flatness was not attained because of curvature present in the long axis of the samples.

A.4.2 Brazilian Test

The ISRM is less stringent regarding sample preparation for the Brazilian test than for UCS testing. They recommend a specimen thickness approximately equal to the radius. They also suggest that the specimen be free of any tool marks or irregularities [4].

For each of the two holes drilled, ten specimens were prepared for the Brazilian test. Ten is the ISRM suggested minimum number of specimens for one sample. All twenty samples prepared for the Brazilian test were cut to have a thickness-to-diameter ratio of approximately 0.5:1. After being cut, the samples were precision ground so that the ends were smooth. Of all twenty samples prepared, the maximum and minimum thickness-to-diameter ratios were 0.548:1 and 0.484:1, respectively. The dimensions of the specimens after preparation can be found in Appendix B [4].

Some difficulty was encountered during preparation of the samples from Hole #2 for the Brazilian test. Three specimens had to be discarded during the grinding process because they split along the foliations present. While this readiness to split along foliations is not reflected numerically, it is indicative of a significant source of weakness present in the roof rock where Hole #2 was drilled. Sample preparation of all ten specimens from Hole #1 was completed without issue.

Table A.3: P- and S-wave velocity estimates of the four samples prepared for UCS testing. Velocities listed are given in ft/sec (m/s).

Hole	Sample	S-Wave	P-Wave
1	1	7620 (2320)	12400 (3790)
1	2	7430 (2260)	12000 (3650)
1	3	7610 (2320)	12300 (3730)
2	4	7920 (2410)	12000 (3650)

A.5 Non-Destructive Testing

One of the primary goals of this laboratory testing was the determination of the acoustic properties of the roof rock to aid in later seismic analysis. To that end, the speeds of the p- and s-waves through the cores was estimated. Acoustic testing was performed on the four samples which were prepared for UCS testing.

To perform the acoustic tests, a Model - 5217A Sonic Viewer was used to generate and detect a waveform using a piezoelectric transducer and a piezoelectric receiver, respectively. A pneumatic clamp was also used to hold each sample in place to reduce the measurement error.

To measure the s-wave velocity, the piezoelectric transducer was placed in contact with the piezoelectric receiver. The input and output amplitudes and frequencies were adjusted until a waveform was discernible. The arrival time in μs was recorded for each of the first two peaks and troughs of the waveform. Each sample was then placed between the piezoelectric transducer and receiver and the process was repeated. The difference in the arrival times between corresponding peaks and troughs was then averaged to get an estimate of the s-wave travel time through each sample. Table A.3 shows the s-wave velocities estimated for the four samples tested.

The procedure for estimating the p-wave velocity is somewhat simpler. The sample was placed between a compression-type piezoelectric transducer and receiver and the first arrival

was recorded. The ratio of the sample length to this travel time is then taken as the p-wave velocity. The p-wave velocity estimates for each of the four samples tested can be found in Table A.3. All raw data collected to determine the acoustic properties listed in Table A.3 can be found in Appendix B.

The only other material property determined non-destructively was density. Each of the twenty-four specimens which were cut and ground–four for UCS testing, ten from Hole #1 for Brazilian testing, and ten from Hole #2 for Brazilian testing–were also weighed. The average density calculated from the four samples prepared for UCS testing was 166.5 pcf. The raw data collected to determine the density can be found in Appendix B.

The average density of the samples prepared for Brazilian testing was also calculated in an attempt to determine if a difference in the roof rock material between Holes #1 and #2 could be measured. The average density of samples taken from Holes #1 and #2, as determined from the samples prepared for the Brazilian test, are 165.2 pcf and 167.4 pcf, respectively. The density estimates as determined from Brazilian test specimens should be considered less accurate than those determined from UCS test specimens, because of the shorter specimen lengths used for the Brazilian test.

A.6 Results of Destructive Tests

Three forms of destructive testing were performed: UCS testing, Brazilian testing, and point-load testing. UCS testing was given priority due to the greater sample length required and the ability to get estimates for multiple important material properties from a single test. Then, ten specimens from each core hole were prepared and subjected to Brazilian testing. After UCS and Brazilian testing, the point-load test was performed axially on all extant samples with a length-to-diameter ratio between 0.3:1 and 1.0:1.

A.6.1 UCS Testing

Uniaxial compressive strength testing was performed on four core specimens–three from Hole #1 and one from Hole #2. An MTS 810 load cell with a capacity of 110,000 pounds was used to apply the load. Bedding planes existed in all four samples oriented perpendicular to the loading direction and the long axis of the drill core.

In accordance with ISRM suggestions, a constant rate of compression was applied in such a way as to cause failure in five to ten minutes. To meet this suggestion, a constant

Table A.4: Peak load and unconfined compressive strength of the four samples subjected to UCS testing.

Hole	Sample	Peak Load lb	UCS psi (MPa)
1	1	73900	18800 (130)
1	2	88500	22500 (155)
1	3	90700	22800 (157)
2	4	73000	18400 (127)

stroke rate of 1.2 x 10^{-4} inches per second was used for each of the four specimens. All four specimens failed after five to six minutes of loading [5].

Throughout the testing process, the applied load in pounds and the displacement in inches from the unstressed state were recorded every second. The raw load vs. displacement values and plots can be found in Appendix B. The peak applied load was also recorded for each of the four samples tested. The peak load of each sample and the unconfined compressive strength of each sample is listed in Table A.4.

Stress-strain curves developed from the raw UCS data are shown in Figure A.4. From these, an estimate of Young's modulus can be estimated for each specimen. Determination of Young's modulus for rock specimens is less straightforward than other materials, but it is arguably the most important design parameter [6].

There have been many methods proposed for determining Young's modulus for rock from a stress-strain curve [6]. Young's modulus, which is the slope of the elastic portion of a stress-strain curve, is uniquely difficult to determine for rocks because of the nonlinearity in the early loading stages. This phenomenon, which is widely observed in rock testing, is also present in the curves obtained during this study, as can be seen in Figure A.4.

The ISRM suggests three methods for determining Young's modulus for rocks [7]:

- Tangent modulus–slope of a line tangent to the stress-strain curve at some fixed percentage of the ultimate strength.

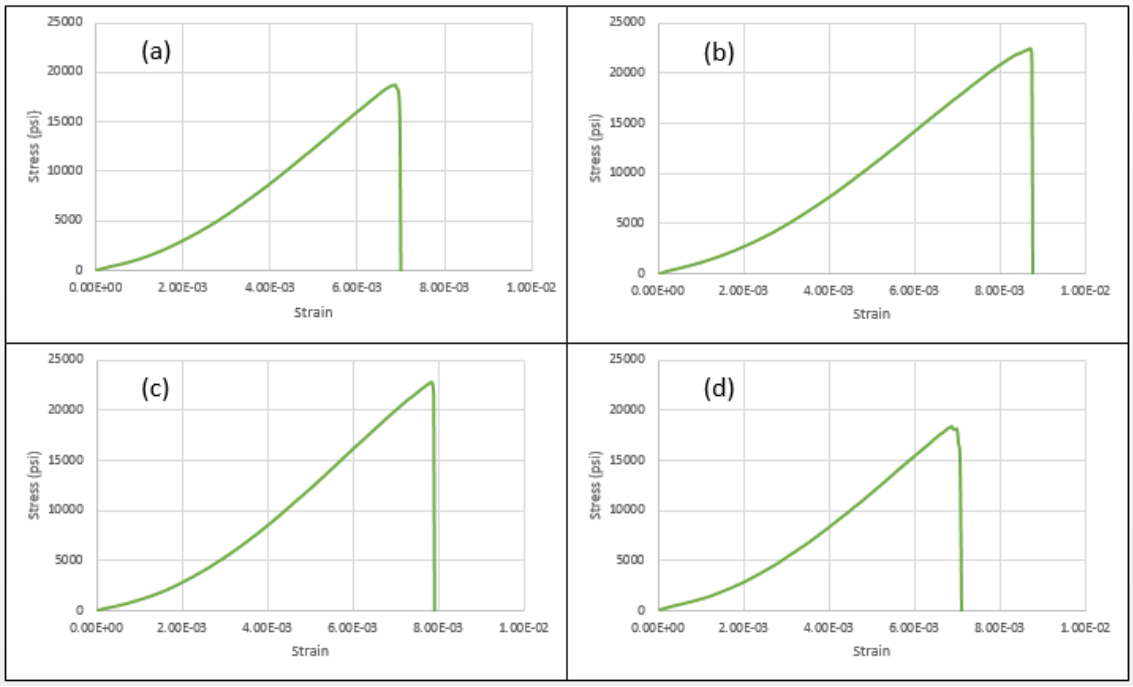

Figure A.4: Stress-strain curves of the four specimens subjected to UCS testing. (a) Sample #1; (b) Sample #2; (c) Sample #3; and (d) Sample #4.

- Average modulus–slope of a line secant to the stress-strain curve around the linear portion.
- Secant modulus–slope of a secant line from the origin to an intersecting point at some fixed percentage of the ultimate strength.

The most commonly chosen fixed percentage of the ultimate strength is the 50% point [7].

Out of the four specimens tested for UCS, one of them from Hole #1 failed along a well defined failure plane. The normal axis of the plane of failure was oriented 60° from the direction of loading. From this failure angle, and knowing that the angle of failure, θ, is related to the angle of internal friction, ϕ, by $2\theta = 90° + \phi$, the angle of internal friction can be estimated to be 30°. Furthermore, cohesion, c, can be calculated from Eq. (A-1). By setting $\sigma_3 = 0$ and $\sigma_1 = 130$ MPa, the stress at failure for that sample, cohesion is found to be 37.5 MPa.

$$\sigma_1 = \sigma_3 \tan^2\theta + 2c\tan\theta \tag{A-1}$$

Table A.5: Tangent elastic modulus, average elastic modulus, and secant elastic modulus of the four samples subjected to UCS testing as determined from the stress-strain curves according to the ISRM suggestions [7]. Moduli are reported in 10^6 psi (GPa).

Hole	Sample	Elastic Modulus		
		Tangent	Average	Secant
1	1	3.65 (25.1)	3.57 (24.6)	2.25 (15.5)
1	2	3.12 (21.5)	3.29 (22.7)	2.20 (15.2)
1	3	3.36 (23.1)	3.80 (26.2)	2.38 (16.4)
2	4	3.34 (23.0)	3.54 (24.4)	2.16 (14.9)

The cores collected granted only a very small number of specimens with a length great enough to perform UCS testing. This small sample size for UCS testing does not aid in the achievement of one of the primary goals–that of determining whether the roof rock surrounding the two holes could be considered one sample or if they are distinct. In order to produce a meaningful conclusion toward that goal regarding compressive strength, the point-load test was performed on a larger sample size.

A.6.2 Brazilian Testing

The Brazilian test was performed on ten specimens from each of the two holes drilled in accordance with the ISRM suggestions [4]. A double layer of masking tape was applied to the circumference of each of the samples and they were placed in the apparatus as shown in Figure A.5. This loading orientation resulted in the load being applied parallel to the laminations in the cores.

The MTS 810 load cell which was used for the UCS testing was also used for the Brazilian tests. A constant stroke rate of 1.2 x 10^{-4} inches per second was applied to each of the samples. In addition to the peak applied load being recorded, the applied load and the total displacement of the loading piston were recorded each second during loading. The

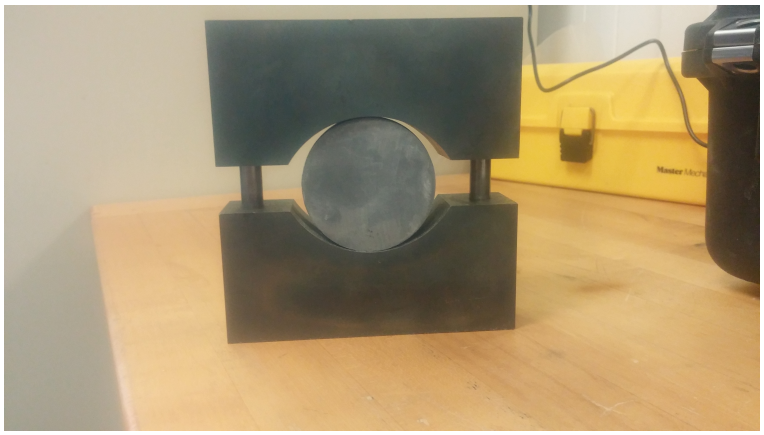

Figure A.5: Specimen prepared for the Brazilian test sitting inside of the apparatus used to apply a load according to ISRM suggestions [4].

raw load vs. displacement plots can be found in Appendix B.

Two of the raw load vs. displacement plots are shown in Figure A.6. These curves, one for a specimen from Hole #1 and one for a specimen from Hole #2, are representative of the shape of a majority of the load vs. displacement curves of other samples from the holes from which each of these specimens were obtained. That is, most of the load vs. displacement curves for specimens from Hole #1 are fairly smooth and linear and free of any irregularities during loading until failure occurs at some peak load, while most of the load vs. displacement curves for specimens from Hole #2 are not.

A majority of the specimens from Hole#1 behaved as brittle materials during the Brazilian test by failing suddenly along the vertical diameter. The specimens from Hole #2, however, mostly crumbled during loading instead of splitting along the vertical diameter. Since the Brazilian test is only valid when failure occurs along the vertical diameter [8], most of the peak load data recorded during testing of specimens from Hole #2 are meaningless.

After discarding results from specimens which did not fail along the vertical diameter, eight meaningful Brazilian test results remained from the sample for Hole #1, but only two results remained from Hole #2. An estimate of the tensile strength, T_0, for the Brazilian test is given by:

$$T_0 = \frac{2P}{\pi D t} \tag{A-2}$$

where P is the load at failure, D is the sample diameter, and t is the sample thickness.

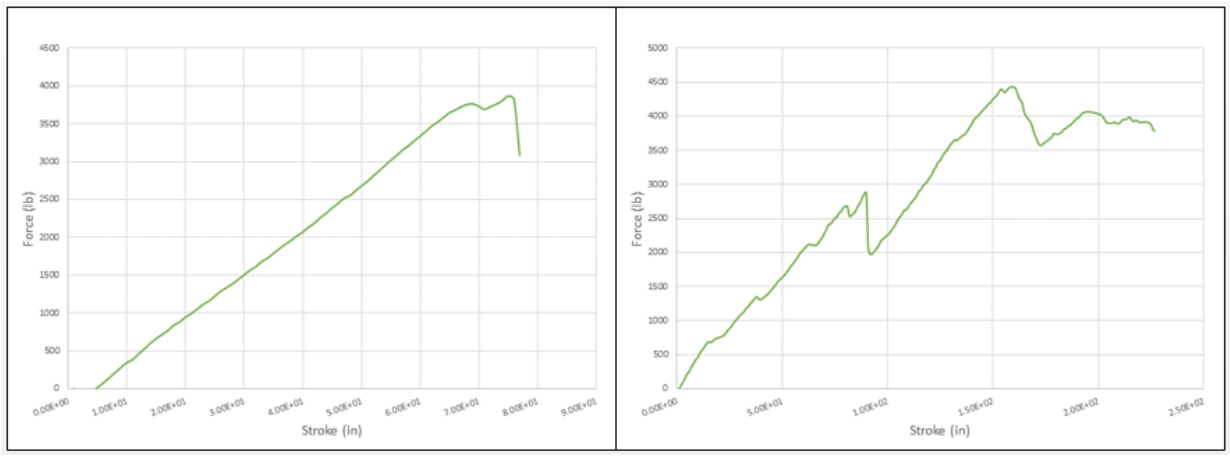

Figure A.6: Raw load vs. displacement curves for Sample #1 from Hole #1 (left) and for Sample #1 from Hole #2 (right).

The ISRM suggested methods often recommend discarding the highest and lowest strength value out of a sample before calculating an average. After discarding the maximum and minimum values, the six remaining median results from Hole #1 have an average of tensile strength value of 1300 psi (9.0 MPa) with a standard deviation of ±82 psi (±0.56 MPa). The average of the only two meaningful values obtained from testing Hole #2 is considerably less at 690 psi (4.7 MPa).

A.6.3 Point-Load Testing

A Roctest Model PIL-7 point load tester was used to perform the point-load test. A load was applied to each specimen by hand using a hydraulic jack until the sample fractured. The load was applied axially on all samples tested. Protocols for point-load tests with diametrical loading of cores are also given by the ISRM [9], but such loading of coal measure rocks is typically not performed due to a lack of meaningful and consistent results [10].

The load applied by the Roctest point-load tester was increased steadily until failure of the specimen occurred. Oil pressure was measured electronically at all times during the test by an electronic gage, and the maximum pressure reached during loading was maintained and recorded. The applied load at failure can be calculated from the oil pressure and the effective area of the jack piston, which is published by the manufacturer.

The point-load test was performed on all rock specimens which were not tested for UCS or tensile strength via the Brazilian test, and which had a length-to-diameter ratio between

0.3:1 and 1.0:1. Ratios of length:diameter of the specimens tested fell between 0.28:1 and 0.87:1. The length-to-diameter ratio restriction is one suggested by the ISRM [9].

The point-load test was performed on thirty-one total specimens, sixteen from Hole #1 and fifteen from Hole #2. The applied load at failure for each of the specimens tested was recorded, and can be found in Appendix B. The results obtained for any test in which the failure surface of a specimen did not intersect the two load points was discarded, as per ISRM suggestions.

Before estimating the UCS from a point-load test, the point load strength index, $I_{s(50)}$, must be calculated. The 50 in the subscript is meant to indicate that the point load index has been standardized for 50 mm diameter core. The point load index for core specimens is calculated from:

$$I_{s(50)} = F\frac{P}{D^2} \tag{A-3}$$

where P is the load at failure, D is the diameter of the core, and F is a correction factor which is only necessary for core diameters which are not 50 mm. The correction factor is calculated from:

$$F = \left(\frac{D}{50\text{ mm}}\right)^{0.45} \tag{A-4}$$

In accordance with ISRM suggestions. the highest and lowest point load indices from each sample were discarded as outliers [9]. The point load strength index is directly proportional to UCS:

$$\text{UCS} = KI_{s(50)} \tag{A-5}$$

The value of K has been extensively studied and has been debated for decades. Early on in the development of the point-load test as an indirect means of estimating the UCS, a K-value of 24 was suggested [2]. Since the inception of the point-load test, K-values ranging from 15 - 30 have been found appropriate for various rock types [11]. A meta-analysis was performed which suggests a K-value equal to 21 can be considered appropriate for coal measure rocks [12].

Assuming a K-value of 21, the distribution of estimates of the uniaxial compressive strength of the samples subjected to the point-load test are plotted in Figure A.7. The UCS

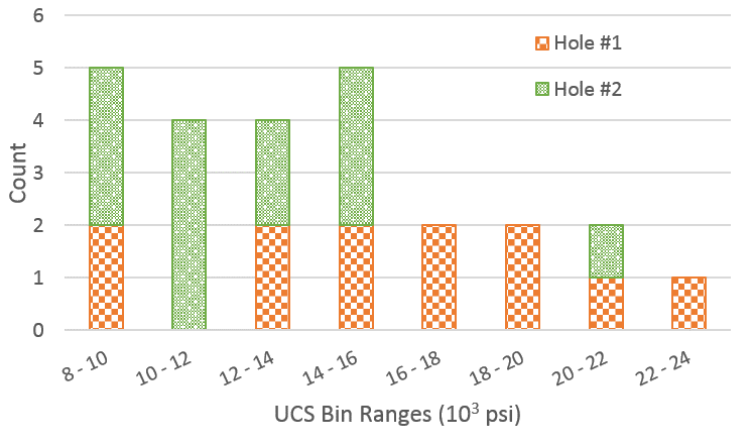

Figure A.7: Distribution of UCS estimates for Holes #1 and #2 as determined from point-load testing with a K-value of 21.

estimates from Holes #1 and #2 cover approximately the same range–from about 8000 psi to 22000 psi. The averages, however, are quite different. The average UCS estimate of all specimens tested from Hole #1 is approximately 16000 psi, while the average UCS estimate of all specimens tested from Hole #2 is about 12800 psi.

Though the point-load test is used primarily as an indirect method of determining uniaxial compressive strength, it is also an indirect tensile strength method. As suggested by the ISRM, the point-load strength index, $I_{s(50)}$, is approximately 0.80 times the uniaxial tensile strength [9]. Using this multiplier, tensile strength was estimated for each of the valid point-load test samples. A histogram of the resulting estimates is shown in Figure A.8.

A.7 Discussion

There were three primary goals at the outset of this study:

- Determining acoustic properties of the roof rock.
- Estimating additional material properties of the roof rock for numerical modeling.
- Concluding whether there is significant variation in the roof rock from Hole #1 to Hole #2.

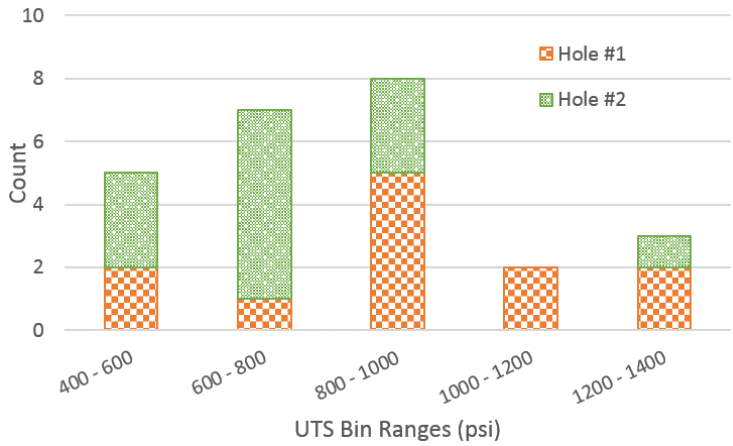

Figure A.8: Distribution of uniaxial tensile strength (UTS) estimates for Holes #1 and #2 as determined from point-load testing.

Acoustic properties were only measured for four samples. Of those four, the average s- and p-wave velocities were found to be 7640 ft/sec (2510 m/s) and 12200 ft/sec (3990 m/s), respectively. From these magnitudes, the ratio of s-wave velocity to p-wave velocity, V_s/V_p, is estimated at 0.62. Knowledge of the wave velocity magnitudes as well as the velocity ratio allows for greater accuracy and higher confidence in the locating of seismic events, which will aid in the passive seismic survey performed at this mine site.

In addition to the acoustic properties, estimates of other material properties of the roof rock were sought for use as inputs in numerical models. Properties to be used as inputs into numerical models include density, elastic moduli, UCS and tensile strength, cohesion, and angle of internal friction. The 95% confidence interval for density of the twenty-four samples cut and ground was found to be 166.3 ± 3.08 pcf.

Three methods were used to determine Young's modulus of the four specimens subjected to UCS testing, namely: the tangent elastic modulus, the average elastic modulus, and the secant elastic modulus. Other methods for estimating a Young's modulus for rock have been suggested. A majority of them would be expected to result in very similar values to those obtained here.

The various methods for estimating Young's modulus has been studied extensively for differing rock types [6]. The method which showed the greatest consistency for rocks experiencing plastic-elastic stress-strain curves was found to be the "modified secant modulus at 50 percent maximum stress." This value is defined as the slope of the line from the 50%

maximum stress point to the intersection of the linear portion of the stress-strain curve and the strain-axis. For the four samples tested, the modified secant modulus at 50 percent maximum stress was found to be identical to the tangent modulus at 50 percent maximum stress calculated previously. The average Young's modulus of the four samples is then 23.2 GPa. With an estimate of Young's modulus and Poisson's ratio, any of the other four elastic moduli can be estimated.

The UCS testing suggests a uniaxial compressive strength of the roof rock of approximately 140 MPa. Applying a K-value of 21 in Eq. (A-5) results in a UCS estimate of 99 MPa. Though the sample size is small for the UCS testing, this implies a higher K-value is more appropriate for this dataset. A K-value of approximately 30 results in the UCS indirectly estimated from the point-load strength index to be approximately 140 MPa.

Success of the Brazilian test as an indirect measure of tensile strength requires that the material being tested act homogeneously and in a brittle manner [8]. Brittle fracture occurred during loading in many of the specimens from Hole #2, but only partially. The specimens would experience fracturing which was limited to only a few of the laminations present, while other layers would maintain integrity. This phenomenon is reflected in the stress-strain curves for the Hole #2 specimens in the multiple local peaks in stress followed by the sudden shedding of some of the applied load. As can be seen from the stress-strain curves in Figure A.6, and in the Figures in Appendix B, many of the specimens in the sample from Hole #2 did not behave in a brittle, homogeneous manner.

A primary purpose of this laboratory study was to compile a list of material properties for the roof material above this room-and-pillar coal mine to be used as first estimates in numerical models. A list of these material properties is given in Table A.6. Small sample sizes were available in all testing procedures performed, so the values listed are considered only first estimates for numerical modeling. The values for cohesion and angle on internal friction, for instance, were determined from a single specimen.

The material property values listed in Table A.6 match well with previously published values for shale with the exception of the cohesion and the angle of internal friction [13]. Both of these values were determined from a single UCS specimen by using Eq. (A-1). Because of the small sample size and the fact that the two values are significantly above published ranges, the cohesion and the angle of internal friction values listed in Table A.6 were not used as numerical modeling inputs.

Another primary goal of this laboratory study was to determine if the material properties of the roof material around Hole #1 and Hole #2 should be considered similar enough

Table A.6: Material properties of the roof rock as determined from this series of laboratory tests.

Parameter	Unit	Value
Density	$^{kg}/_{m^3}$	2670
P-wave velocity	$^{m}/_{s}$	3700
S-wave velocity	$^{m}/_{s}$	2330
Young's modulus	GPa	23.2
Compressive strength	MPa	142
Tensile strength	MPa	7.84
Cohesion	MPa	37.5
Angle of internal friction	$^{\circ}$	30

to group them both into a single material, or if they should be considered distinct. Any statistical basis for claiming that Holes #1 and #2 should be considered distinct samples and not of the same dataset could only come from the point-load test results. The UCS test was not performed on enough samples to conclude any difference. The fact that the specimens from Hole #2 crumbled during Brazilian testing, as well as during sample preparation, indicated that the roof rock around Hole #2 contains weaker laminations, but that evidence was nonexistent numerically.

The averages of the point load strength indices for the specimens from Holes #1 and #2 are quite different, but hypothesis testing proves inconclusive. The null hypothesis stating that they contain the same mean cannot be rejected from the data collected. While it is not backed statistically, it is clear that the two materials behave quite differently. A difference in material properties was surmised upon initial inspection, and evidence for it was seen during sample preparation and from the lack of sample integrity during Brazilian testing of specimens from Hole #2. It is likely that any weakness in the specimens from Hole #2 exists only due to the laminations which are not as prevalent in Hole #1.

The material properties listed in Table A.6, among others, will be used for numerical modeling of the roof rock. The entire roof will be modeled as a jointed rock mass where the intact rock has the properties listed in Table A.6. The material properties of the joints, however, will reflect the difference in strength between the roof rock around Holes #1 and #2.

Poor sample preparation can often contribute to error in the final strength estimates. According to the ISRM, substandard preparation of samples can result in premature failure, and a low estimate of strength [5]. While the samples prepared for this study did not meet the tolerances suggested by the ISRM, the strength estimates found in this study are well above published averages.

A.8 Conclusions

A series of lab tests was performed on core collected from the roof rock above a retreating room-and-pillar coal mine in the Eastern US. The drilling was performed in order to install triaxial geophones as part of a passive seismic study of the retreat process. Approximately eleven feet of sandy shale core was collected for the testing.

Three goals motivated the laboratory testing: estimating the p- and s-wave velocities of the roof rock in order to aid in event location for the passive seismic study; determining first estimates of other material properties for use in numerical models; and assessing whether the roof rock surrounding the two holes can be considered the same material, or if there is a statistically significant difference between them.

A list of the material properties, including the acoustic properties, is given in Table A.6. These properties will improve the accuracy of the passive seismic event locating in the seismic survey and will aid in numerical model generation. While no significant difference was found between the material properties of the roof rock around Holes #1 and #2, a difference became evident during sample preparation and performing the Brazilian test. The difference in integrity between specimens from Hole #1 and Hole #2 is assumed to be due to the presence of laminations in the core taken from Hole #2, which will be reflected in numerical models by a reduction in joint strength properties.

Works Cited

[1] William J Conrad. Microseismic monitoring of a room and pillar retreat coal mine in southwest virginia. Master's thesis, Virginia Polytechnic Institute and State University (Virginia Tech), 2016.

[2] E. Broch and J.A. Franklin. The point-load strength test. *International Journal of Rock Mechanics and Mining Sciences & Geomechanics Abstracts*, 9(6):669 – 676, 1972.

[3] DU Deere. Geological considerations. *Rock mechanics in engineering practice*, pages 1–20, 1968.

[4] ZT Bieniawski and I Hawkes. Suggested methods for determining tensile strength of rock materials. In *International Journal of Rock Mechanics and Mining Sciences & Geomechanics Abstracts*, volume 15, pages 99–103. Elsevier, 1978.

[5] ZT Bieniawski and MJ Bernede. Suggested methods for determining the uniaxial compressive strength and deformability of rock materials: Part 1. suggested method for determination of the uniaxial compressive strength of rock materials. In *International Journal of Rock Mechanics and Mining Sciences & Geomechanics Abstracts*, volume 16 (2), page 137. Elsevier, 1979.

[6] Paul M Santi, Jason E Holschen, and Richard W Stephenson. Improving elastic modulus measurements for rock based on geology. *Environmental & Engineering Geoscience*, 6(4):333–346, 2000.

[7] ZT Bieniawski and MJ Bernede. Suggested methods for determining the uniaxial compressive strength and deformability of rock materials: Part 2. suggested method for determining deformability of rock material in uniaxial compression. In *International Journal of Rock Mechanics and Mining Sciences & Geomechanics Abstracts*, volume 16 (2), pages 138–140. Elsevier, 1979.

[8] Malcolm Mellor and Ivor Hawkes. Measurement of tensile strength by diametral compression of discs and annuli. *Engineering Geology*, 5(3):173–225, 1971.

[9] JA Franklin. Suggested method for determining point load strength. In *International Journal of Rock Mechanics and Mining Sciences & Geomechanics Abstracts*, volume 22 (2), pages 51–60. Elsevier, 1985.

[10] Norman Brook. *Comprehensive rock engineering: principles, practice, & projects*, volume 3. Pergamon Press Ltd, 1993.

[11] Jeff S Cargill and A Shakoor. Evaluation of empirical methods for measuring the uniaxial compressive strength of rock. In *International Journal of Rock Mechanics and Mining Sciences & Geomechanics Abstracts*, volume 27 (6), pages 495–503. Elsevier, 1990.

[12] John Rusnak and Christopher Mark. Using the point load test to determine the uniaxial compressive strength of coal measure rock. In *Proceedings of the 19th International Conference on Ground Control in Mining. Morgantown, WV: West Virginia University*, pages 362–371, 2000.

[13] Essie Esterhuizen, Chris Mark, and Michael M Murphy. Numerical model calibration for simulating coal pillars, gob and overburden response. In *Proceeding of the 29th international conference on ground control in mining, Morgantown, WV*, pages 46–57, 2010.

Appendix B

Raw Lab Data

B.1 Dimension Measurement after Specimen Preparation

Table B.1: All diameter measurements made on the samples subjected to uniaxial compression strength (UCS) tests after sample preparation.

	Sample #	1	2	3	4
	Hole #	1	1	1	2
Diameter #	Location	Measurements in inches			
1	Top	2.232	2.236	2.256	2.249
2	Top	2.240	2.239	2.255	2.251
1	Middle	2.234	2.232	2.255	2.243
2	Middle	2.230	2.238	2.250	2.240
1	Bottom	2.242	2.237	2.250	2.245
2	Bottom	2.244	2.244	2.252	2.246

Table B.2: All length measurements made on the samples subjected to uniaxial compression strength (UCS) tests after sample preparation.

	Sample #	1	2	3	4
	Hole #	1	1	1	2
Length #	Location	Measurements in inches			
1	0°	5.602	4.425	5.352	5.472
2	120°	5.610	4.424	5.352	5.462
3	240°	5.608	4.425	5.352	5.458

Table B.3: All flatness measurements made on the samples subjected to uniaxial compression strength (UCS) tests after sample preparation. The absolute magnitudes are meaningless. The values listed are measurements in milli-inches made to determine the degree of variation in end flatness. That is, the relative magnitudes indicate the degree to which an end varies in 10^{-3} inches.

		Sample #	1	2	3	4
		Hole #	1	1	1	2
End #	Diameter #	Measurement #	Values			
1	1	1	34	0	23	20
1	1	2	40	5	21	30
1	1	3	43	7	10	40
1	2	1	45	3	20	20
1	2	2	40	5	20	30
1	2	3	31	5	20	40
1	3	1	50	7	10	32
1	3	2	40	5	20	30
1	3	3	30	0	23	30
2	1	1	25	2	23	28
2	1	2	40	6	21	30
2	1	3	50	6	15	21
2	2	1	38	7	15	20
2	2	2	40	5	20	31
2	2	3	40	0	25	40
2	3	1	47	10	12	26
2	3	2	40	5	22	30
2	3	3	30	0	28	34

Table B.4: Measured dimensions of the ten samples from Hole #1 after sample preparation which were subjected to the Brazil test. Diameter and thickness measurements listed in inches.

Sample #	Diameter	Thickness
1	2.235	1.140
2	2.233	1.167
3	2.241	1.134
4	2.237	1.123
5	2.234	1.131
6	2.243	1.188
7	2.246	1.146
8	2.244	1.174
9	2.242	1.183
10	2.234	1.201

Table B.5: Measured dimensions of the ten samples from Hole # 2 after sample preparation which were subjected to the Brazil test. Diameter and thickness measurements listed in inches.

Sample #	Diameter	Thickness
1	2.223	1.160
2	2.237	1.165
3	2.236	1.083
4	2.239	1.114
5	2.245	1.230
6	2.223	1.091
7	2.242	1.152
8	2.281	1.107
9	2.270	1.141
10	2.231	1.153

B.2 Acoustic Properties

Table B.6: Measured arrival times of the s-type waveform.

Measurement	Location	Sample #			
		1	2	3	4
Arrival time without sample in μs	Trough 1	23.6	21.4	21.6	21.4
	Peak 1	39.2	36.8	36.8	36.8
	Trough 2	54	51.2	51.4	51.2
	Peak 2	68.8	65.6	66.0	66.4
Arrival time with sample in μs	Trough 1	84.8	72.0	80.0	76.0
	Peak 1	101.6	86.4	93.6	93.6
	Trough 2	114.0	100.0	111.0	111.0
	Peak 2	130.4	115.2	125.6	125.2

Table B.7: Averaged s-type travel times, measured p-arrivals and length, and calculated p- and s-wave velocities through the four samples subjected to UCS testing. Average s-wave travel time is determined by averaging the difference between the measured arrivals with and without the sample present. Wave velocities are the ratio of the sample length to the travel time measured/calculated.

Parameter	Unit	Sample #			
		1	2	3	4
S Arrival	μs	61.3	49.	58.6	57.5
P Arrival	μs	37.6	30.8	36.4	38
Length	(in.)	5.607	4.425	5.352	5.464
S Velocity	(ft/sec)	7620	7430	7610	7920
P Velocity	(ft/sec)	12400	12000	12300	12000

B.3 Density

Table B.8: Density of the four UCS samples.

Hole	Sample	Volume in.^{3}	Weight oz.	Density pcf
1	1	22.04	34.055	166.9
1	2	17.40	26.760	166.1
1	3	21.34	32.80	166.0
2	4	21.64	33.435	166.9

Table B.9: Density of the ten specimens comprising the Brazil test sample from Hole #1.

Sample	Volume in.^{3}	Weight oz.	Density pcf
1	4.472	6.880	166.1
2	4.570	6.960	164.5
3	4.473	6.830	164.9
4	4.414	6.715	164.3
5	4.433	6.745	164.3
6	4.694	7.190	165.4
7	4.540	6.945	165.2
8	4.643	7.070	164.5
9	4.670	7.240	167.4
10	4.708	7.225	165.8

Table B.10: Density of the ten specimens comprising the Brazil test sample from Hole #2.

Sample	Volume in.^{3}	Weight oz.	Density pcf
1	4.502	6.975	167.3
2	4.579	7.035	165.9
3	4.253	6.480	164.6
4	4.386	6.875	169.3
5	4.869	7.535	167.1
6	4.234	6.660	169.9
7	4.548	7.050	167.4
8	4.524	7.005	167.2
9	4.618	7.225	169.0
10	4.517	6.925	165.9

B.4 Raw Load-Displacement Curves

B.4.1 Uniaxial Compressive Strength Tests

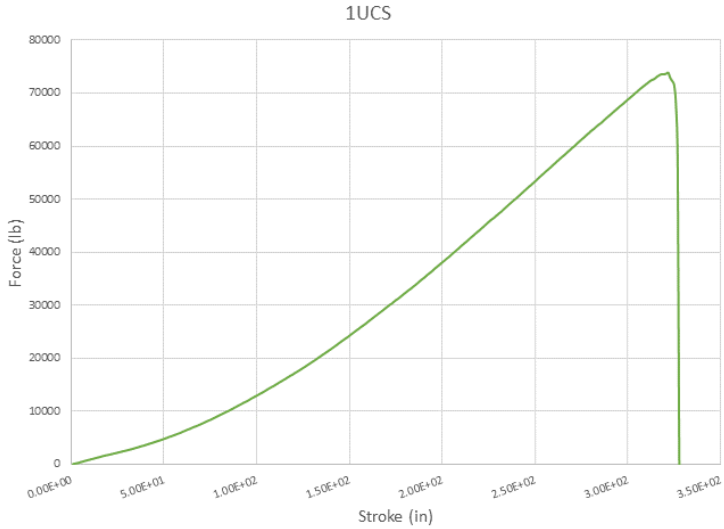

Figure B.1: Raw load-displacement curve recorded during UCS testing of Sample #1.

Figure B.2: Raw load-displacement curve recorded during UCS testing of Sample #2.

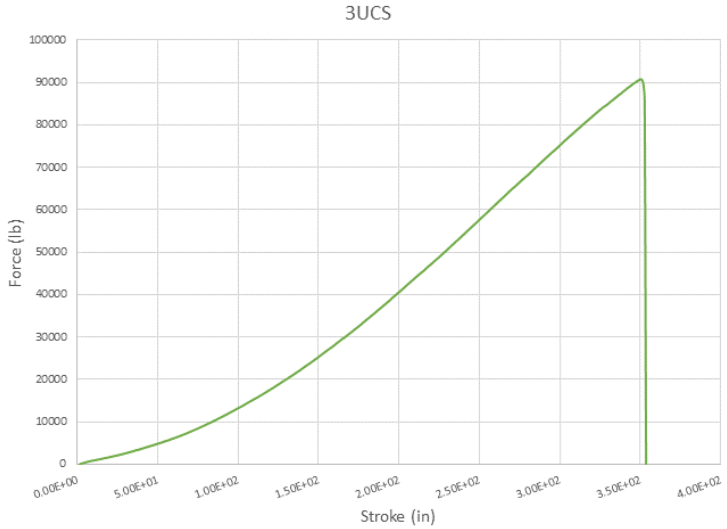

Figure B.3: Raw load-displacement curve recorded during UCS testing of Sample #3.

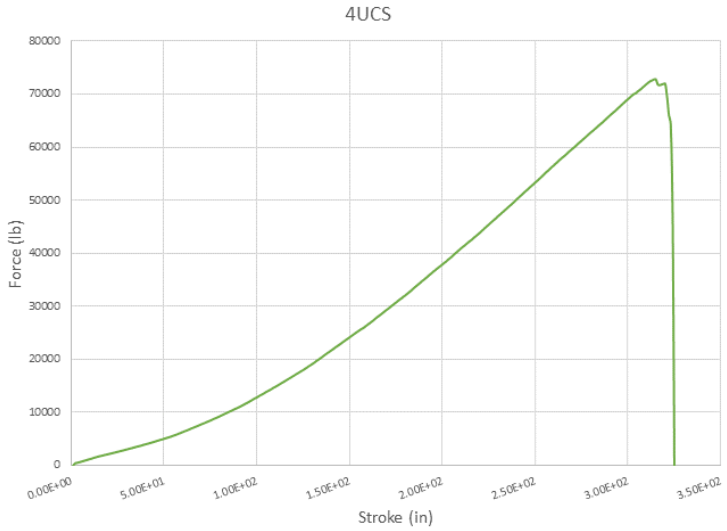

Figure B.4: Raw load-displacement curve recorded during UCS testing of Sample #4.

B.4.2 Brazil Test on Sample from Hole #1

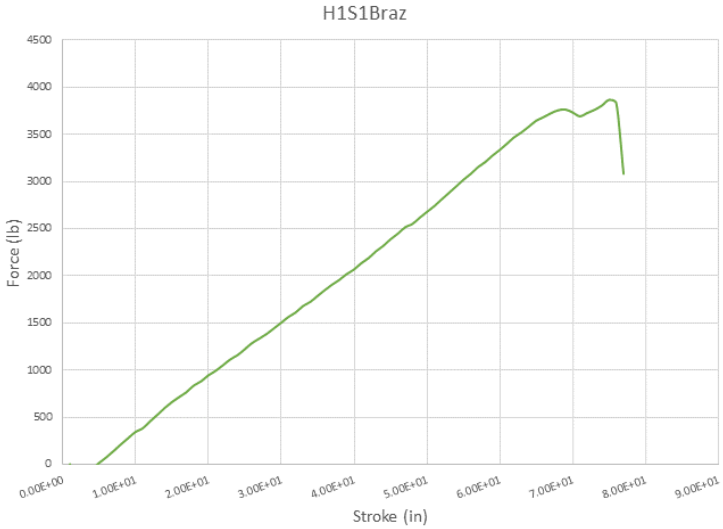

Figure B.5: Raw load-displacement curve recorded during Brazil test for Sample #1 of Hole #1.

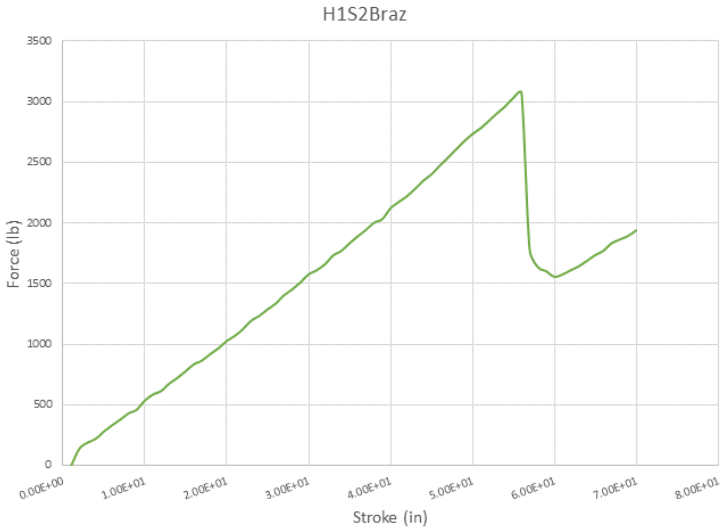

Figure B.6: Raw load-displacement curve recorded during Brazil test for Sample #2 of Hole #1.

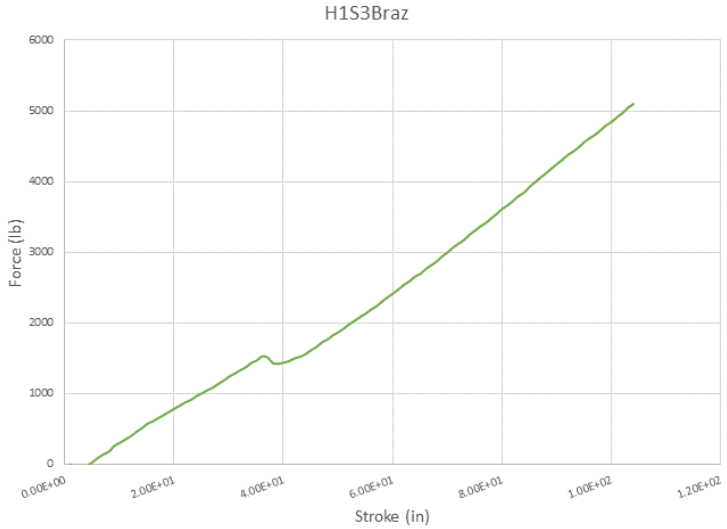

Figure B.7: Raw load-displacement curve recorded during Brazil test for Sample #23 of Hole #1.

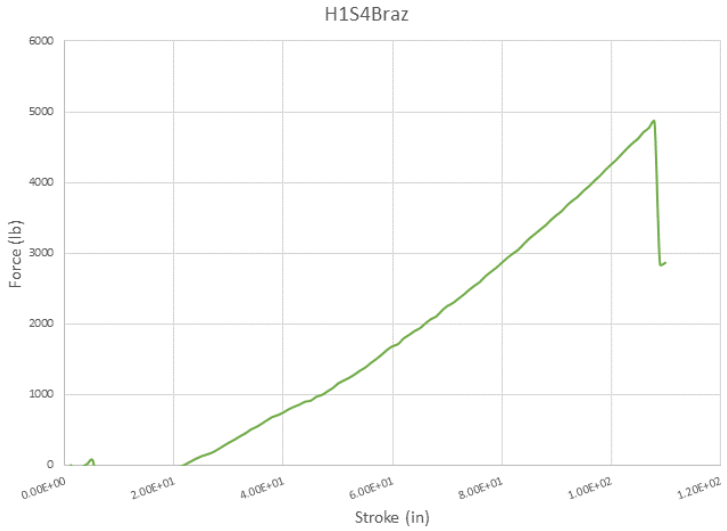

Figure B.8: Raw load-displacement curve recorded during Brazil test for Sample #4 of Hole #1.

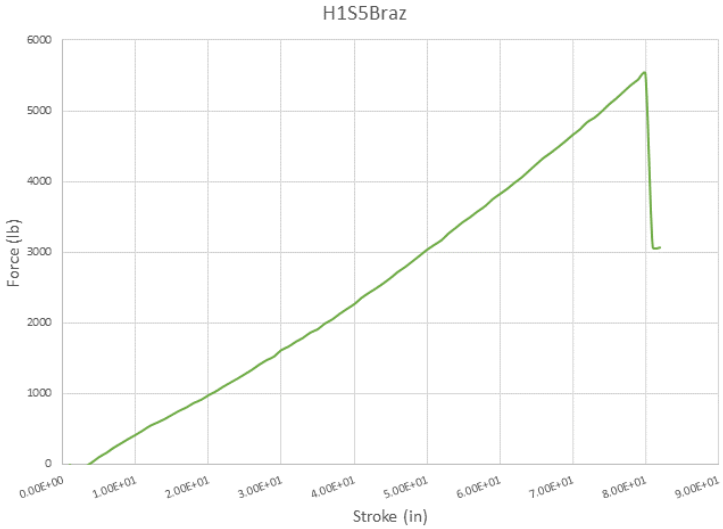

Figure B.9: Raw load-displacement curve recorded during Brazil test for Sample #5 of Hole #1.

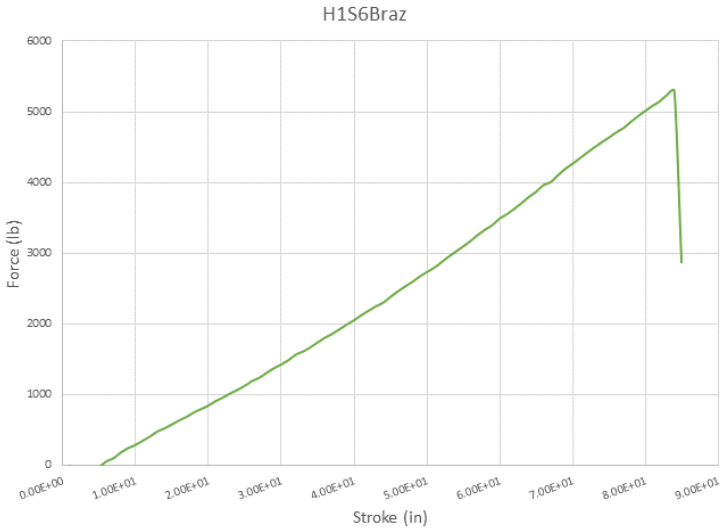

Figure B.10: Raw load-displacement curve recorded during Brazil test for Sample #6 of Hole #1.

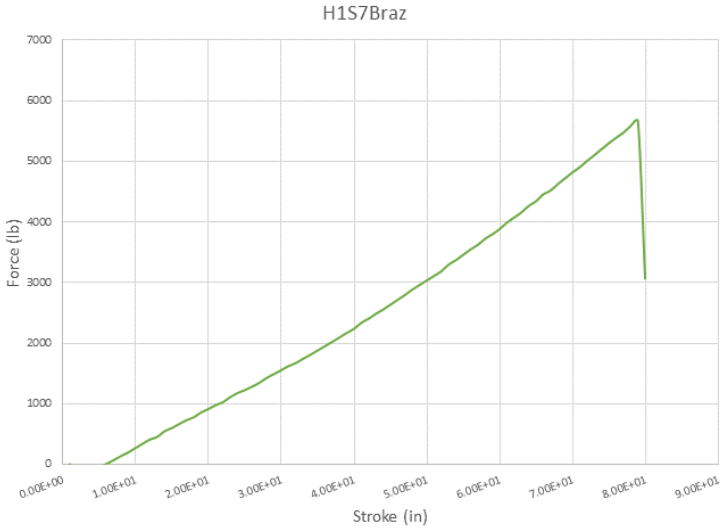

Figure B.11: Raw load-displacement curve recorded during Brazil test for Sample #7 of Hole #1.

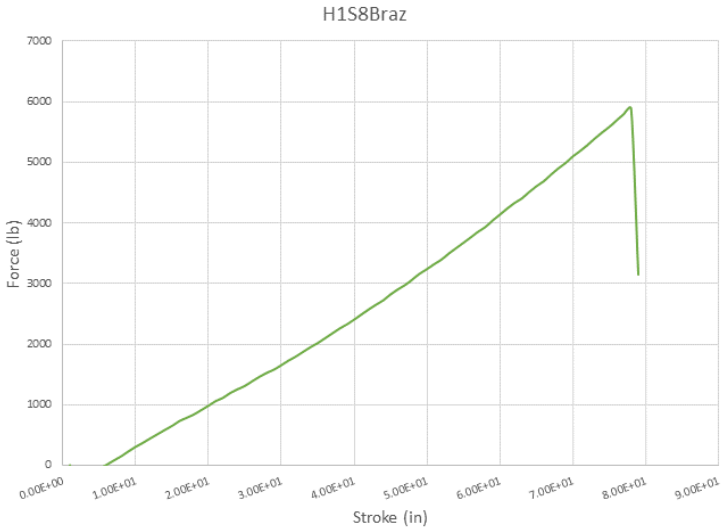

Figure B.12: Raw load-displacement curve recorded during Brazil test for Sample #8 of Hole #1.

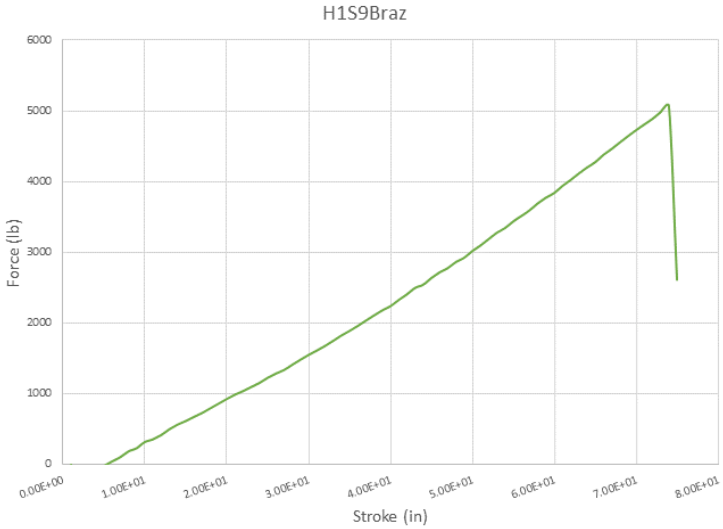

Figure B.13: Raw load-displacement curve recorded during Brazil test for Sample #9 of Hole #1.

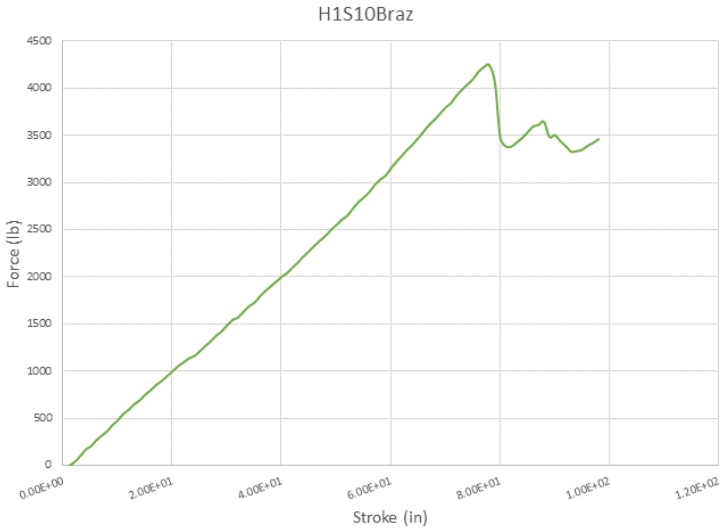

Figure B.14: Raw load-displacement curve recorded during Brazil test for Sample #10 of Hole #1.

B.4.3 Brazil Test on Sample from Hole #2

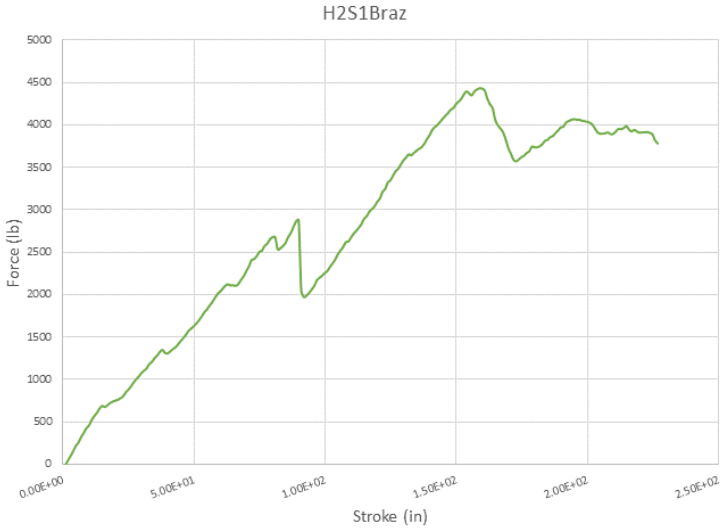

Figure B.15: Raw load-displacement curve recorded during Brazil test for Sample #1 of Hole #2.

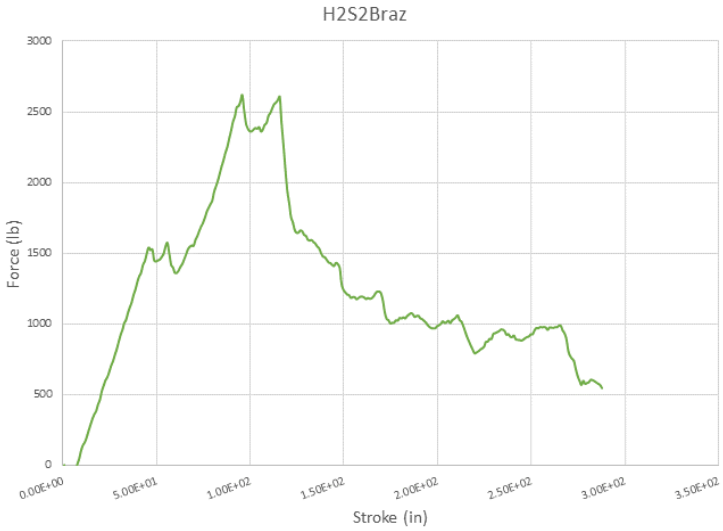

Figure B.16: Raw load-displacement curve recorded during Brazil test for Sample #2 of Hole #2.

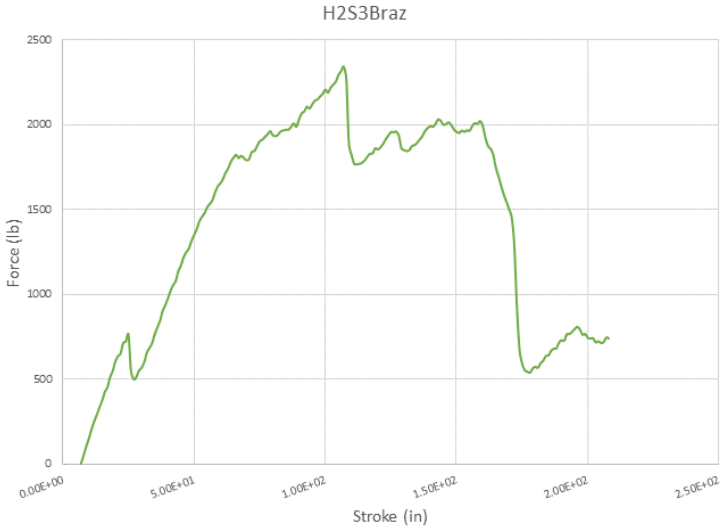

Figure B.17: Raw load-displacement curve recorded during Brazil test for Sample #3 of Hole #2.

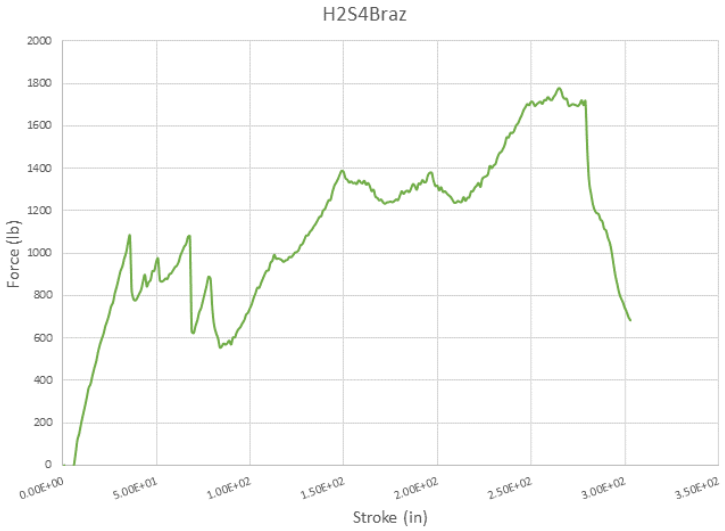

Figure B.18: Raw load-displacement curve recorded during Brazil test for Sample #4 of Hole #2.

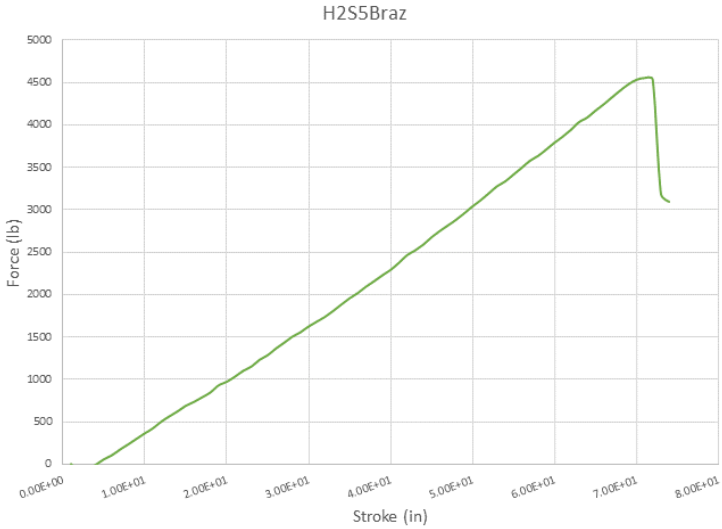

Figure B.19: Raw load-displacement curve recorded during Brazil test for Sample #5 of Hole #2.

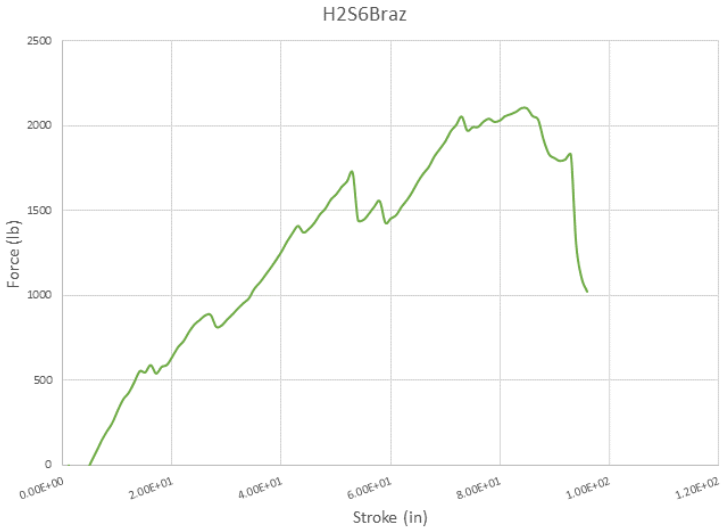

Figure B.20: Raw load-displacement curve recorded during Brazil test for Sample #6 of Hole #2.

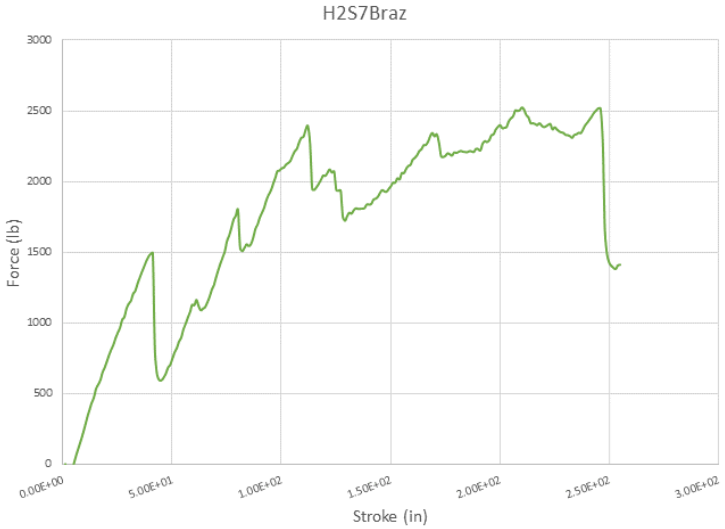

Figure B.21: Raw load-displacement curve recorded during Brazil test for Sample #7 of Hole #2.

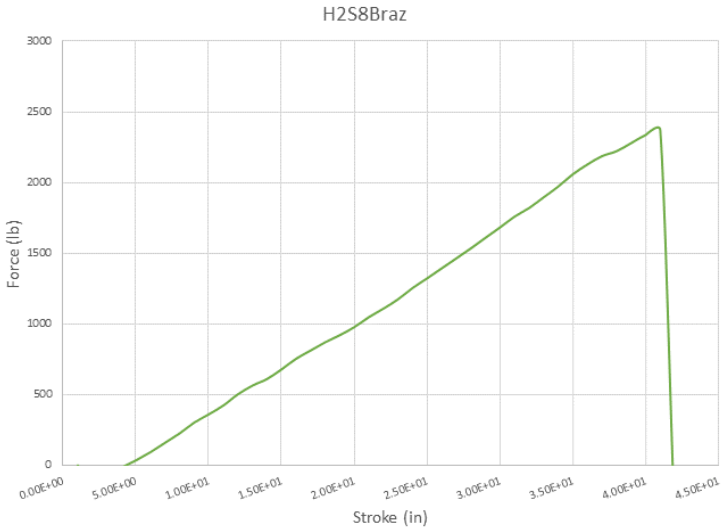

Figure B.22: Raw load-displacement curve recorded during Brazil test for Sample #8 of Hole #2.

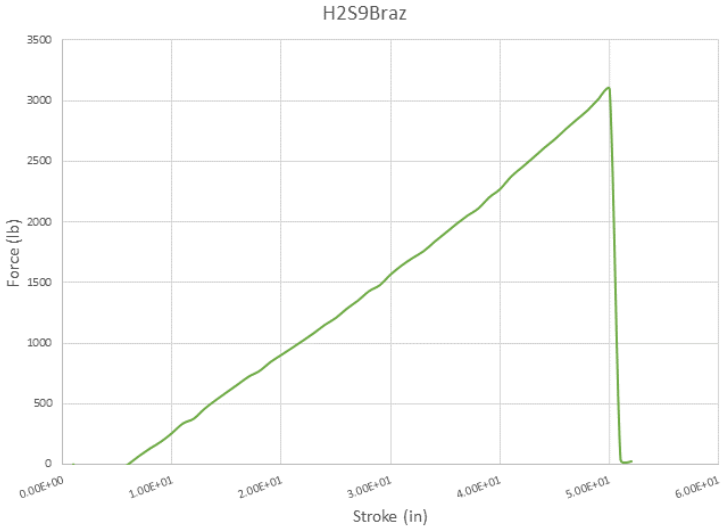

Figure B.23: Raw load-displacement curve recorded during Brazil test for Sample #9 of Hole #2.

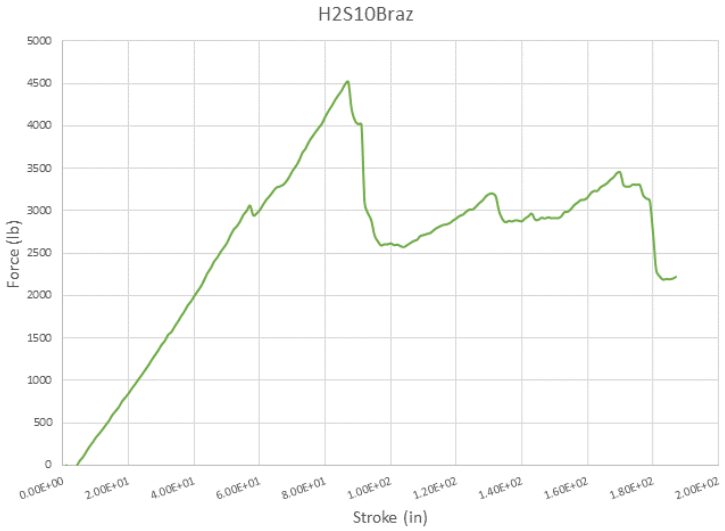

Figure B.24: Raw load-displacement curve recorded during Brazil test for Sample #10 of Hole #2.

B.5 Strength Calculations

B.5.1 Uniaxial Compressive Strength

Table B.11: Peak load and unconfined compressive strength of the four samples subjected to UCS testing where UCS, C_0, is determined from $C_0 = \frac{P}{A}$; where P is the peak load and A is the cross-sectional area of the sample.

Hole	Sample	Peak Load lb	UCS psi (MPa)
1	1	73900	18800 (130)
1	2	88500	22500 (155)
1	3	90700	22800 (157)
2	4	73000	18400 (127)

B.5.2 Indirect Tensile Strength via Brazil Test

Table B.12: Peak applied load to the ten specimens comprising the sample from Hole #1. A boolean value also accompanies each sample entry which indicates whether the specimen failed along the vertical diameter–indicating a valid test.

Sample	Peak Load lb	Valid Test
1	3909	FALSE
2	3070	TRUE
3	5118	TRUE
4	4886	TRUE
5	5583	TRUE
6	5346	TRUE
7	5677	TRUE
8	5943	TRUE
9	5075	TRUE
10	4274	FALSE

Table B.13: Peak applied load to the ten specimens comprising the sample from Hole #2. A boolean value also accompanies each sample entry which indicates whether the specimen failed along the vertical diameter–indicating a valid test.

Sample	Peak Load lb	Valid Test
1	4454	FALSE
2	2672	FALSE
3	2346	FALSE
4	1801	FALSE
5	4578	FALSE
6	2133	FALSE
7	2557	FALSE
8	2394	TRUE
9	3120	TRUE
10	4557	FALSE

Table B.14: Peak load and indirect estimate of tensile strength of the ten specimens which gave meaningful results by failing along the vertical diameter.

Hole	Sample	Peak Load lb	Tensile Strength psi (MPa)
1	2	3070	750 5.17
1	3	5120	1280 8.83
1	4	4890	1240 8.53
1	5	5580	1410 9.69
1	6	5350	1280 8.80
1	7	5680	1400 9.67
1	8	5940	1440 9.89
1	9	5080	1220 8.39
2	8	2390	604 4.16
2	9	3120	767 5.28

B.6 Point-Load Tests

Table B.15: Sample dimensions and pressure of the hydraulic fluid measured at failure for the fifteen specimens comprising the Hole #1 sample subjected to the point load test. A boolean value also accompanies each sample entry which indicates whether the fracture surface of the specimen passed through both loading points–indicating a valid test.

Sample	Diameter in.	Length mm	Oil Pressure psi	Valid Test
1	2.234	27	2126	TRUE
2	2.245	17	1523	TRUE
3	2.242	29	1917	TRUE
4	2.250	20	1218	TRUE
5	2.250	32	2587	TRUE
6	2.237	21	1247	TRUE
7	2.242	42	2976	TRUE
8	2.247	36	3260	TRUE
9	2.235	34	2553	TRUE
10	2.24	45	3687	TRUE
11	2.243	27	2384	TRUE
12	2.252	34	2448	TRUE
13	2.254	49	3519	TRUE
14	2.241	39	2938	TRUE
15	2.250	39	—	FALSE

Table B.16: Sample dimensions and pressure of the hydraulic fluid measured at failure for the fifteen specimens comprising the Hole #2 sample subjected to the point load test. A boolean value also accompanies each sample entry which indicates whether the fracture surface of the specimen passed through both loading points–indicating a valid test.

Sample	Diameter in.	Length mm	Oil Pressure psi	Valid Test
1	2.249	40	3594	TRUE
2	2.236	24	2376	TRUE
3	2.234	20	1685	TRUE
4	2.226	43	1300	TRUE
5	2.222	43	2025	TRUE
6	2.218	49	—	FALSE
7	2.231	20	1784	TRUE
8	2.242	23	1987	TRUE
9	2.246	22	2405	TRUE
10	2.245	32	3316	TRUE
11	2.223	40	1505	TRUE
12	2.222	32	2277	TRUE
13	2.25	17	1630	TRUE
14	2.241	16	1279	TRUE
15	2.248	17	1398	TRUE
16	2.247	22.5	1819	TRUE

Table B.17: Values calculated to determine a UCS estimate from the point-load test for the valid test specimens in the sample from Hole#1. Peak load is calculated by multiplying the hydraulic pressure listed in Table B.16 by the effective jack piston area (1.469 in). Point load index is determined as outline in [1]. UCS is estimated using the multiplier suggested in [2].

Sample	Peak Load lb	Point Load Index psi	UCS Estimate psi
1	3120	663	13900
2	2240	471	9890
3	2820	594	12500
4	1790	375	7880
5	380	797	16700
6	1830	388	8100
7	4370	922	19400
8	4790	1010	21100
9	3750	795	16700
10	5420	1140	24000
11	3500	738	15500
12	3600	754	15800
13	5170	1080	22700
14	4320	911	19100

Table B.18: Values calculated to determine a UCS estimate from the point-load test for the valid test specimens in the sample from Hole#2. Peak load is calculated by multiplying the hydraulic pressure listed in Table B.16 by the effective jack piston area (1.469 in). Point load index is determined as outline in [1]. UCS is estimated using the multiplier suggested in [2].

Sample	Peak Load lb	Point Load Index psi	UCS Estimate psi
1	5280	1100	23000
2	3490	740	15500
3	2480	525	11000
4	1910	407	8560
5	2980	636	13400
7	2620	557	11700
8	2920	616	12900
9	3530	743	15600
10	4870	1030	21500
11	2210	473	9930
12	3350	716	15000
13	2400	502	10600
14	1880	397	8330
15	2050	432	9060
16	2670	562	11800

Works Cited

[1] JA Franklin. Suggested method for determining point load strength. In *International Journal of Rock Mechanics and Mining Sciences & Geomechanics Abstracts*, volume 22 (2), pages 51–60. Elsevier, 1985.

[2] John Rusnak and Christopher Mark. Using the point load test to determine the uniaxial compressive strength of coal measure rock. In *Proceedings of the 19th International Conference on Ground Control in Mining. Morgantown, WV: West Virginia University*, pages 362–371, 2000.

Appendix C

Constitutive Model Implementation

C.1 Preface

This appendix was created to house all information required for the creation and implementation of the constitutive model in FLAC3D, which was mentioned in Chapters 3 and 4. The ideas contained in this appendix are in no way original. Tresca's constitutive model is over 150 years old, and the theories of plasticity discussed here can be found in many texts.

Nearly the entirety of the information contained in this appendix was gleaned from three invaluable resources. Constitutive models and theories of plasticity are discussed at great length in two volumes in a format and from a basis which the author found uniquely accessible: one volume on elasticity and modeling by Chen and Saleeb [1] and one volume on plasticity and modeling by Chen alone [2]. Also, the value of the FLAC3D User's Manual [3] in completing this task cannot be overstated. This appendix, which could not have been created without reference to these works, will be free of citations to them after this point.

C.2 Introduction to Plasticity Theory

Hooke's Law, shown in Eq. (C-1), describes the deformation of materials within the elastic region, and can be assumed to be valid until the yield strength is reached. Loading past the yield strength requires Plasticity Theory. Theories of plasticity traditionally follow one of two forms: the deformation theory of plasticity, or the incremental theory of plasticity, also called flow theory. The deformation theory of plasticity is the simpler of the two, and is limited in

that it assumes that no volume change occurs during plastic deformation. The theory also results in strain being simply a function of stress, which clearly ignores history-dependence, irreversibility, and strain-softening materials.

$$\begin{aligned} \epsilon_x &= \tfrac{1}{E}\left[\sigma_x - \nu\left(\sigma_y + \sigma_z\right)\right] \\ \epsilon_y &= \tfrac{1}{E}\left[\sigma_y - \nu\left(\sigma_x + \sigma_z\right)\right] \\ \epsilon_z &= \tfrac{1}{E}\left[\sigma_z - \nu\left(\sigma_x + \sigma_y\right)\right] \end{aligned} \tag{C-1}$$

The incremental theory of plasticity instead implements a stress increment-strain increment relationship. To develop this relationship, the total strain increment, $d\epsilon$, is considered to be composed of an elastic strain increment, $d\epsilon^e$, and a plastic strain increment, $d\epsilon^p$, as shown in Eq. (C-2).

$$d\epsilon = d\epsilon^e + d\epsilon^p \tag{C-2}$$

The elastic portion of the total strain increment is given by Hooke's Law (Eq. C-1). The limits of elasticity are defined by a yield surface, $f\left(\sigma_1, \sigma_2, \sigma_3\right)$, where:

$$\begin{aligned} f > 0 &: \text{ elastic} \\ f = 0 &: \text{ plastic} \end{aligned} \tag{C-3}$$

A stress increment which causes plasticity as defined by Eq. (C-3) will cause incremental plastic strain, $d\epsilon^p$ of magnitude:

$$d\epsilon^p = d\lambda \frac{\delta g}{\delta \sigma} \tag{C-4}$$

where λ is a non-negative scalar constant. The function g is called the flow rule. Flow rules are called "associated" if $f = g$ and "non-associated" otherwise.

C.3 Implementation Procedure in FLAC3D

FLAC3D uses the incremental theory of plasticity to arrive at an explicit solution. Constitutive models in FLAC3D return the stress state at time $t + \Delta t$ given the stress state at t and the strain increment incurred during Δt. To accomplish this, the incremental stress state is first assumed to be purely elastic, as described in Eq. (C-5).

$$\begin{aligned}\Delta\sigma_1 &= \alpha_1\Delta\epsilon_1^e + \alpha_2\left(\Delta\epsilon_2^e + \Delta\epsilon_3^e\right)\\ \Delta\sigma_2 &= \alpha_1\Delta\epsilon_2^e + \alpha_2\left(\Delta\epsilon_1^e + \Delta\epsilon_3^e\right)\\ \Delta\sigma_3 &= \alpha_1\Delta\epsilon_3^e + \alpha_2\left(\Delta\epsilon_1^e + \Delta\epsilon_2^e\right)\end{aligned} \tag{C-5}$$

where:

$$\begin{aligned}\alpha_1 &= K + \frac{4}{3}G\\ \alpha_2 &= K - \frac{2}{3}G\end{aligned} \tag{C-6}$$

and:

$$\begin{aligned}K &= \frac{E}{3\left(1-2\nu\right)}\\ G &= \frac{E}{2\left(1+\nu\right)}\end{aligned} \tag{C-7}$$

Eq. (C-5) is an incremental representation of Hooke's Law. The elastic stress increments incurred during Δt as determined by Eq. (C-5) are added to the total stress state present at time t, to determine what is called the "elastic guess."

The elastic guess is then compared to the yield surface and the state of the zone with respect to yielding is determined by Eq. (C-3). If the zone has not yielded, i.e. $f > 0$, then the elastic guess is the correct state of stress at time $t + \Delta t$. If the zone has yielded, i.e. $f \leq 0$, then a plastic correction must be applied. Since only the elastic portion of the total strain increment can contribute to a stress change, a correction for the plastic portion must be made according to the flow rule (Eq. (C-4)). The FLAC3D manual represents this correction with the symbol λ as:

$$\sigma^N = \sigma^I - \lambda S\left(\frac{\delta g}{\delta\sigma}\right) \tag{C-8}$$

where σ^N is the new stress state at time $t + \Delta t$, σ^I is the elastic guess, and $S\left(\frac{\delta g}{\delta\sigma}\right)$ is an expression for the incremental form of Hooke's Law, shown in Eq. (C-5), with the partial derivatives of the flow rule substituted for the incremental strain terms. This correction factor, λ, which is used to bring the elastic guess back to the flow rule if the yield criterion is violated, takes the form:

$$\lambda = \frac{f\left(\sigma^I\right)}{\delta f^{\star}[(S\left(\frac{\delta g}{\delta \sigma}\right)])} \tag{C-9}$$

where $f^{\star}$ is the failure surface function without its constant term.

The implementation of these equations for the Tresca constitutive model will be illustrated in the following section.

C.4 Incremental Tresca Constitutive Model in FLAC3D

The Tresca constitutive model assumes yielding will occur when the shear stress reaches a critical value, k, as shown:

$$\max[\tau_1, \tau_2, \tau_3] = k \tag{C-10}$$

or in terms of the normal principal stresses:

$$\max\left[\frac{|\sigma_1 - \sigma_2|}{2}, \frac{|\sigma_2 - \sigma_3|}{2}, \frac{|\sigma_3 - \sigma_1|}{2}\right] = k \tag{C-11}$$

The Tresca constitutive model considers only shear stress and assumes no increase in shear strength with an increase in confinement–as, for instance, the Mohr-Coulomb criterion does (in fact, the Mohr-Coulomb can be considered a generalization of the Tresca criterion. i.e. The Mohr-Coulomb criterion reduces to the Tresca criterion when the angle of internal friction is assumed to be zero.). In the principal stress space of σ_1 - σ_2 - σ_3, the Tresca failure surface plots as a regular hexagonal prism parallel to and centered around the hydrostatic stress axis where $\sigma_1 = \sigma_2 = \sigma_3$, as depicted in Figure C.1. Any state of stress which plots inside of this regular hexagonal prism is expected to be in the elastic state. States of stress plotted on the prism represent yielding, and states of stress outside of the prism cannot exist according to the Tresca criterion.

Since the Tresca yield surface is parallel to and prismatic around the hydrostatic axis, it is hydrostatic-stress independent. It is, therefore, only necessary to consider the projection of a stress state onto the deviatoric plane. The normal of the deviatoric plane is the hydrostatic stress axis. The Tresca criterion is plotted on a deviatoric plane in Figure C.2.

By assigning $\sigma_1 \leq \sigma_2 \leq \sigma_3$, Eq. (C-11) can be simplified to:

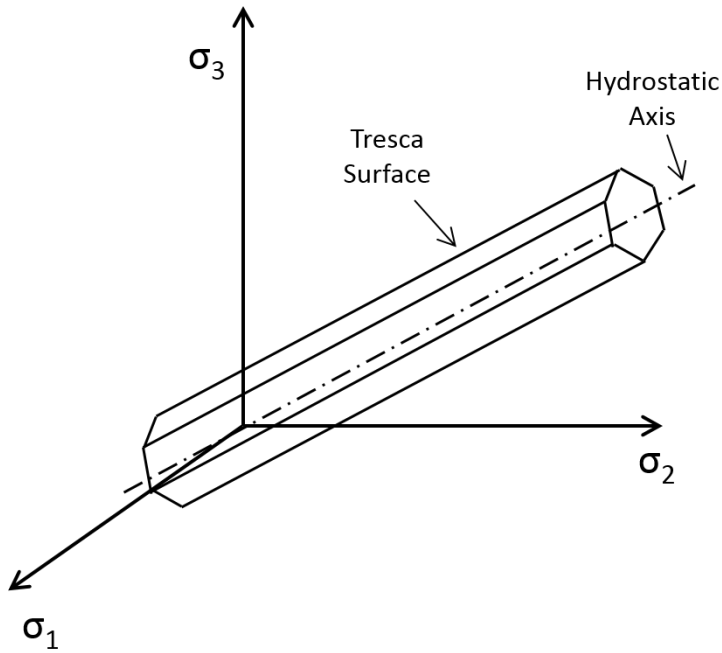

Figure C.1: Tresca failure surface plotted in the principal stress space with the hydrostatic stress axis labeled.

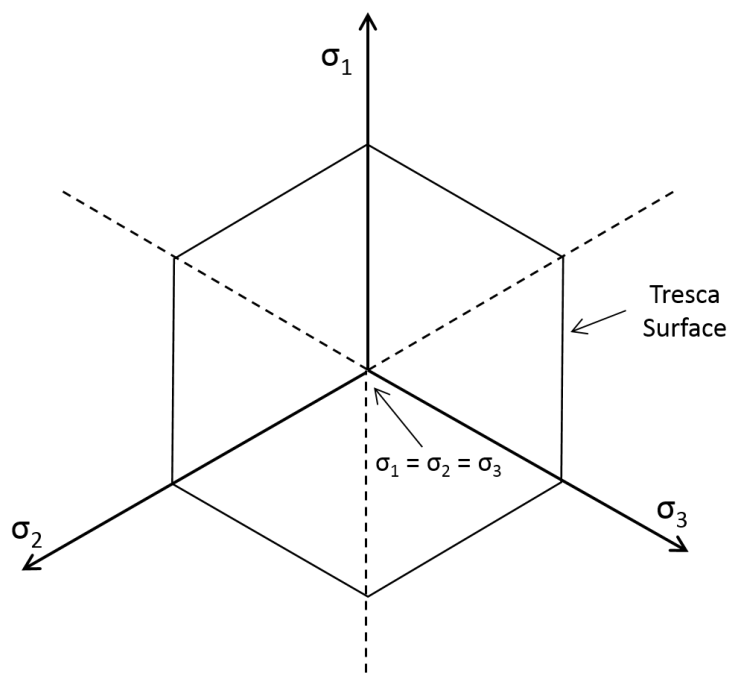

Figure C.2: Projection of the Tresca yield surface onto the deviatoric plane.

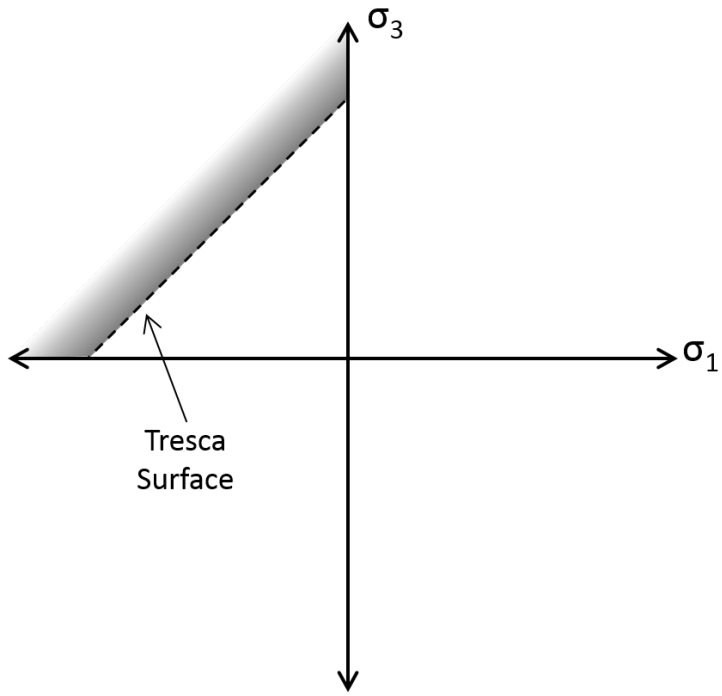

Figure C.3: Tresca yield surface plotted on the σ_1–σ_3 plane.

$$\frac{|\sigma_1 - \sigma_3|}{2} = k \tag{C-12}$$

or as a yield surface which follows the conditions of Eq. (C-3) and which follows the compressive stress-negative convention of FLAC3D:

$$f(\sigma_1, \sigma_2, \sigma_3) = \sigma_1 - \sigma_3 + 2k = 0 \tag{C-13}$$

The Tresca failure surface implemented in FLAC3D is plotted in Figure C.3. Two-dimensional cross-sections of the Tresca criterion along principal axis planes are well known to be hexagonal. The condition restricting $\sigma_1 \leq \sigma_2 \leq \sigma_3$ eliminates all sides of the hexagon save the one shown.

Assuming associated flow, the plastic flow rule takes the form:

$$g(\sigma_1, \sigma_2, \sigma_3) = \sigma_1 - \sigma_3 \tag{C-14}$$

Elastic guesses are evaluated according to Eqs. C-13 and C-3. Guesses violating the yield criterion, which would plot in the shaded region of Figure C.3, are placed back on the yield surface where $f(\sigma_1, \sigma_2, \sigma_3) = 0$ by using the associated flow rule shown in Eq. (C-14).

The procedure used for implementing these plastic corrections to the elastic guesses is shown in the following section.

C.4.1 Plastic Corrections

Partial differentiation of Eq. (C-14), the flow rule, yields:

$$\begin{aligned} \frac{\delta g}{\delta \sigma_1} &= 1 \\ \frac{\delta g}{\delta \sigma_2} &= 0 \\ \frac{\delta g}{\delta \sigma_3} &= -1 \end{aligned} \tag{C-15}$$

Substitution of the partial derivatives shown in Eq. (C-15) into the incremental Hooke's Law shown in Eq. (C-5) for $\Delta\epsilon_1^e$, $\Delta\epsilon_2^e$, and $\Delta\epsilon_3^e$ gives:

$$\begin{aligned} S_1\left(\frac{\delta g}{\delta \sigma_1}, \frac{\delta g}{\delta \sigma_2}, \frac{\delta g}{\delta \sigma_3}\right) &= \alpha_1 - \alpha_2 \\ S_2\left(\frac{\delta g}{\delta \sigma_1}, \frac{\delta g}{\delta \sigma_2}, \frac{\delta g}{\delta \sigma_3}\right) &= \alpha_2 - \alpha_1 \\ S_3\left(\frac{\delta g}{\delta \sigma_1}, \frac{\delta g}{\delta \sigma_2}, \frac{\delta g}{\delta \sigma_3}\right) &= \alpha_2 - \alpha_1 \end{aligned} \tag{C-16}$$

It follows that the new stress state, including plastic adjustments made to the elastic guesses, as shown in Eq. (C-8), takes the form:

$$\begin{aligned} \sigma_1^N &= \sigma_1^I - \lambda(\alpha_1 - \alpha_2) \\ \sigma_2^N &= \sigma_2^I - \lambda(\alpha_2 - \alpha_1) \\ \sigma_3^N &= \sigma_3^I - \lambda(\alpha_2 - \alpha_1) \end{aligned} \tag{C-17}$$

where:

$$\lambda = \frac{f\left(\sigma_1^I, \sigma_2^I, \sigma_3^I\right)}{(\alpha_1 - \alpha_2) - (\alpha_2 - \alpha_1)} \tag{C-18}$$

The procedure outlined above was implemented in FLAC3D as mentioned in Chapters 3 and 4. The actual implementation was somewhat simpler than that outlined above because the material was assumed to be loaded uniaxially and it was also assumed that no horizontal stresses developed due to this loading. These assumptions led to a failure point at $f = \sigma_1 + 2k = 0$ rather than a failure surface. Accordingly, there are simplifications to the associative plastic flow rule and the procedure for making plastic corrections to the elastic guesses.

References

[1] Wai-Fah Chen and Atef F Saleeb. *Constitutive equations for engineering materials: Elasticity and modeling*, volume 37a. Elsevier, 1994.

[2] Wai-Fah Chen. *Constitutive equations for engineering materials: Plasticity and modeling*, volume 37b. Elsevier, 1994.

[3] Itasca Consulting Group, Inc., Minnesota. *Fast Lagrangian Analysis of Continua in 3-Dimensions, version 5.0, manual*, 2013.

Appendix D

Parametric Analysis of Coal Material

D.1 Coal Pillars with Width:Height = 6

Table D.1: Numerical modeling input parameters for the coal pillar which resulted in the stress-strain curve shown in Figure D.1.

Parameter	Value
Young's Modulus	1.5 GPa
Intact Compressive Strength	10 MPa

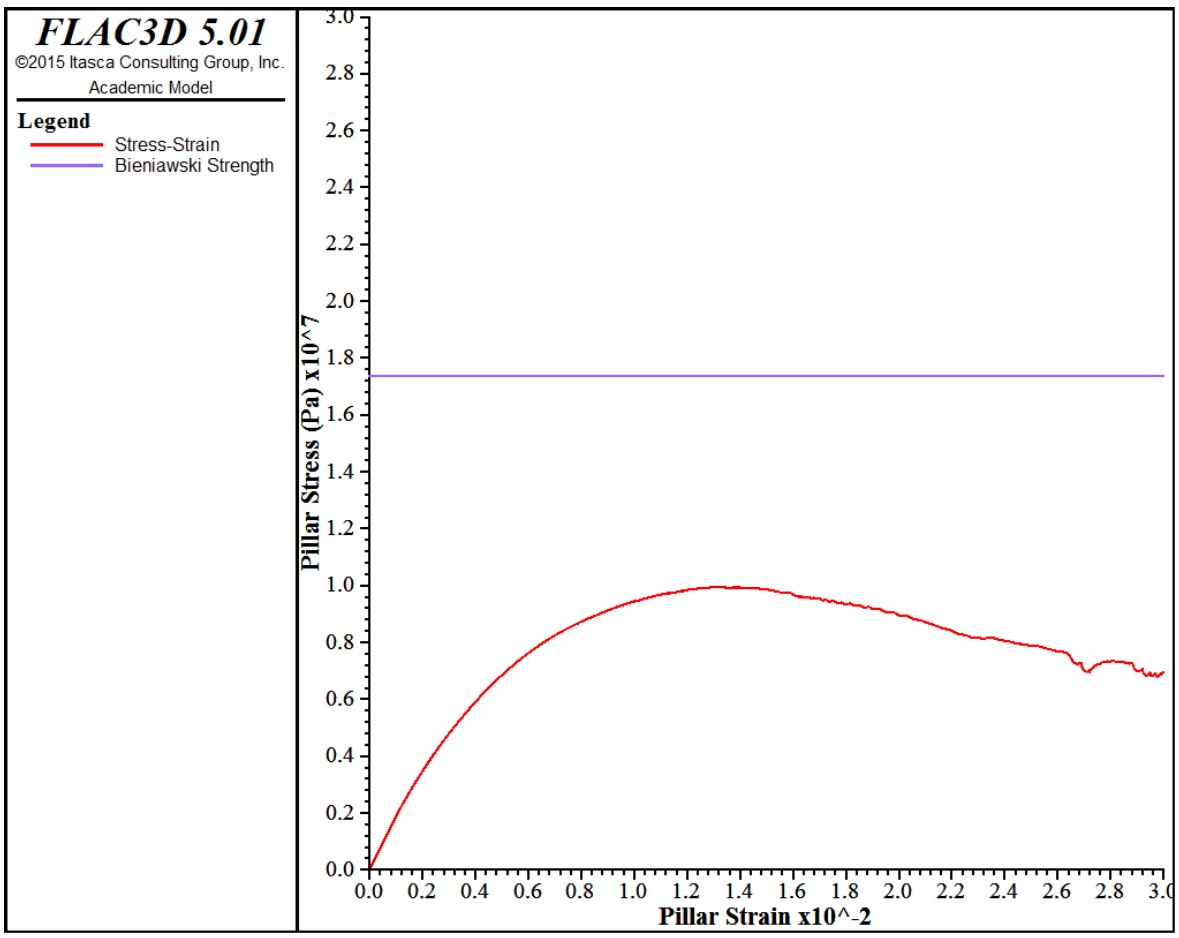

Figure D.1: Pillar stress-strain curve obtained in FLAC3D with the model inputs listed in Table D.1. The pillar strength empirically predicted by the Bieniawski equation is also plotted.

Table D.2: Numerical modeling input parameters for the coal pillar which resulted in the stress-strain curve shown in Figure D.2.

Parameter	Value
Young's Modulus	3.0 GPa
Intact Compressive Strength	10 MPa

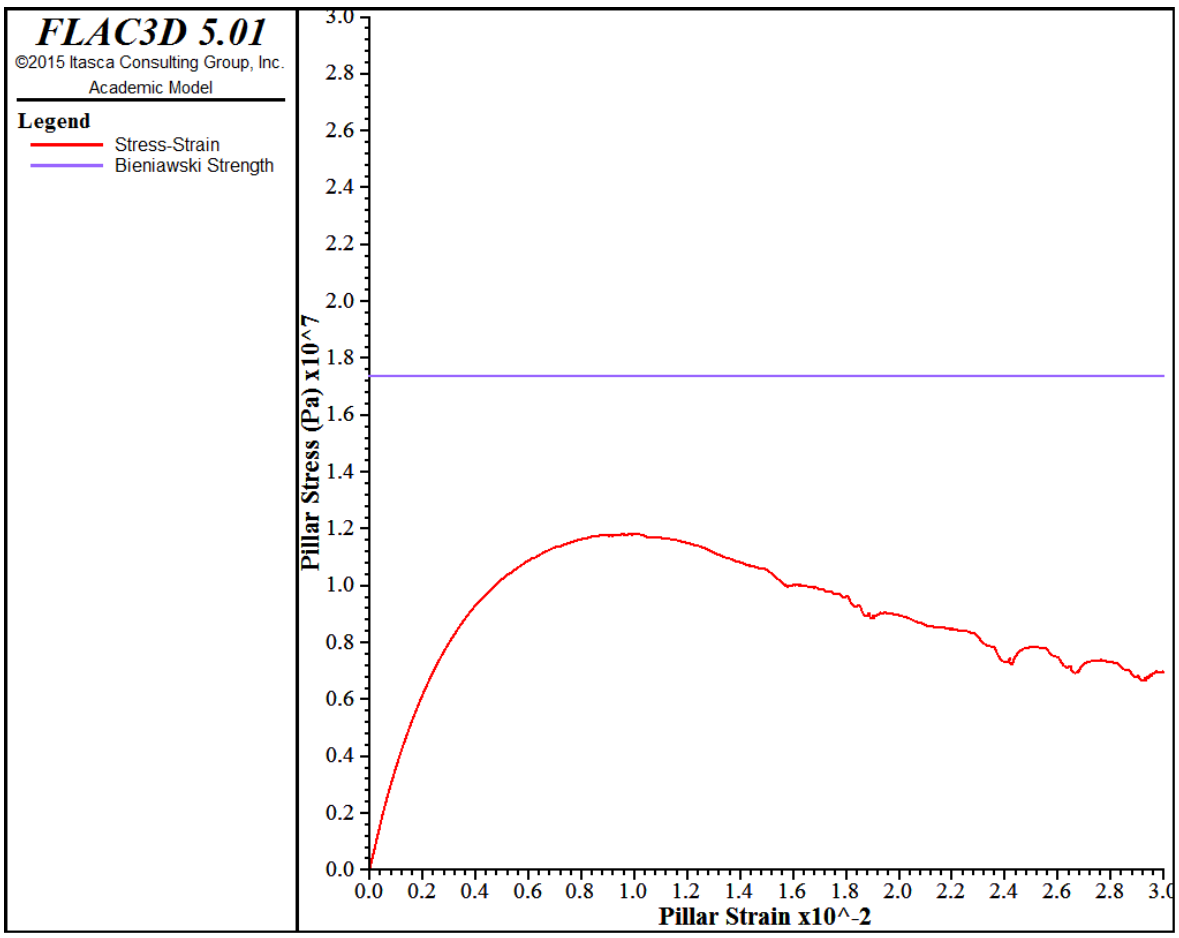

Figure D.2: Pillar stress-strain curve obtained in FLAC3D with the model inputs listed in Table D.2. The pillar strength empirically predicted by the Bieniawski equation is also plotted.

Table D.3: Numerical modeling input parameters for the coal pillar which resulted in the stress-strain curve shown in Figure D.3.

Parameter	Value
Young's Modulus	4.5 GPa
Intact Compressive Strength	10 MPa

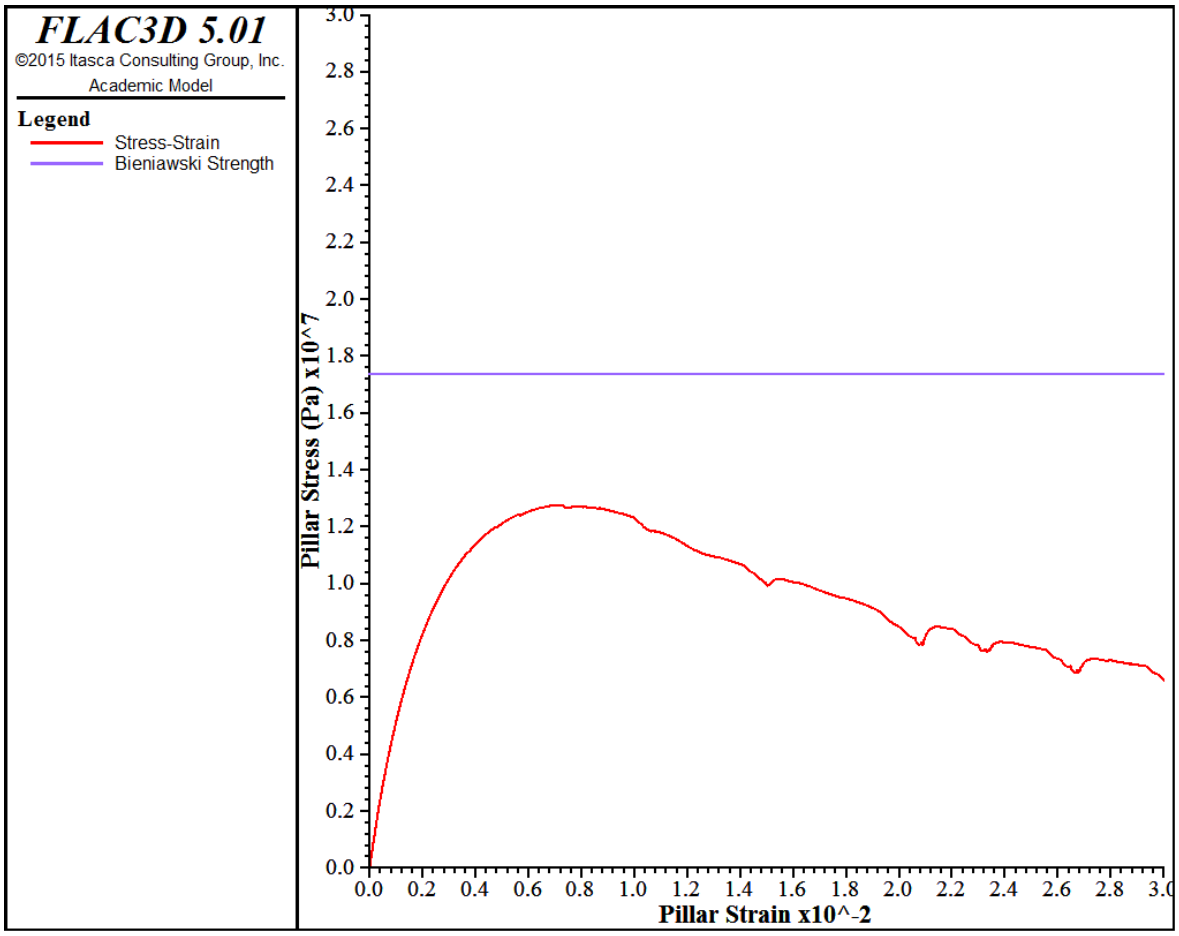

Figure D.3: Pillar stress-strain curve obtained in FLAC3D with the model inputs listed in Table D.3. The pillar strength empirically predicted by the Bieniawski equation is also plotted.

Table D.4: Numerical modeling input parameters for the coal pillar which resulted in the stress-strain curve shown in Figure D.4.

Parameter	Value
Young's Modulus	1.5 GPa
Intact Compressive Strength	20 MPa

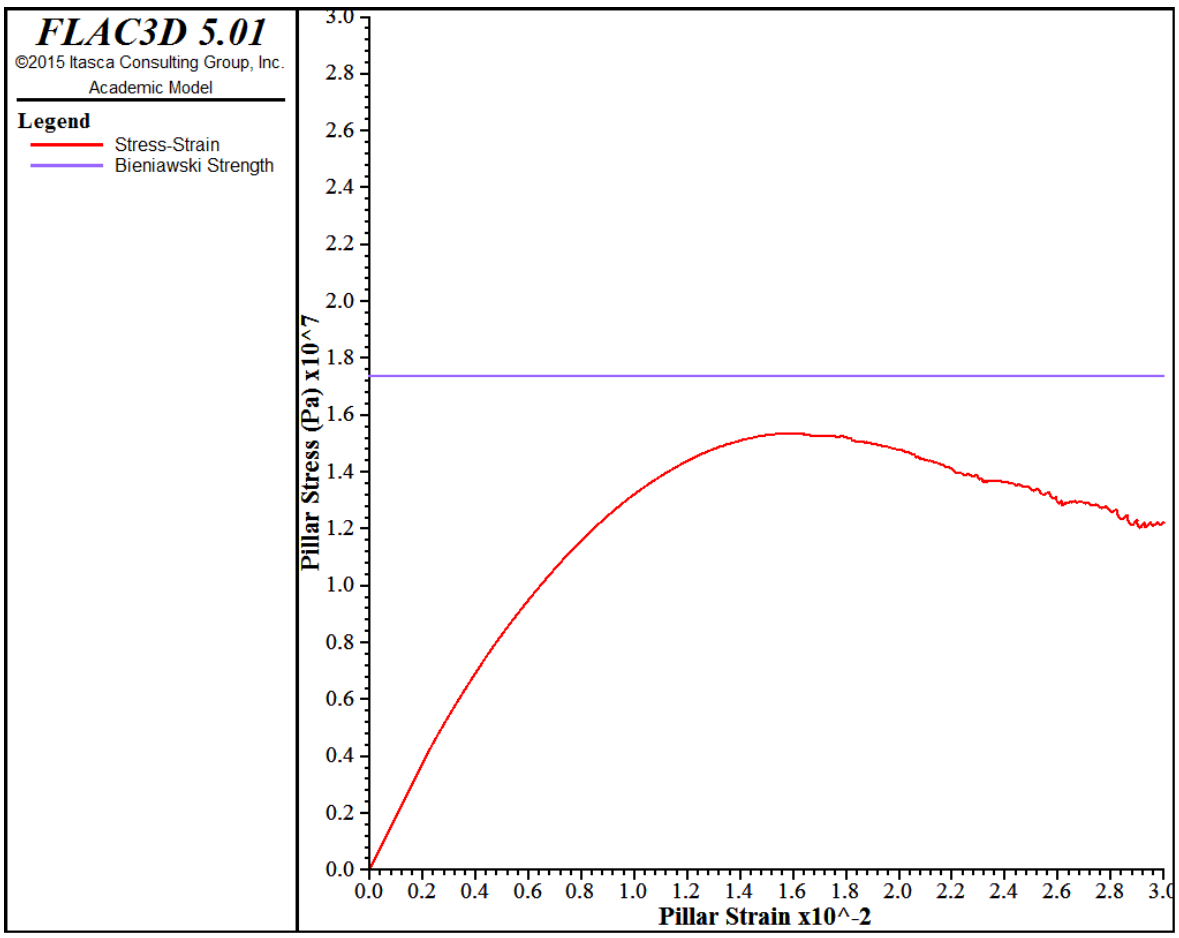

Figure D.4: Pillar stress-strain curve obtained in FLAC3D with the model inputs listed in Table D.4. The pillar strength empirically predicted by the Bieniawski equation is also plotted.

Table D.5: Numerical modeling input parameters for the coal pillar which resulted in the stress-strain curve shown in Figure D.5.

Parameter	Value
Young's Modulus	3.0 GPa
Intact Compressive Strength	20 MPa

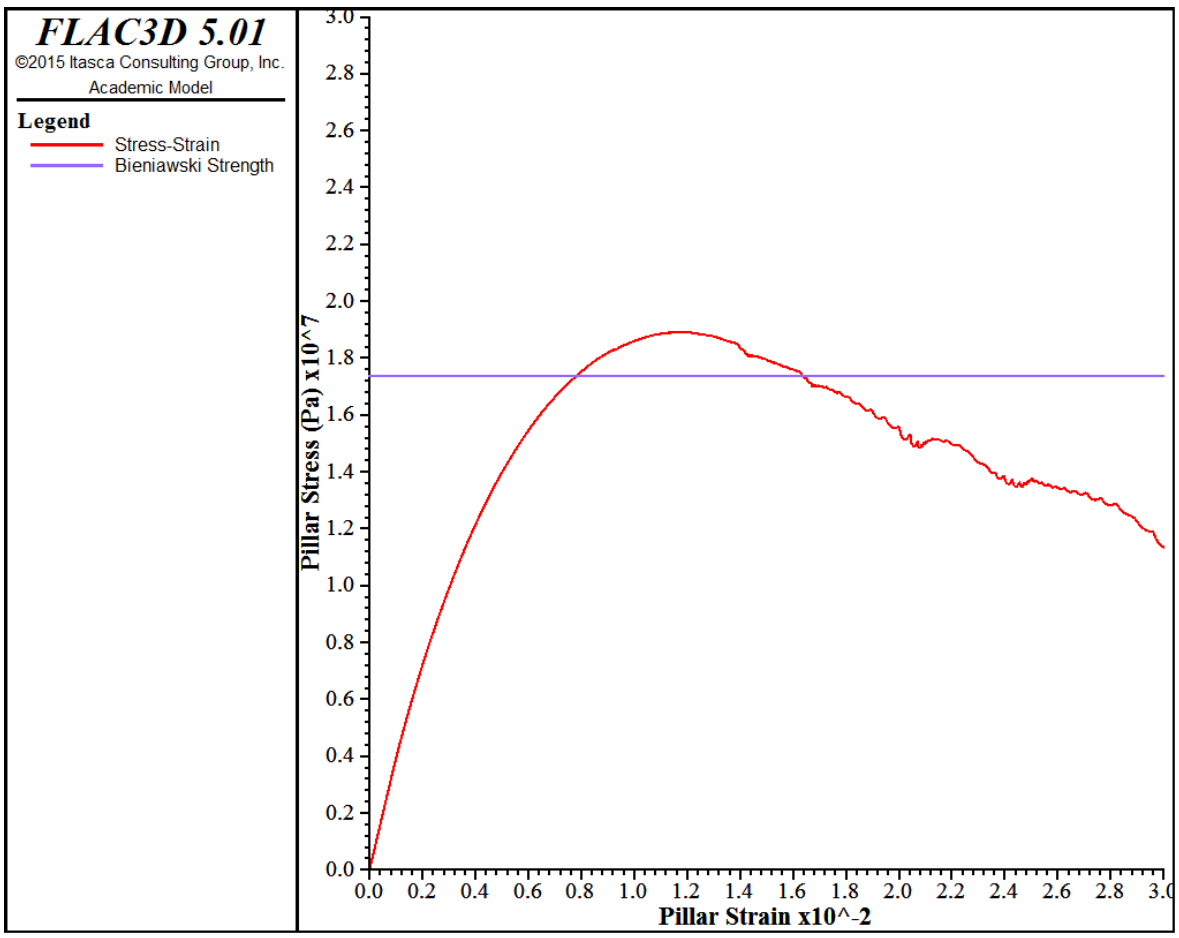

Figure D.5: Pillar stress-strain curve obtained in FLAC3D with the model inputs listed in Table D.5. The pillar strength empirically predicted by the Bieniawski equation is also plotted.

Table D.6: Numerical modeling input parameters for the coal pillar which resulted in the stress-strain curve shown in Figure D.6.

Parameter	Value
Young's Modulus	4.5 GPa
Intact Compressive Strength	20 MPa

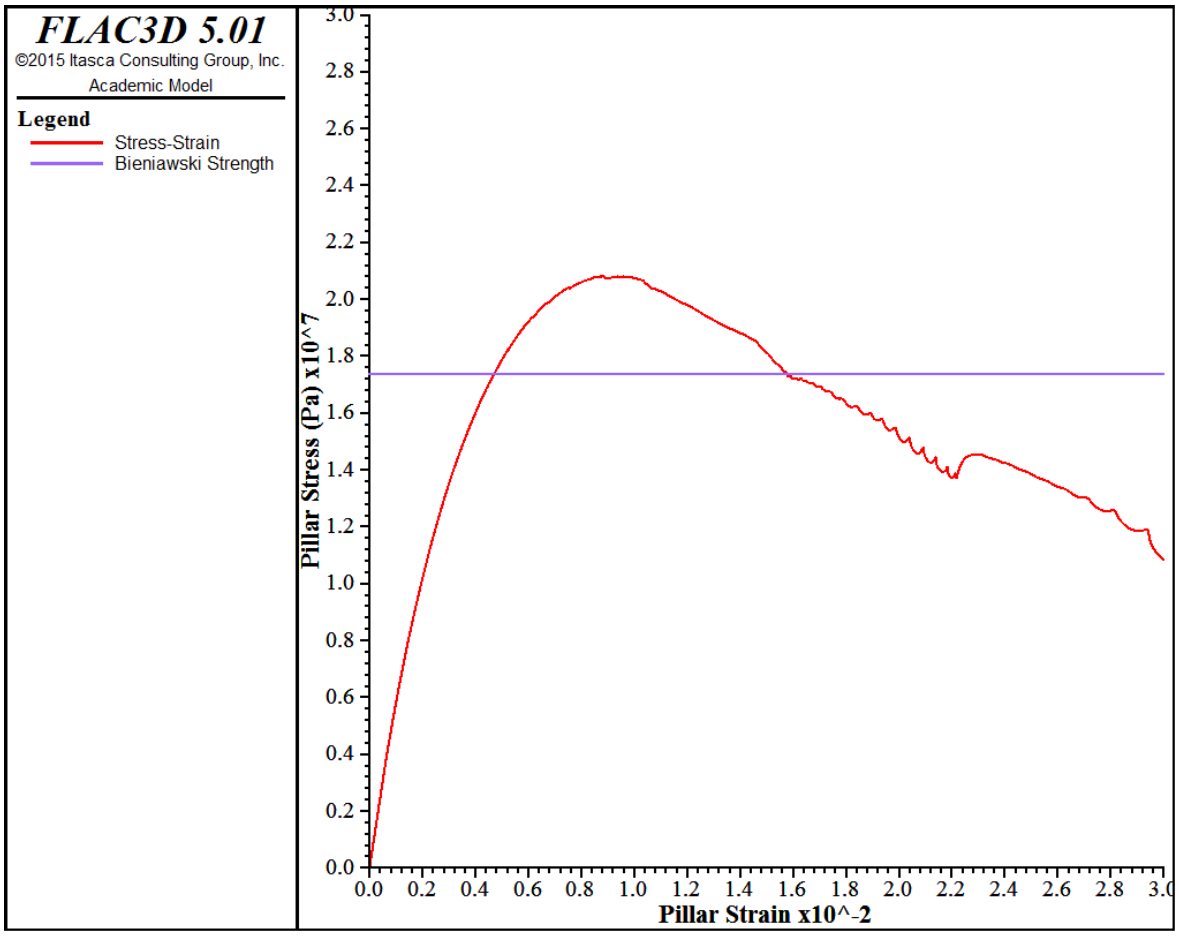

Figure D.6: Pillar stress-strain curve obtained in FLAC3D with the model inputs listed in Table D.6. The pillar strength empirically predicted by the Bieniawski equation is also plotted.

Table D.7: Numerical modeling input parameters for the coal pillar which resulted in the stress-strain curve shown in Figure D.7.

Parameter	Value
Young's Modulus	1.5 GPa
Intact Compressive Strength	30 MPa

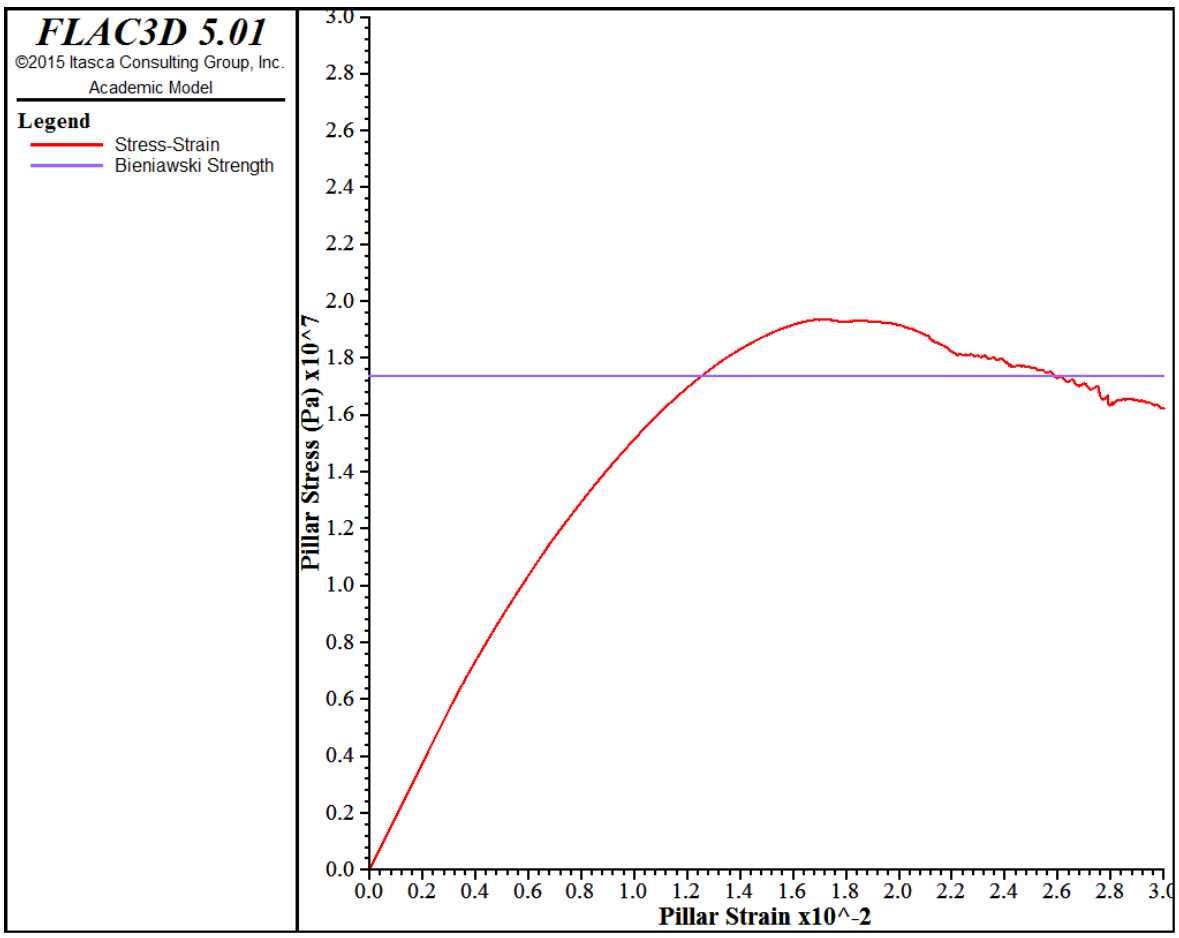

Figure D.7: Pillar stress-strain curve obtained in FLAC3D with the model inputs listed in Table D.7. The pillar strength empirically predicted by the Bieniawski equation is also plotted.

Table D.8: Numerical modeling input parameters for the coal pillar which resulted in the stress-strain curve shown in Figure D.8.

Parameter	Value
Young's Modulus	3.0 GPa
Intact Compressive Strength	30 MPa

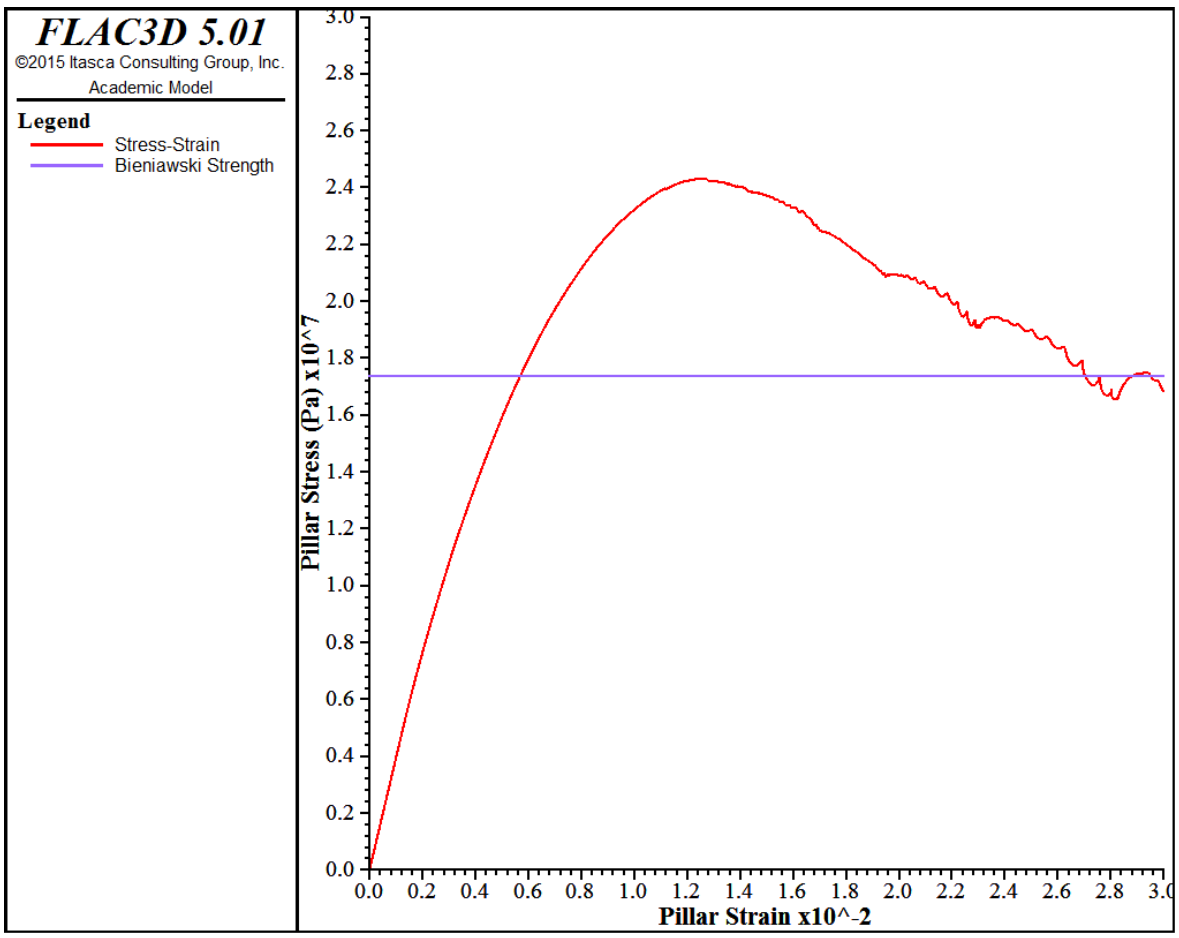

Figure D.8: Pillar stress-strain curve obtained in FLAC3D with the model inputs listed in Table D.8. The pillar strength empirically predicted by the Bieniawski equation is also plotted.

Table D.9: Numerical modeling input parameters for the coal pillar which resulted in the stress-strain curve shown in Figure D.9.

Parameter	Value
Young's Modulus	4.5 GPa
Intact Compressive Strength	30 MPa

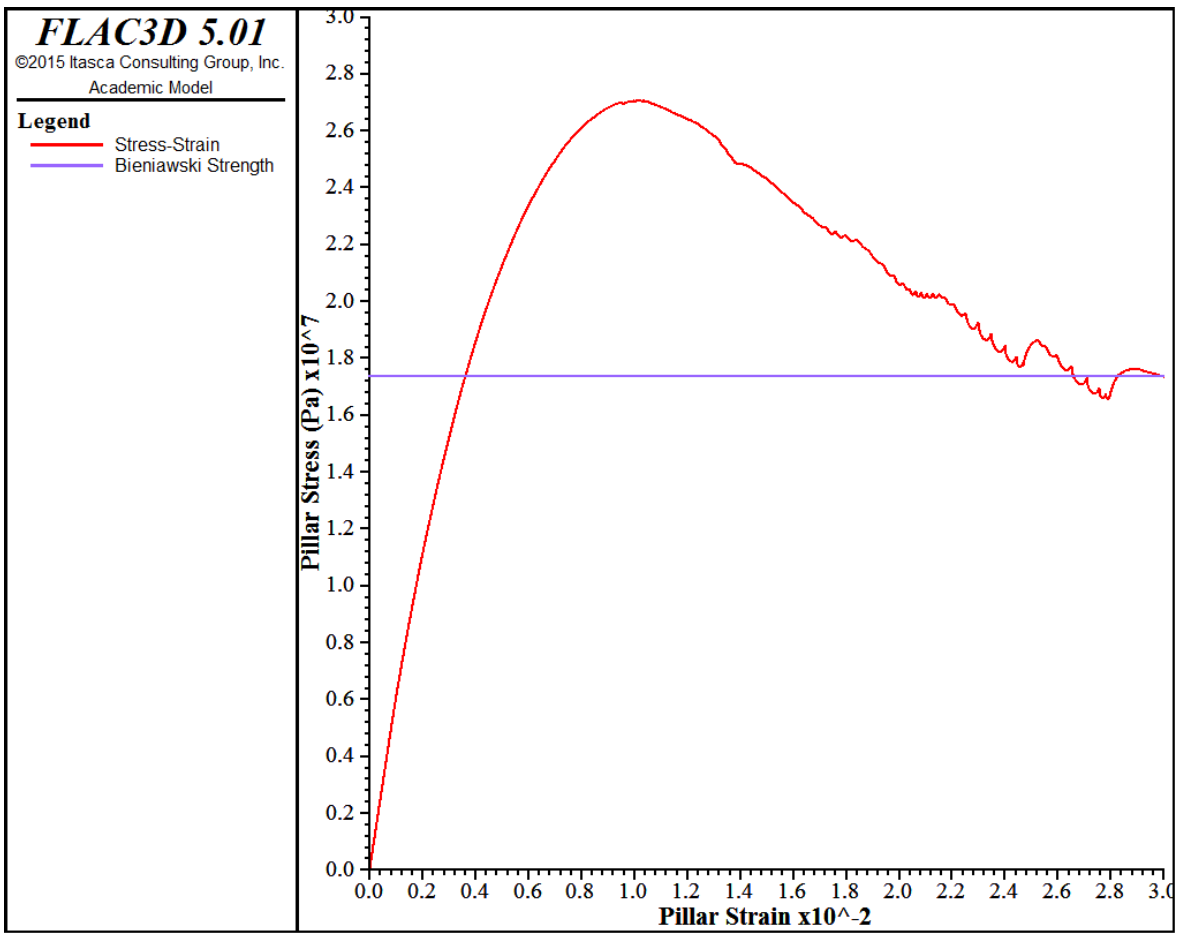

Figure D.9: Pillar stress-strain curve obtained in FLAC3D with the model inputs listed in Table D.9. The pillar strength empirically predicted by the Bieniawski equation is also plotted.

D.2 Coal Pillars with Width:Height = 8

Table D.10: Numerical modeling input parameters for the coal pillar which resulted in the stress-strain curve shown in Figure D.10.

Parameter	Value
Young's Modulus	1.5 GPa
Intact Compressive Strength	10 MPa

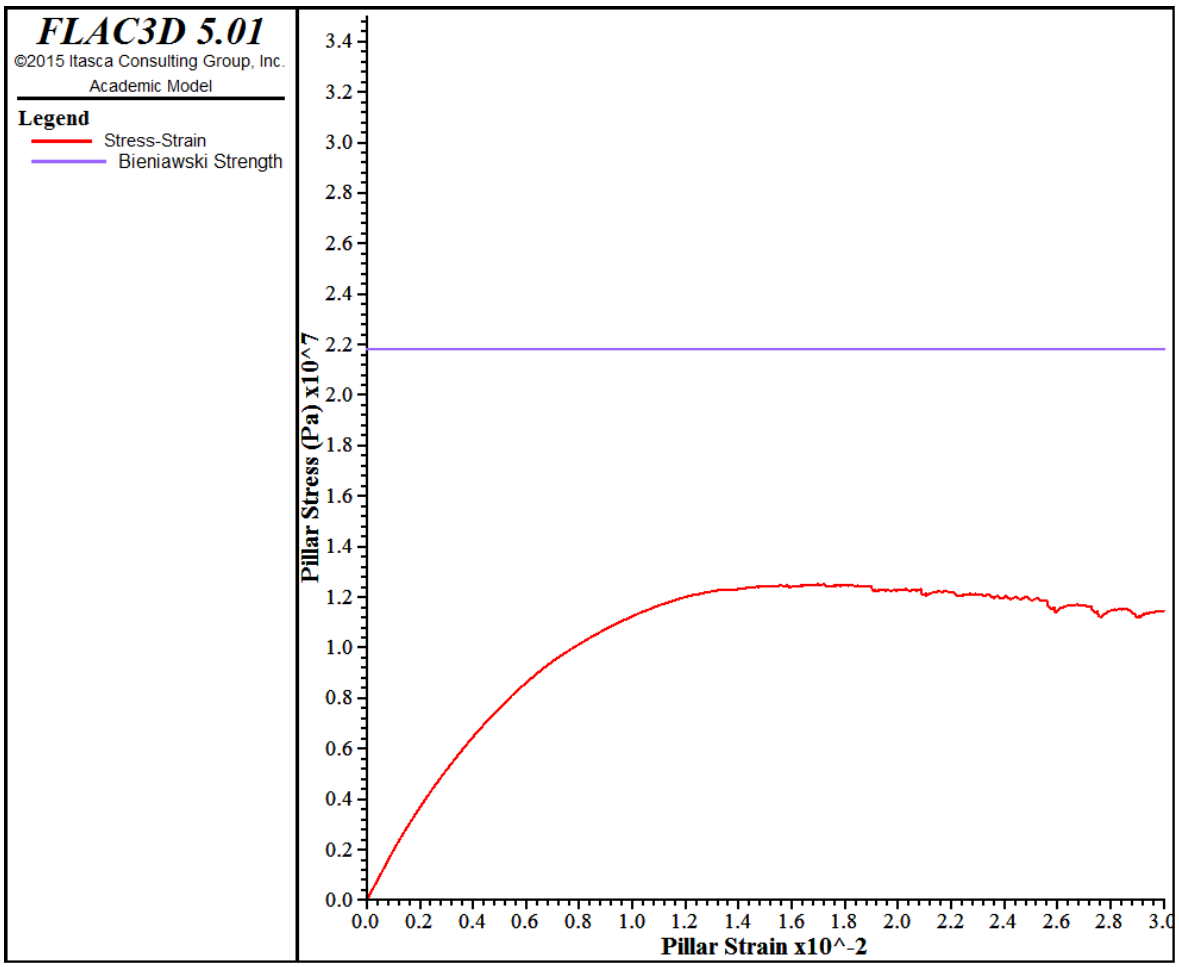

Figure D.10: Pillar stress-strain curve obtained in FLAC3D with the model inputs listed in Table D.10. The pillar strength empirically predicted by the Bieniawski equation is also plotted.

Table D.11: Numerical modeling input parameters for the coal pillar which resulted in the stress-strain curve shown in Figure D.11.

Parameter	Value
Young's Modulus	3.0 GPa
Intact Compressive Strength	10 MPa

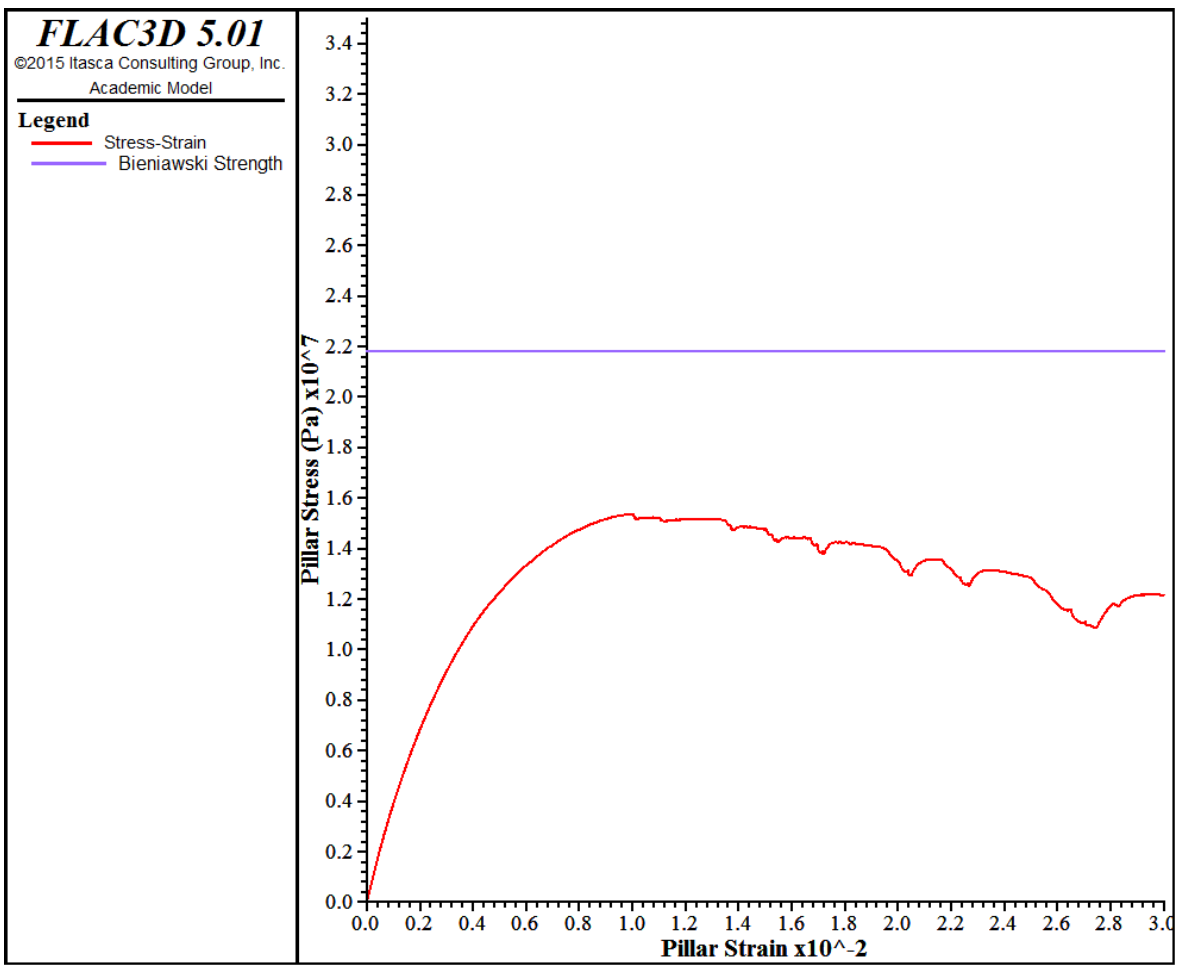

Figure D.11: Pillar stress-strain curve obtained in FLAC3D with the model inputs listed in Table D.11. The pillar strength empirically predicted by the Bieniawski equation is also plotted.

Table D.12: Numerical modeling input parameters for the coal pillar which resulted in the stress-strain curve shown in Figure D.12.

Parameter	Value
Young's Modulus	4.5 GPa
Intact Compressive Strength	10 MPa

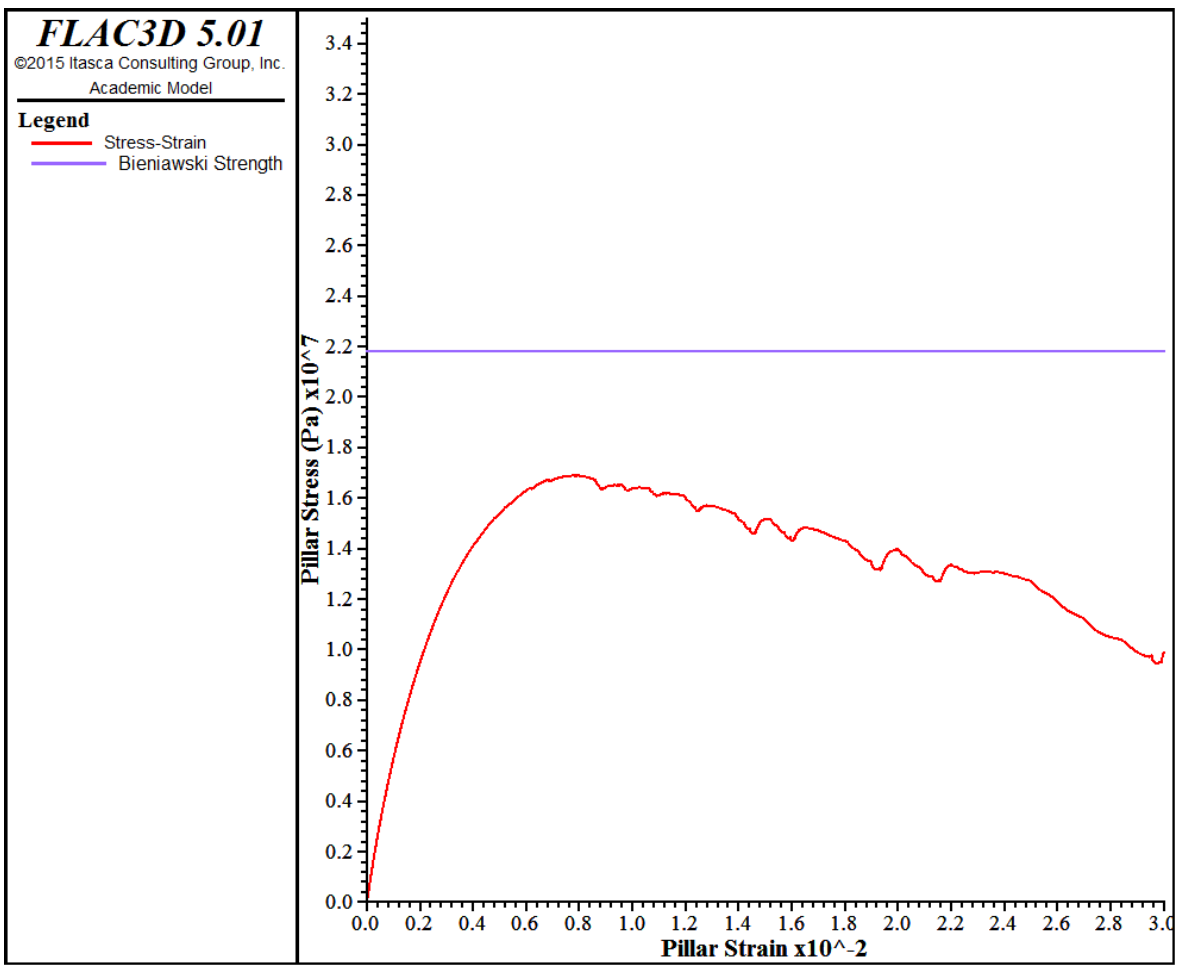

Figure D.12: Pillar stress-strain curve obtained in FLAC3D with the model inputs listed in Table D.12. The pillar strength empirically predicted by the Bieniawski equation is also plotted.

Table D.13: Numerical modeling input parameters for the coal pillar which resulted in the stress-strain curve shown in Figure D.13.

Parameter	Value
Young's Modulus	1.5 GPa
Intact Compressive Strength	20 MPa

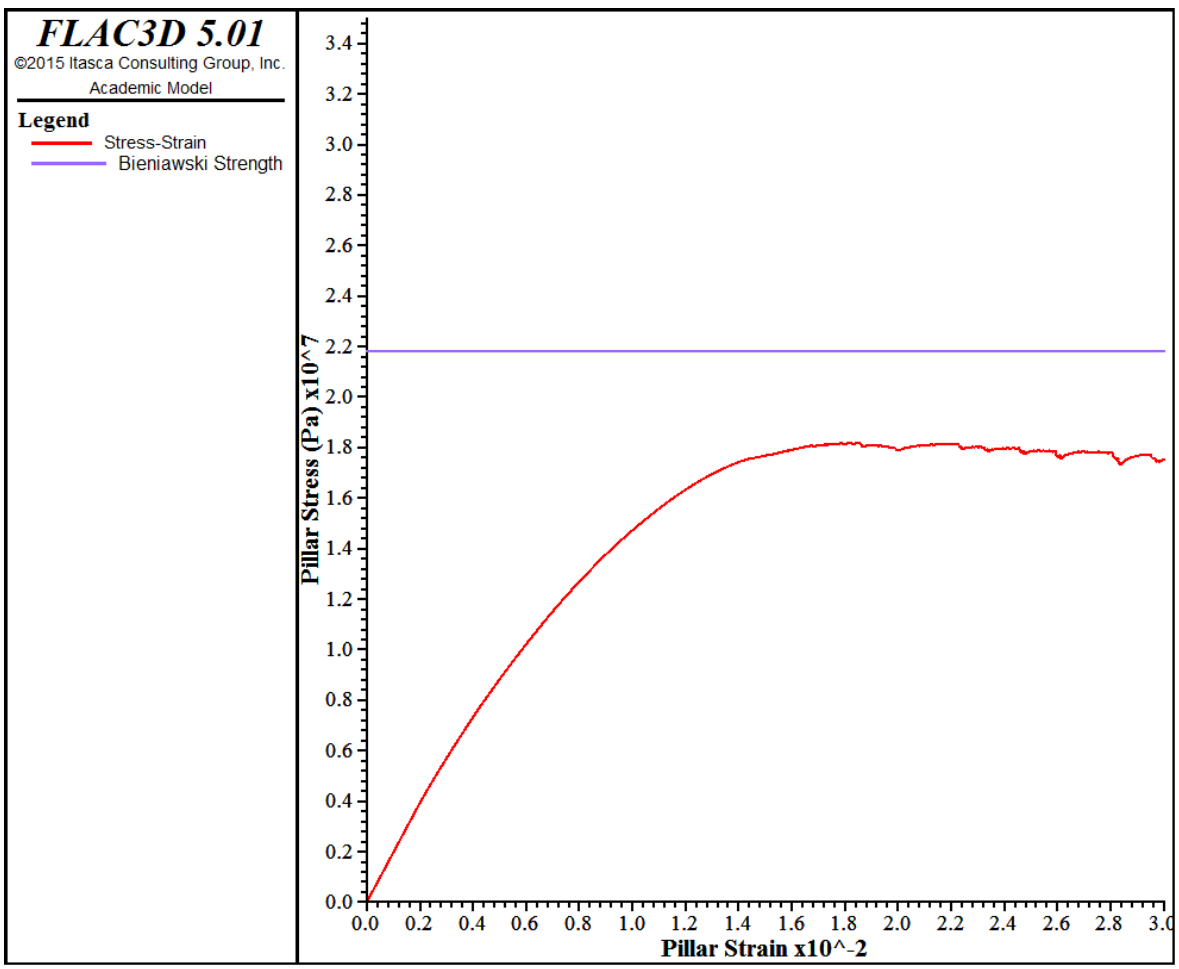

Figure D.13: Pillar stress-strain curve obtained in FLAC3D with the model inputs listed in Table D.13. The pillar strength empirically predicted by the Bieniawski equation is also plotted.

Table D.14: Numerical modeling input parameters for the coal pillar which resulted in the stress-strain curve shown in Figure D.14.

Parameter	Value
Young's Modulus	3.0 GPa
Intact Compressive Strength	20 MPa

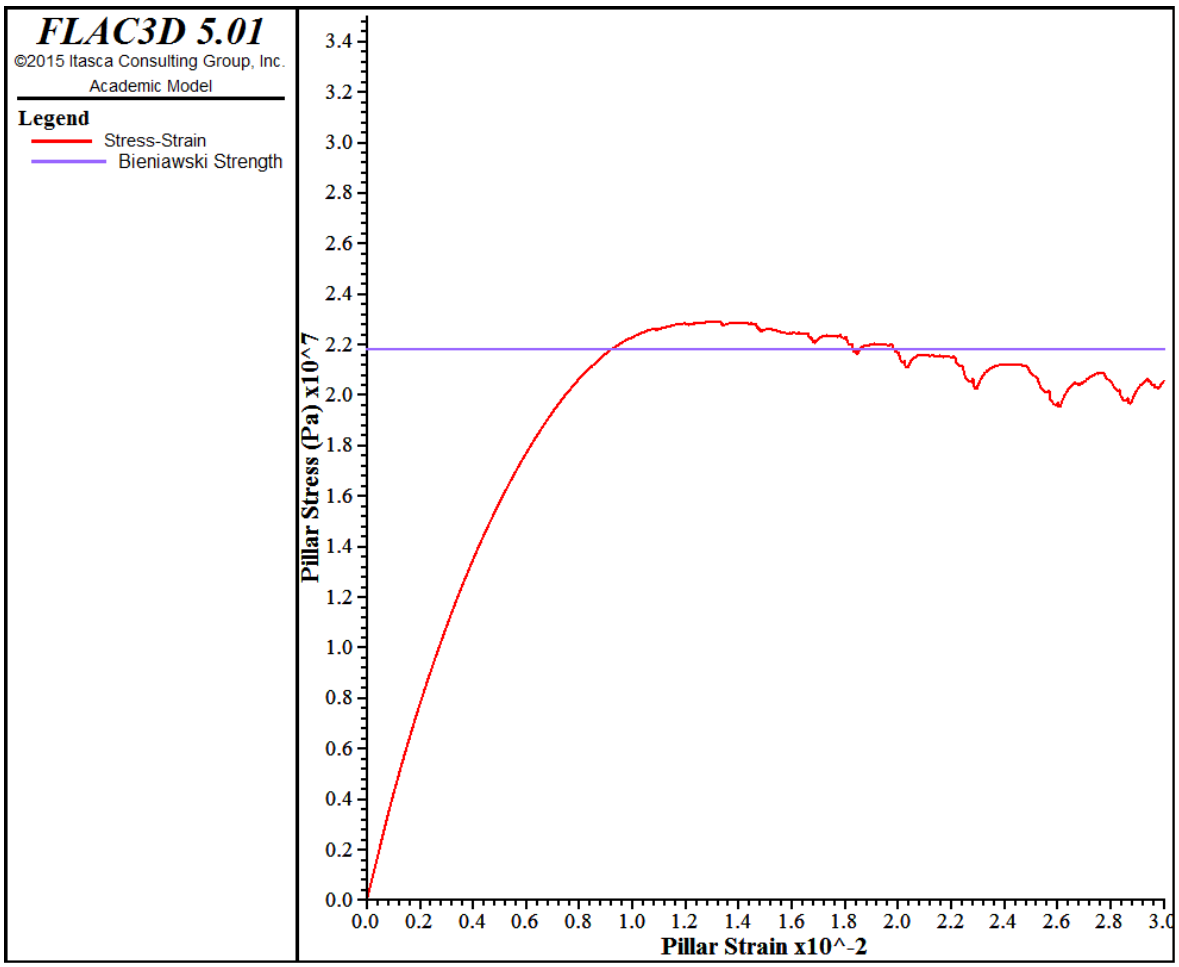

Figure D.14: Pillar stress-strain curve obtained in FLAC3D with the model inputs listed in Table D.14. The pillar strength empirically predicted by the Bieniawski equation is also plotted.

Table D.15: Numerical modeling input parameters for the coal pillar which resulted in the stress-strain curve shown in Figure D.15.

Parameter	Value
Young's Modulus	4.5 GPa
Intact Compressive Strength	20 MPa

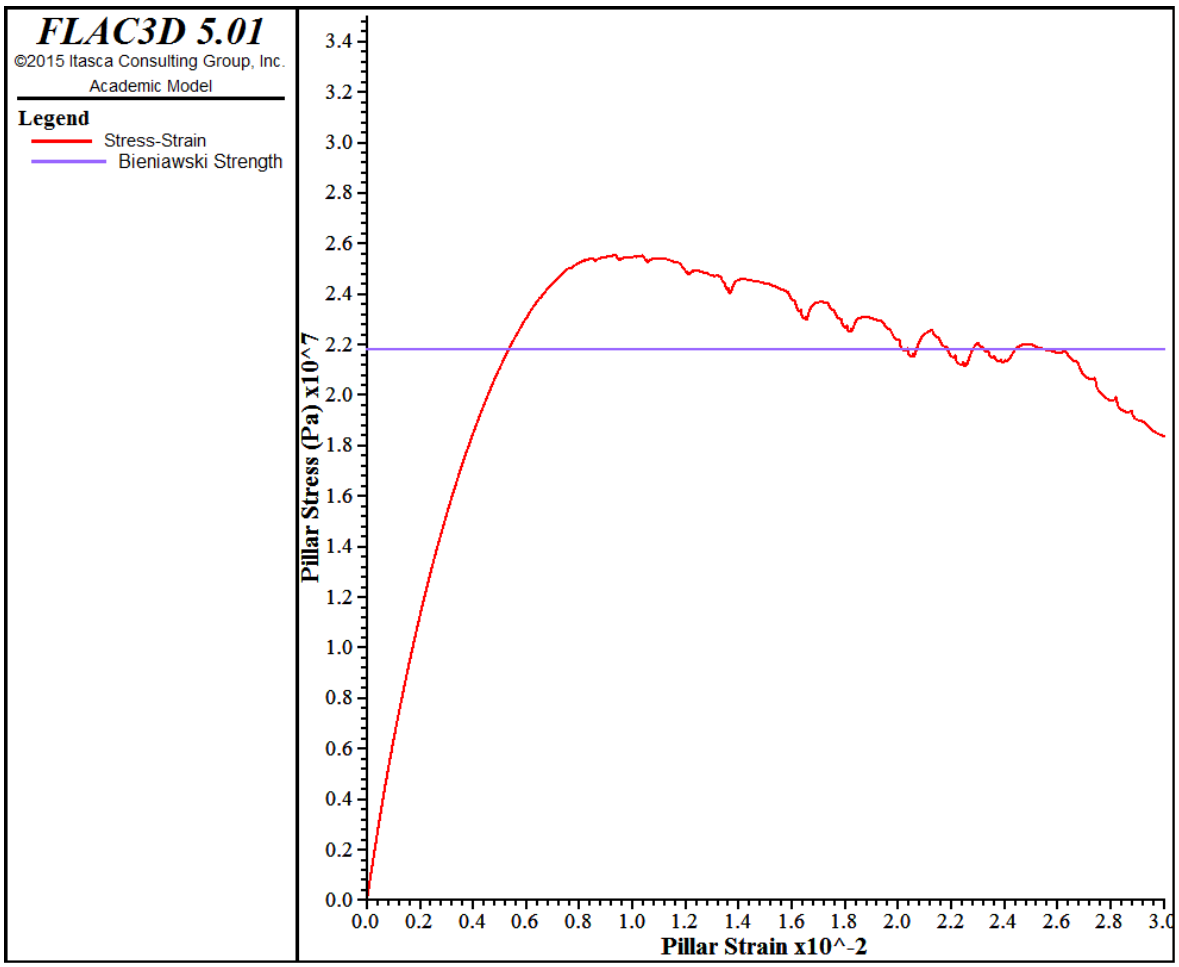

Figure D.15: Pillar stress-strain curve obtained in FLAC3D with the model inputs listed in Table D.15. The pillar strength empirically predicted by the Bieniawski equation is also plotted.

Table D.16: Numerical modeling input parameters for the coal pillar which resulted in the stress-strain curve shown in Figure D.16.

Parameter	Value
Young's Modulus	1.5 GPa
Intact Compressive Strength	30 MPa

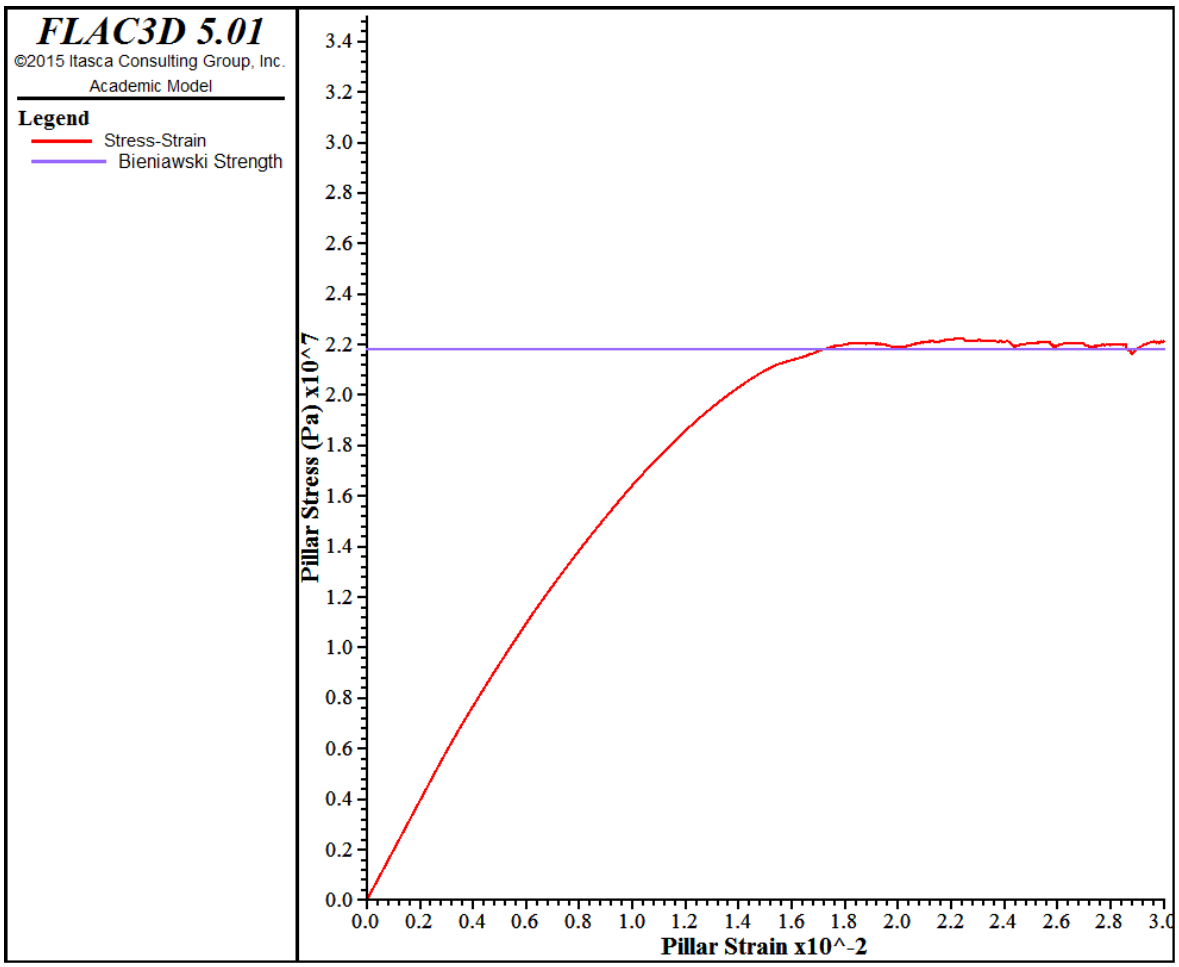

Figure D.16: Pillar stress-strain curve obtained in FLAC3D with the model inputs listed in Table D.16. The pillar strength empirically predicted by the Bieniawski equation is also plotted.

Table D.17: Numerical modeling input parameters for the coal pillar which resulted in the stress-strain curve shown in Figure D.17.

Parameter	Value
Young's Modulus	3.0 GPa
Intact Compressive Strength	30 MPa

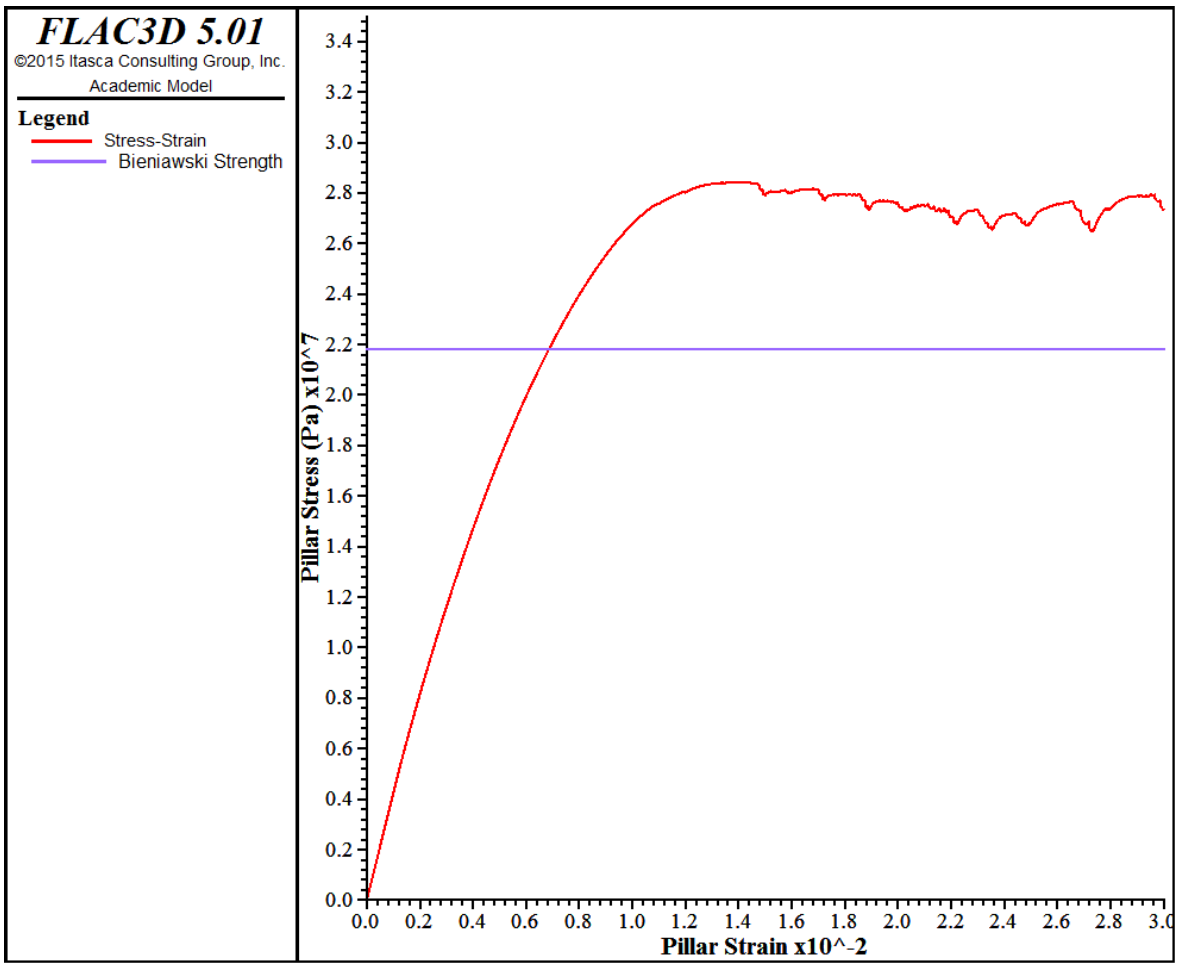

Figure D.17: Pillar stress-strain curve obtained in FLAC3D with the model inputs listed in Table D.17. The pillar strength empirically predicted by the Bieniawski equation is also plotted.

Table D.18: Numerical modeling input parameters for the coal pillar which resulted in the stress-strain curve shown in Figure D.18.

Parameter	Value
Young's Modulus	4.5 GPa
Intact Compressive Strength	30 MPa

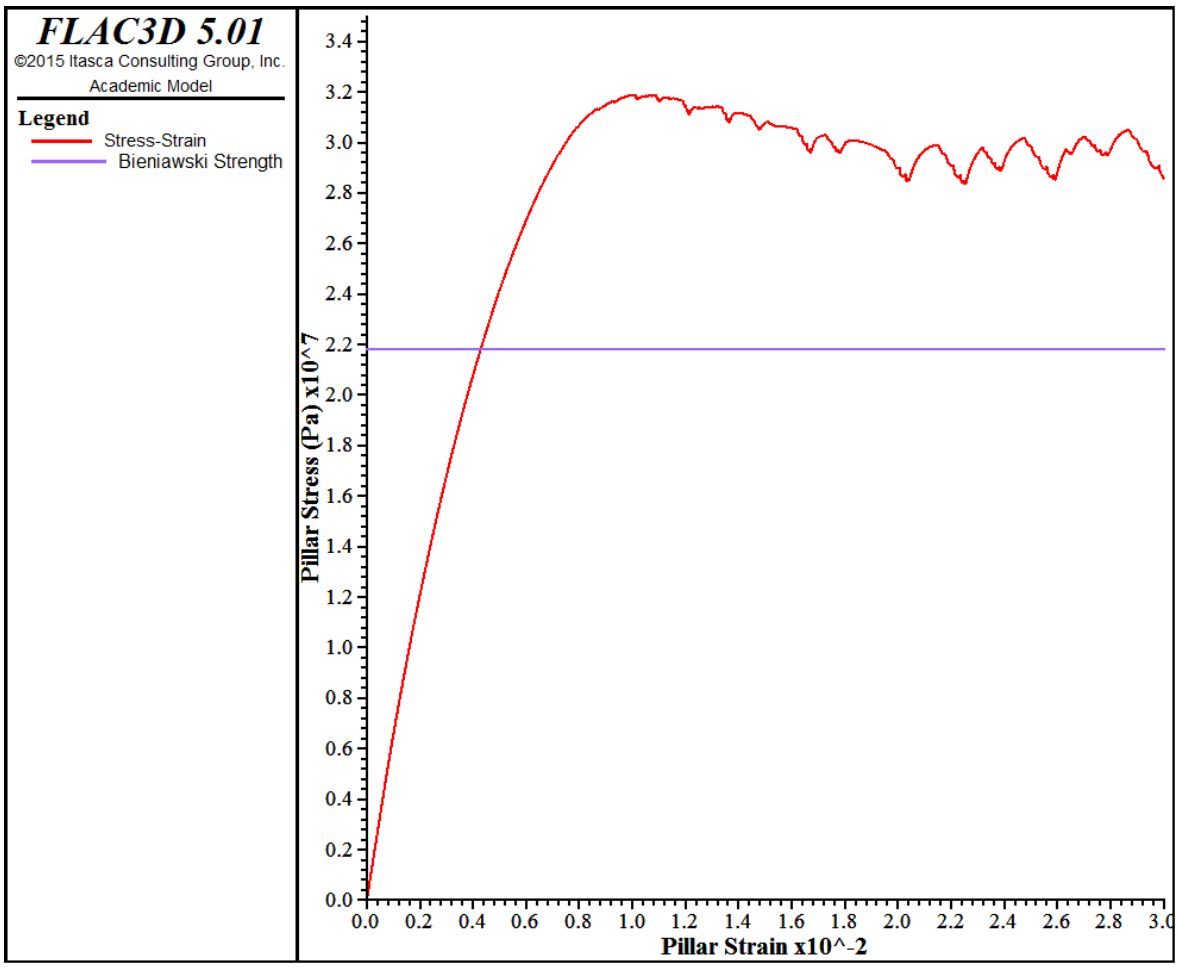

Figure D.18: Pillar stress-strain curve obtained in FLAC3D with the model inputs listed in Table D.18. The pillar strength empirically predicted by the Bieniawski equation is also plotted.

Works Cited

[1] US EIA. Annual coal report 2013. *US Energy Information Administration, Washington, DC*, 2013.

[2] US EIA. Short term energy outlook. *Energy Information Administration, Department of Energy*, 2016.

[3] Christopher Mark and Thomas M Barczak. Fundamentals of coal mine roof support. *New Technology for Coal Mine Roof Support, Proceedings of the NIOSH Open Industry Briefing, NIOSH IC*, 9453:23–42, 2000.

[4] Mine safety and health administration.

[5] Edwin T Brown, John W Bray, Branko Ladanyi, and Evert Hoek. Ground response curves for rock tunnels. *Journal of Geotechnical Engineering*, 1983.

[6] Pierpaolo Oreste. The convergence-confinement method: roles and limits in modern geomechanical tunnel design. *American Journal of Applied Sciences*, 6(4):757, 2009.

[7] B Damjanac, M Pierce, and M Board. Methodology for stability analysis of large room-and-pillar panels. In *48th US Rock Mechanics/Geomechanics Symposium*. American Rock Mechanics Association, 2014.

[8] Itasca Consulting Group, Inc., Minnesota. *Fast Lagrangian Analysis of Continua in 3-Dimensions, version 5.0, manual*, 2013.

[9] Essie Esterhuizen, Chris Mark, and Michael Murphy. The ground response curve, pillar loading and pillar failure in coal mines. In *29th International Conference on Ground Control in Mining*, 2010.

[10] Inc. Itasca Consulting Group. Flac3d training course - basic concepts and recommended procedures, 2015.

[11] Norman E Dowling. *Mechanical behavior of materials: engineering methods for deformation, fracture, and fatigue*. Prentice hall, 1993.

[12] DU Deere, AJ Hendron, FD Patton, and EJ Cording. Design of surface and near-surface construction in rock. In *The 8th US Symposium on Rock Mechanics (USRMS)*. American Rock Mechanics Association, 1966.

[13] DU Deere. Geological considerations. *Rock mechanics in engineering practice*, pages 1–20, 1968.

[14] DU Deere and DW Deere. The rock quality designation (RQD) index in practice. In *Symposium on Rock Classification Systems for Engineering Purposes, 1987, Cincinnati, Ohio, USA*, 1988.

[15] ZT Bieniawski. Engineering classification of jointed rock masses. *Civil Engineer in South Africa*, 15(12), 1973.

[16] ZT Bieniawski. The geomechanics classification in rock engineering applications. In *4th ISRM Congress*. International Society for Rock Mechanics, 1979.

[17] ZT Bieniawski. *Engineering rock mass classifications: a complete manual for engineers and geologists in mining, civil, and petroleum engineering*. John Wiley & Sons, 1989.

[18] N. Barton, R. Lien, and J. Lunde. Engineering classification of rock masses for the design of tunnel support. *Rock mechanics*, 6(4):189–236, 1974.

[19] NGI. Using the Q-system: rock mass classification and support design. Norwegian Geotechnical Institute, Oslo, April 2013.

[20] V Marinos, P Marinos, and Evert Hoek. The geological strength index: applications and limitations. *Bulletin of Engineering Geology and the Environment*, 64(1):55–65, 2005.

[21] E Hoek, PK Kaiser, and WF Bawden. *Support of underground excavations in hard rock*. AA Balkema, Rotterdam, 1995.

[22] AJ Hendron. Mechanical properties of rock. *Rock Mechanics in Engineering Practice*, pages 21–53, 1968.

[23] Nick Barton. Shear strength criteria for rock, rock joints, rockfill and rock masses: Problems and some solutions. *Journal of Rock Mechanics and Geotechnical Engineering*, 5(4):249 – 261, 2013.

[24] Nick Barton and Stavros Bandis. Effects of block size on the shear behavior of jointed rock. In *The 23rd US Symposium on Rock Mechanics (USRMS)*. American Rock Mechanics Association, 1982.

[25] Seong-Tae Yi, Min-Su Kim, Jin-Keun Kim, and Jang-Ho Jay Kim. Effect of specimen size on flexural compressive strength of reinforced concrete members. *Cement and Concrete Composites*, 29(3):230–240, 2007.

[26] JN van der Merwe. A laboratory investigation into the effect of specimen size on the strength of coal samples from different areas. *Journal of the South African Institute of Mining and Metallurgy*, 103(5):273–279, 2003.

[27] Z.T. Bieniawski. The effect of specimen size on compressive strength of coal. *International Journal of Rock Mechanics and Mining Sciences & Geomechanics Abstracts*, 5 (4):325 – 335, 1968.

[28] Evert Hoek. Strength of jointed rock masses. *Geotechnique*, 33(3):187–223, 1983.

[29] Evert Hoek and Paul Marinos. A brief history of the development of the Hoek-Brown failure criterion. *Soils and rocks*, 2:1–8, 2007.

[30] GA Wiebols and NGW Cook. An energy criterion for the strength of rock in polyaxial compression. In *International Journal of Rock Mechanics and Mining Sciences & Geomechanics Abstracts*, volume 5 (6), pages 529–549. Elsevier, 1968.

[31] R Ulusay. *The ISRM Suggested Methods for Rock Characterization, Testing and Monitoring: 2007-2014*. Springer, 2015.

[32] Q Xu, J Chen, J Li, C Zhao, and C Yuan. Study on the constitutive model for jointed rock mass. *PloS one*, 10(4), 2015.

[33] ZF Zhang and J Eckert. Unified tensile fracture criterion. *Physical review letters*, 94(9):094301, 2005.

[34] John Conrad Jaeger and Neville GW Cook. *Fundamentals of rock mechanics*. Chapman & Hall, London, 3rd edition, 1979.

[35] Evert Hoek and Edwin T Brown. *Underground excavations in rock*. Institution of Mining and Metallurgy, 1980.

[36] Evert Hoek and Edwin T Brown. The Hoek-Brown failure criterion-a 1988 update. In *Proc. 15th Canadian Rock Mech. Symp*, pages 31–38. Toronto, Dept. Civil Engineering, University of Toronto, 1988.

[37] E Hoek, D Wood, and S Shah. A modified Hoek-Brown failure criterion for jointed rock masses. In *Eurock*, volume 92, pages 209–13, 1992.

[38] Sandip Shah. *A study of the behaviour of jointed rock masses*. PhD thesis, University of Toronto, 1992.

[39] C. Mark and F.E. Chase. Analysis of retreat mining pillar stability (armps). In *Proceedings-New Technology for Ground Control in Retreat Mining. Pittsburgh, PA: US Department of Health and Human Services, Public Health Service, Centers for Disease Control and Prevention, National Institute for Occupational Safety and Health, DHHS (NIOSH) Publication*, pages 17–34, 1997.

[40] BN Whittaker, T Unlu, DJ Reddish, and Smith SF. Pillar design aspects for stability in deep coal mines. *Assessment and Prevention of Failure Phenomena in Rock Engineering*, 1993.

[41] C Mark. State-of-the-art in coal pillar design. *Transactions-Society for Mining Metallurgy and Exploration Incorporated*, 308:123–128, 2000.

[42] WA Hustrulid. A review of coal pillar strength formulas. *Rock Mechanics*, 8(2):115–145, 1976.

[43] Christopher Mark and Timothy M Barton. Pillar design and coal strength. In *Proceedings-New Technology for Ground Control in Retreat Mining. Pittsburgh, PA: US Department of Health and Human Services, Public Health Service, Centers for Disease Control and Prevention, National Institute for Occupational Safety and Health, DHHS (NIOSH) Publication*, pages 49–59, 1997.

[44] M Jawed, RK Sinha, and S Sengupta. Chronological development in coal pillar design for bord and pillar workings: A critical appraisal. *Journal of Geology and Mining Research*, 5(1):1–11, 2013.

[45] H Wagner. Pillar design in coal mines. *JS Afr Inst Min Metall*, 80:37–45, 1980.

[46] Diego Lope Álvarez. Limitations of the ground reaction curve concept for shallow tunnels under anisotropic in-situ stress conditions. Master's thesis, Universitat Politècnica de Catalunya, 2012.

[47] N Vlachopoulos and MS Diederichs. Improved longitudinal displacement profiles for convergence confinement analysis of deep tunnels. *Rock mechanics and rock engineering*, 42(2):131–146, 2009.

[48] Thomas M Barczak. Optimizing secondary roof support with the niosh support technology optimization program (stop). In *Proceedings of 19th International Conference on Ground Control in Mining, Morgantown, WV*, pages 74–84, 2000.

[49] Thomas M Barczak, Thomas P Mucho, and Dennis R Dolinar. Design methodology for standing secondary roof support systems. *Proceedings, New Technology for Coal Mine Roof Support*, pages 133–150, 2000.

[50] JJK Daemen and C Fairhurst. Influence of failed rock properties on tunnel stability. In *The 12th US Symposium on Rock Mechanics (USRMS)*. American Rock Mechanics Association, 1970.

[51] JW Bray. A study of jointed and fractured rock. part ii–theory of limiting equilibrium. *Rock mechanics and engineering geology*, 5(4):197–216, Dec 1964.

[52] C Carranza-Torres and C Fairhurst. Application of the convergence-confinement method of tunnel design to rock masses that satisfy the Hoek-Brown failure criterion. *Tunnelling and Underground Space Technology*, 15(2):187–213, 2000.

[53] C Carranza-Torres and Ch Fairhurst. The elasto-plastic response of underground excavations in rock masses that satisfy the Hoek-Brown failure criterion. *International Journal of Rock Mechanics and Mining Sciences*, 36(6):777–809, 1999.

[54] Kyung-Ho Park, Bituporn Tontavanich, and Joo-Gong Lee. A simple procedure for ground response curve of circular tunnel in elastic-strain softening rock masses. *Tunnelling and Underground Space Technology*, 23(2):151–159, 2008.

[55] H Yavuz. Support pressure estimation for circular and non-circular openings based on a parametric numerical modelling study. *Journal-South African Institute Mining and Metallurgy*, 106(2):129, 2006.

[56] Essie Esterhuizen and Tom Barczak. Development of ground response curves for longwall tailgate support design. In *Golden Rocks 2006, The 41st US Symposium on Rock Mechanics (USRMS)*. American Rock Mechanics Association, 2006.

[57] Thomas M Barczak. A retrospective assessment of longwall roof support with a focus on challenging accepted roof support concepts and design premises. In *Proceedings of the 25th international conference on ground control in mining, Morgantown, WV*, pages 232–243, 2006.

[58] Thomas M Barczak, GS Esterhuizen, John Ellenberger, and P Zhang. A first step in developing standing roof support design criteria based on ground reaction data for Pittsburgh seam longwall tailgate support. In *Proceedings of the 27th International Conference on Ground Control in Mining*, pages 349–359, 2008.

[59] M Board, B Damjanac, and M Pierce. Development of a methodology for analysis of instability in room and pillar mines. In *Deep Mine 07, Proceedings of the Fourth International Seminar on Deep and High Stress Mining*, pages 273–282. Perth, Australia, 2007.

[60] William J Conrad. Microseismic monitoring of a room and pillar retreat coal mine in southwest virginia. Master's thesis, Virginia Polytechnic Institute and State University (Virginia Tech), 2016.

[61] Essie Esterhuizen, Chris Mark, and Michael M Murphy. Numerical model calibration for simulating coal pillars, gob and overburden response. In *Proceeding of the 29th international conference on ground control in mining, Morgantown, WV*, pages 46–57, 2010.

[62] Jienan Pan, Zhaoping Meng, Quanlin Hou, Yiwen Ju, and Yunxing Cao. Coal strength and young's modulus related to coal rank, compressional velocity and maceral composition. *Journal of Structural Geology*, 54:129–135, 2013.

[63] C Mark, F Chase, and D Pappas. Reducing the risk of ground falls during pillar recovery. *Transactions-society for mining, metallurgy, and exploration incorporated*, 314:153–160, 2003.

[64] MN Das. Influence of width/height ratio on post-failure behaviour of coal. *International Journal of Mining and Geological Engineering*, 4(1):79–87, 1986.

[65] ZT Bieniawski. A method revisited: coal pillar strength formula based on field investigations. In *Proceedings of the Workshop on Coal Pillar Mechanics and Design. Pittsburgh, PA: US Department of the Interior, Bureau of Mines, IC*, volume 9315, pages 158–165, 1992.

[66] Christopher Mark and Murali Gadde. Global trends in coal mine horizontal stress measurements. In *10th Coal Operator's Conference COAL 2010)*, 2010.

[67] J Townsend, C Meyers, R Ortega, J Peck, M Reinfurth, and B Weinstock. *Review of the probabilistic failure analysis methodology and other probabilistic approaches for application in aerospace structural design*, volume 3434. National Aeronautics and Space

Administration, Office of Management, Scientific and Technical Information Program, 1993.

[68] H. Park and TR West. Development of a probabilistic approach for rock wedge failure. *Engineering Geology*, 59(3):233–251, 2001.

[69] G. Zhou, T. Esaki, Y. Mitani, M. Xie, and J. Mori. Spatial probabilistic modeling of slope failure using an integrated gis monte carlo simulation approach. *Engineering Geology*, 68(3):373–386, 2003.

[70] Enno Reinsalu. Stochastic approach to room-and-pillar failure in oil shale mining. In *Proceedings of the Estonian Academy of Sciences, Engineering*, volume 6, pages 207–216. Estonian Academy Publishers, 2000.

[71] MATLAB. *version 8.0.0.783 (R2012b)*. The MathWorks Inc., Natick, Massachusetts, 2012.

[72] ZT Bieniawski. Ground control. *SME Mining Engineering Handbook. Littleton, CO: Society for Mining, Metallurgy, and Exploration, Inc*, pages 897–937, 1992.

[73] E. Broch and J.A. Franklin. The point-load strength test. *International Journal of Rock Mechanics and Mining Sciences & Geomechanics Abstracts*, 9(6):669 – 676, 1972.

[74] ZT Bieniawski and I Hawkes. Suggested methods for determining tensile strength of rock materials. In *International Journal of Rock Mechanics and Mining Sciences & Geomechanics Abstracts*, volume 15, pages 99–103. Elsevier, 1978.

[75] ZT Bieniawski and MJ Bernede. Suggested methods for determining the uniaxial compressive strength and deformability of rock materials: Part 1. suggested method for determination of the uniaxial compressive strength of rock materials. In *International Journal of Rock Mechanics and Mining Sciences & Geomechanics Abstracts*, volume 16 (2), page 137. Elsevier, 1979.

[76] Paul M Santi, Jason E Holschen, and Richard W Stephenson. Improving elastic modulus measurements for rock based on geology. *Environmental & Engineering Geoscience*, 6(4):333–346, 2000.

[77] ZT Bieniawski and MJ Bernede. Suggested methods for determining the uniaxial compressive strength and deformability of rock materials: Part 2. suggested method for determining deformability of rock material in uniaxial compression. In *International Journal of Rock Mechanics and Mining Sciences & Geomechanics Abstracts*, volume 16 (2), pages 138–140. Elsevier, 1979.

[78] Malcolm Mellor and Ivor Hawkes. Measurement of tensile strength by diametral compression of discs and annuli. *Engineering Geology*, 5(3):173–225, 1971.

[79] JA Franklin. Suggested method for determining point load strength. In *International Journal of Rock Mechanics and Mining Sciences & Geomechanics Abstracts*, volume 22 (2), pages 51–60. Elsevier, 1985.

[80] Norman Brook. *Comprehensive rock engineering: principles, practice, & projects*, volume 3. Pergamon Press Ltd, 1993.

[81] Jeff S Cargill and A Shakoor. Evaluation of empirical methods for measuring the uniaxial compressive strength of rock. In *International Journal of Rock Mechanics and Mining Sciences & Geomechanics Abstracts*, volume 27 (6), pages 495–503. Elsevier, 1990.

[82] John Rusnak and Christopher Mark. Using the point load test to determine the uniaxial compressive strength of coal measure rock. In *Proceedings of the 19th International Conference on Ground Control in Mining. Morgantown, WV: West Virginia University*, pages 362–371, 2000.

[83] Wai-Fah Chen and Atef F Saleeb. *Constitutive equations for engineering materials: Elasticity and modeling*, volume 37a. Elsevier, 1994.

[84] Wai-Fah Chen. *Constitutive equations for engineering materials: Plasticity and modeling*, volume 37b. Elsevier, 1994.